

# Optical tweezers-based microrheological measurements using a high-speed camera

by

**Victoria Emma Loosemore**

B.Sc., Mount Allison University, 2014

Thesis Submitted in Partial Fulfillment of the  
Requirements for the Degree of  
Master of Science

in the  
Department of Physics  
Faculty of Science

© **Victoria Emma Loosemore 2017**  
**SIMON FRASER UNIVERSITY**  
Spring 2017

All rights reserved.

However, in accordance with the *Copyright Act of Canada*, this work may be reproduced without authorization under the conditions for “Fair Dealing.” Therefore, limited reproduction of this work for the purposes of private study, research, education, satire, parody, criticism, review and news reporting is likely to be in accordance with the law, particularly if cited appropriately.

# Approval

**Name:** Victoria Emma Loosemore  
**Degree:** Master of Science (Physics)  
**Title:** *Optical tweezers-based microrheological measurements using a high-speed camera*  
**Examining Committee:** **Chair:** Eldon Emberly  
Associate Professor

**Nancy Forde**  
Senior Supervisor  
Associate Professor

---

**John Bechhoefer**  
Supervisor  
Professor

---

**Barbara Frisken**  
Internal Examiner  
Professor

---

**Date Defended:**

May 18, 2017

---

# Abstract

Collagen, the most abundant protein in the body, assembles into an extra-cellular fibrillar gel, which has both viscous and elastic properties. These properties can be determined by using optical tweezers to hold a micron-sized bead within the sample. Measurement of the bead's thermally induced motion enables the determination of the frequency-dependent viscoelasticity. Rather than only probing response at a single location, holographic optical tweezers create multiple, independent traps, permitting simultaneous tracking of multiple embedded beads and characterization of their correlated motion. By using this technique in a collagen gel, we will be able to determine local and cross-correlated viscoelastic properties, which vary at different locations during its formation. Implications of this research lie in the fields of health and biomaterials.

The aim of this work is to devise and validate protocols for using holographic optical tweezers to measure local and through-space viscoelasticity. Rather than using laser deflection to track particle motion, I use a high-speed camera and image analysis to track the simultaneous motion of multiple beads. This approach provides nanometer-scale resolution of particle position at sampling rates up to 2.5 kHz. I compare tracking data collected from the high-speed camera to those collected by the laser deflection method and find a discrepancy in the perceived motion of the bead. I perform many experimental tests to assess the root of this problem.

Additionally, I numerically represent bead motion measurements if collected using both methods (laser-deflection method and high-speed camera method) and compare them to the idealized measurement results. In doing so, I learn about the limitations of each method, and how the viscous and elastic properties inferred from the data are affected by each measurement device.

Finally, based on my numerical representations, I suggest a simple procedure to gain more accuracy in the viscous and elastic properties for both simple fluids (such as water) and complex fluids (such as collagen solutions) when using each method. This procedure can be used in future holographic optical tweezers-based experiments to obtain an accurate representation of the local and correlated properties of collagen.

**Keywords:** Optical Tweezers; Microrheology

# Acknowledgements

I would like to thank, first and foremost, my amazing supervisor, Nancy Forde. She continually believed in me and my abilities throughout the last several years, and I am deeply grateful for her support.

Special thanks also to all of the members of the Forde lab who have come and gone these last few years. Particularly to Mike Kirkness, Chapin Korosec, Aaron Lyons and Martin Zuckermann for fruitful discussions and feedback, and for helping to prepare me for my defense; to Alaa Al-Shaer and Teo Penkov for their friendship and for being endlessly distracting yet awesome office-mates; and also to Tuba Altindal for teaching me the ropes of the optical tweezers instrument.

Lastly, I'd like to thank all those who provided help during my classes at SFU. In particular, Brendin Chow and Justine Munich, who saw me through some of the toughest assignments and tests.

# Table of Contents

Approval	ii
Abstract	iii
Acknowledgements	v
Table of Contents	vi
List of Figures	viii
<b>1 Introduction</b>	<b>1</b>
<b>2 Microrheology: properties of fluids on the micrometer scale</b>	<b>4</b>
2.1 Rheology and the study of fluids . . . . .	4
2.2 Microrheology . . . . .	7
2.3 Dynamics of a trapped bead . . . . .	8
2.4 Analysis methods for microrheology . . . . .	8
2.4.1 The power spectrum . . . . .	8
2.4.2 Viscous and elastic moduli . . . . .	10
2.5 Microrheology of water . . . . .	11
2.6 Microrheology of a complex fluid . . . . .	12
<b>3 Optical tweezers for microrheological experiments</b>	<b>14</b>
3.1 Application and principles of optical tweezers . . . . .	14
3.2 The optical tweezers instrument . . . . .	17
3.3 Microrheology measurements and analysis . . . . .	20
3.3.1 QPD microrheology analysis . . . . .	20
3.3.2 High-speed camera microrheology analysis . . . . .	22
3.4 Effects of limited detection bandwidth on the viscoelastic moduli . . . . .	26
<b>4 Optical tweezers-based experiments of a bead in water using a high-speed camera</b>	<b>28</b>
4.1 Experimental power spectra . . . . .	28

4.1.1	Position-sensitive diode-derived power spectra . . . . .	30
4.1.2	Surface effects . . . . .	30
4.2	Effects of laser power on power spectra . . . . .	33
4.3	A different fitting method for the PSD . . . . .	35
4.4	Variance of a bead as measured by the QPD and high-speed camera . . . . .	36
4.4.1	Down-sampling of the QPD position data . . . . .	39
4.5	Varying the frame rate of the high-speed camera . . . . .	40
4.6	Conclusions from the OT-based experiments of a bead in water using the high-speed camera . . . . .	44
<b>5</b>	<b>Numerical representations of microrheological experiments using opti- cal tweezers</b>	<b>46</b>
5.1	Introduction to the program . . . . .	46
5.1.1	Numerical representation of the theoretical data . . . . .	47
5.1.2	Numerical representation of QPD-like data . . . . .	49
5.1.3	Numerical representation of the camera-like data . . . . .	52
5.2	Comparison of camera-like, QPD-like, and theoretical data . . . . .	54
5.2.1	The effects of varying corner frequency on the viscous and elastic outputs . . . . .	58
5.2.2	Effects of sampling frequency on QPD-like data . . . . .	61
5.2.3	Effects of the frequency spacing between discrete points . . . . .	64
5.3	Achieving better estimates in experiment . . . . .	69
5.3.1	Interpolating data from a complex fluid . . . . .	70
<b>6</b>	<b>Conclusions and Future Directions</b>	<b>78</b>
	<b>Bibliography</b>	<b>82</b>
	<b>Appendix A Mathematical model Matlab code</b>	<b>88</b>
	<b>Appendix B Calculation of Equation 5.3</b>	<b>95</b>

# List of Figures

Figure 1.1	Schematic of a bead trapped by a focused laser beam. . . . .	1
Figure 1.2	Multiple trapped beads embedded within collagen network. . . . .	3
Figure 2.1	Example shear moduli for Newtonian, solid, and viscoelastic fluids.	7
Figure 2.2	Expected power spectral density for a bead in water. . . . .	9
Figure 2.3	Expected complex response function for a bead in water. . . . .	11
Figure 2.4	Expected complex shear modulus for a bead in water. . . . .	12
Figure 2.5	Complex shear modulus for PEO. . . . .	13
Figure 3.1	Forces on a bead within an optical trap. . . . .	16
Figure 3.2	Schematic of our optical tweezers instrument. . . . .	18
Figure 3.3	Diagram of a sample chamber for the optical tweezers instrument. .	18
Figure 3.4	A schematic of a quadrant photodiode (QPD). . . . .	19
Figure 3.5	Bead positions measured by the camera and QPD for calibration. .	21
Figure 3.6	Positions as from the camera versus those from the QPD. . . . .	22
Figure 3.7	Power spectral density of a stuck bead as collected by the camera. .	23
Figure 3.8	Images in the sequence resulting from shifting pixels. . . . .	24
Figure 3.9	Positions from the analysis program for a bead computational shifted.	25
Figure 3.10	PSD from a bead compared to the same images but rotated 90°. . .	26
Figure 3.11	Complex shear modulus from data for a bead in water (QPD). . . .	27
Figure 4.1	Experimental PSD from the camera and QPD with Lorentzian fits.	29
Figure 4.2	Positions from the position sensitive diode and camera. . . . .	31
Figure 4.3	PSD from the position sensitive diode and the camera. . . . .	31
Figure 4.4	Power spectra at different distances from a surface. . . . .	32
Figure 4.5	Corner frequency as a function of laser power. . . . .	33
Figure 4.6	Diffusion constant as a function of laser power. . . . .	34
Figure 4.7	A bead trapped with two different laser powers. . . . .	35
Figure 4.8	Power spectrum multiplied by frequency squared. . . . .	36
Figure 4.9	Position of bead as a function of time from the QPD and camera. .	37
Figure 4.10	Position of a bead during calibration. . . . .	38
Figure 4.11	Normalized histograms of the position of a bead. . . . .	38
Figure 4.12	Down-sampled position of bead from the QPD. . . . .	39

Figure 4.13	Power spectra for down-sampled PSD. . . . .	40
Figure 4.14	Variance versus the reciprocal of the effective sampling frequency. . .	41
Figure 4.15	Camera variance vs. integration time . . . . .	42
Figure 4.16	Same bead at two different integration times. . . . .	43
Figure 4.17	Variance as a function of image intensity in the camera images. . .	43
Figure 4.18	Diffusion constant ratio of camera to QPD as a function of laser power.	45
Figure 4.19	Experimental complex shear modulus from the QPD and camera. . .	45
Figure 5.1	The theoretical power spectral density. . . . .	48
Figure 5.2	Theoretical $A'(f)$ and $A''(f)$ . . . . .	48
Figure 5.3	Theoretical $G'(f)$ and $G''(f)$ . . . . .	49
Figure 5.4	The numerically calculated QPD-like power spectral density. . . . .	50
Figure 5.5	QPD-like $A'(f)$ and $A''(f)$ including aliasing. . . . .	51
Figure 5.6	QPD-like $G'(f)$ and $G''(f)$ including aliasing. . . . .	51
Figure 5.7	Camera-like power spectral density including aliasing and blur. . .	52
Figure 5.8	Camera-like $A'(f)$ and $A''(f)$ including aliasing and blur. . . . .	53
Figure 5.9	Camera-like $G'(f)$ and $G''(f)$ including aliasing and blur. . . . .	53
Figure 5.10	Power spectra for theoretical, QPD-like, and camera-like data. . . .	55
Figure 5.11	$G'(f)$ and $G''(f)$ for the theoretical, QPD-like, and camera-like data.	55
Figure 5.12	Ratios of $G'(f)$ and $G''(f)$ of device-like to theoretical data. . . . .	56
Figure 5.13	$A'(f)$ and $A''(f)$ for the theoretical and device-like data. . . . .	57
Figure 5.14	Numerical $G'(f)$ and $G''(f)$ with $f_c = 50$ Hz. . . . .	58
Figure 5.15	Numerical $G'(f)$ and $G''(f)$ with $f_c = 200$ Hz. . . . .	59
Figure 5.16	Numerical $G'(f)$ and $G''(f)$ with $f_c = 350$ Hz. . . . .	59
Figure 5.17	Cut-off frequency versus corner frequency. . . . .	60
Figure 5.18	Viscosity versus corner frequency . . . . .	60
Figure 5.19	$G'_{\text{trap}}$ versus corner frequency. . . . .	61
Figure 5.20	QPD-like $A'(f)$ for different sampling frequencies. . . . .	62
Figure 5.21	Complex shear modulus for QPD-like $f_s = 2500$ Hz. . . . .	63
Figure 5.22	Changing the frequency step sizes that lead to the QPD-like $A'(f)$ .	65
Figure 5.23	Changing the frequency step sizes of the camera-like $A'(f)$ . . . . .	66
Figure 5.24	QPD-like complex shear modulus for different $df$ . . . . .	67
Figure 5.25	Camera-like complex shear modulus for different $df$ . . . . .	68
Figure 5.26	PSD from the QPD with interpolated points. . . . .	70
Figure 5.27	Complex shear modulus for values corresponding to experimental data.	71
Figure 5.28	Interpolated and non-interpolated QPD complex shear modulus. . .	72
Figure 5.29	Experimental PSD data from the camera with interpolated points.	72
Figure 5.30	Interpolated and non-interpolated camera complex shear modulus.	73

Figure 5.31	Experimental PSD for the positions of a bead in collagen with interpolation. . . . .	74
Figure 5.32	QPD complex shear modulus for collagen with interpolation. . . . .	75
Figure 5.33	Camera complex shear modulus for collagen with interpolation. . . . .	76

# Chapter 1

## Introduction

The goal of this thesis is to develop techniques to utilise measurements from a high-speed camera used to image optical tweezers experiments, in order to study the viscous and elastic properties of fluids.

Optical tweezers use a focused laser beam to trap a micron-sized particle, as shown in Figure 1.1. The trapped bead is able to undergo short-range thermal fluctuations but long-range movement is prohibited. Careful analysis of the motion of the bead provides insight into the properties of the fluid in which the bead and trap are immersed. For instance, given the same amount of thermal energy, a bead would behave differently in water than in air. Both water and air have Newtonian, or purely viscous, fluidic properties. Water has a higher viscosity than air, meaning it creates more drag on an immersed object. Drag reduces the movement of a particle.

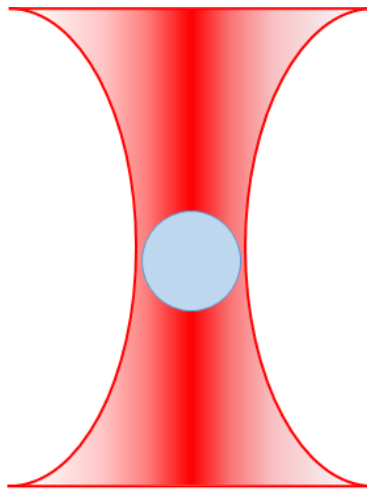


Figure 1.1: Schematic of a bead trapped by a focused laser beam.

There is also another class of fluids known as non-Newtonian. Common examples include mayonnaise, paint, and toothpaste. A bead immersed in these fluids would exhibit different

behaviour than in water or air because non-Newtonian fluids store energy, as well as dissipate it. Viscoelastic fluids can both store (elasticity) and dissipate (viscosity) energy. Therefore, non-Newtonian fluids have viscoelasticity. Silly putty, the child's toy, is another example of a viscoelastic fluid. For forces acting over long times, silly putty flows and therefore, exhibits liquid-like behaviour. But for forces acting over short times, it will act elastically. For example, if dropped, it will bounce, but if left to rest, it will flow under the force of gravity. The study of the viscous and elastic properties of fluids is known as 'rheology' and making measurements of rheological properties using micron-sized particles is known as 'microrheology'.

Collagen, a very abundant structural protein in vertebrates, also exhibits viscoelastic behaviour, the properties of which are linked to its macromolecular characteristics. Collagen molecules self-assemble to form fibrils with well-ordered structures, which, in turn, can assemble into networks or fibres. These viscoelastic hierarchical structures are found in tendon, skin, bone, and cartilage, where they provide strength and flexibility, and in the extracellular matrix, where they provide structural and biochemical support [1, 2, 3, 4].

The mechanism of collagen's self-assembly at the molecular level is important for understanding physiological processes such as extracellular remodelling during cancer metastasis [5], keloid scar formation during wound healing [6], and stem-cell death [7]. In bioengineering, the process of collagen fibril and network formation will allow for better design of cellular growth substrates for cellular engineering studies [8, 9] and tissue engineering for the reparation of bones and ligaments [10]. Additionally, a deficiency or mutation of collagen can cause diseases such as osteoarthritis and osteogenesis imperfecta [11, 12]. Understanding the mechanism of collagen formation may lead to improvements in treatment of these and other diseases.

Previous studies of the microrheological properties of collagen have shown that at different locations within collagen fibrillar gels during and after formation, the elastic and viscous properties vary significantly [13, 14, 15]. As a result, it would be instructive to probe multiple points throughout a network during formation to understand and characterize how these collagen molecules come together and form the higher order structures.

With multiple beads in a collagen gel, not only will each bead provide a rheological picture of its surroundings, but the cross-correlated motions, how the motion of one bead at one location affects another bead at a different location [18], will illuminate the growth mechanism of the gel.

To study the different locations simultaneously, we need to trap and monitor positions of multiple particles. Holographic optical tweezers (HOT) provides a method for patterning a single laser beam into multiple, independent traps. Figure 1.2 shows a schematic of multiple trapped particles before and after formation of a collagen gel.

The HOT instrument in our lab has been built and calibrated for force measurements on a single trapped bead [16]; however, for taking rheological measurements of multiple

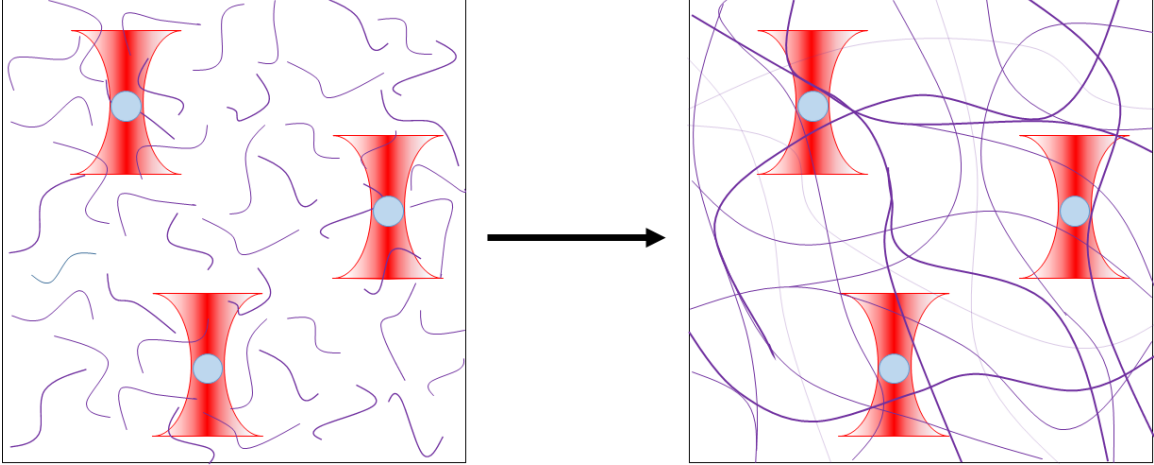


Figure 1.2: Multiple trapped beads embedded within a solution of collagen molecules (left), which come together to create a collagen network (right). Probing multiple locations simultaneously and cross-correlating particle motions will help characterize the mechanism of collagen gel formation.

particles simultaneously, a high-speed camera to observe the motions of each particle is necessary. Some calibration work has been done using the high-speed camera [17]; however, it had not been employed for non-Newtonian fluids.

In this thesis, I introduce the high-speed camera as a method of observing a single bead's position and performing optical tweezers-based microrheology analysis for this bead in water, though the ultimate goal of using the high-speed camera is to allow for multi-particle holographic optical tweezers-based microrheology analysis of cross-correlated viscoelastic properties of gel forming processes such as collagen gels.

My thesis starts with an introduction to microrheology and the analysis techniques used (Chapter 2), followed by a chapter on the optical tweezers instrument and how it is used for the microrheology experiments (Chapter 3). In Chapter 4, I present the experiments I performed using the high-speed camera for the microrheological measurements. Chapter 5 includes numerical representations of the expected outcomes of the experiments which lead to some suggestions for future improvements of the microrheological analysis, followed by a summary (Chapter 6).

## Chapter 2

# Microrheology: properties of fluids on the micrometer scale

### 2.1 Rheology and the study of fluids

Rheology, the study of the flow and deformation of matter, quantifies the way in which materials respond to applied stress or strain. Certain materials dissipate the applied energy through viscous flow, while others respond elastically, storing the energy in a completely reversible deformation, and there are still others whose response to deformation is characterized by a combination of both viscous and elastic responses, consequently referred to a viscoelastic response. The behaviour of viscoelastic materials under force cannot be defined simply by elastic and viscous constants; rather, these are functions of time (or frequency), direction, and magnitude of the applied force [19]. Rheological experiments aim to probe a material over a wide frequency range and relate its viscoelastic response to the structure of the material.

All materials have rheological properties; hence Heraclitus' phrase '*panta rei*', which means 'everything flows'. The phrase was used to coin the term 'rheology' in 1929 [20]. However, human interest in rheological properties dates back to well before the 20th century from the use of water clocks in ancient Egypt [21] to the 17th century when Isaac Newton, whose famous *Principia* discusses the response of water, air, and mercury to the shearing motion of a pendulum [22].

Rheology is relevant in many fields of study in modern science including the food processing industry, where texture and consistency affect taste [23, 24], the processing of plastics for commercial materials [25], the geological sciences, where it describes the deformation and creep of rock structures [26], soil properties for ideal plant growth [27], and is used to model landslides [28], among many other applications.

In the biological sciences, viscoelasticity is integral to the functions of cells, whose mechanical properties are essential for mechanisms such as cell growth, stem-cell differentia-

tion, cell crawling, wound healing, protein regulation, cell malignancy, and even cell death [29, 30]. Particularly relevant here, structural proteins such as collagen rely on their mechanical structure to provide tensile strength to connective tissues such as tendon, bone, skin, and cartilage, and to contribute structural and biochemical support to the extracellular matrix, which surrounds cells [13].

Under an applied stress  $\sigma$ , a purely elastic material will deform proportional to the strain of the material,  $\gamma$ . For small amounts of stress, an elastic material will follow a linear relationship between stress and strain [19],

$$\sigma = E\gamma, \quad (2.1)$$

where  $E$  is the elastic modulus, also called Young's modulus.

By contrast, a purely viscous fluid, also known as a Newtonian fluid after Newton's aforementioned studies, flows under stress and is therefore characterized by its viscosity,  $\eta$  and rate of strain, [31]

$$\sigma = \eta \left( \frac{d\gamma}{dt} \right). \quad (2.2)$$

The viscoelastic response to stress, however, is more complicated and depends also on the timescale of the deformations. The response in this case can be expressed as a convolution integral that is a function of the time-dependent relaxation of the material,  $G(t)$ , [19]

$$\sigma(t) = \int_{-\infty}^t G(t - \tau) \left( \frac{d\gamma}{d\tau} \right) d\tau. \quad (2.3)$$

The physical realization of the time-dependent relaxation can be best understood for a purely elastic substance. The relaxation time  $\tau$ , in this case, is zero and so  $G(t)$  is proportional to the constant  $E = \sigma/\gamma$ .

The conventional method of measuring the rheological properties is based on the in- and out-of-phase stress response,  $\sigma(\omega, t)$ , to an oscillatory strain,  $\gamma(\omega, t)$ , (or vice versa). It is most useful for this method to express the time-dependent relaxation as the frequency-dependent complex shear modulus,  $G^*(\omega)$ , by taking the Fourier transform of  $G(t)$ . For an oscillatory strain,  $\gamma = \gamma_0 \sin(\omega t)$ , with small amplitude  $\gamma_0$  and angular frequency  $\omega = 2\pi f$ , the resulting strain rate will be  $\frac{d\gamma}{dt} = \omega\gamma_0 \cos(\omega t)$ . Plugging this into Equation 2.3 and substituting  $s = t - \tau$ , we get [19]

$$\begin{aligned} \sigma(t) &= \int_0^\infty G(s)\omega\gamma_0 \cos(\omega(t-s))ds \\ &= \gamma_0 \left( \left[ \omega \int_0^\infty G(s) \sin(\omega s) ds \right] \sin(\omega t) + \left[ \omega \int_0^\infty G(s) \cos(\omega s) ds \right] \cos(\omega t) \right). \end{aligned} \quad (2.4)$$

Since the terms in square brackets are no longer functions of time, it is most convenient to rewrite Equation 2.4 in terms of two values:  $G'(f)$ , the in-phase response, and  $G''(f)$ , the out-of-phase response, also known as the elastic (or storage) modulus and the viscous (or loss) modulus, respectively. Equation 2.4 then becomes [19]

$$\sigma(t) = \gamma_0 (G'(\omega) \sin(\omega t) + G''(\omega) \cos(\omega t)). \quad (2.5)$$

An alternative method of representing these quantities is in terms of the amplitude,  $\sigma_0$ , of the applied stress and the phase lag,  $\delta$ , between the stress and strain. This is written as [19]

$$\sigma(t) = \sigma_0 \sin(\omega t + \delta) = \sigma_0 \sin(\omega t) \cos(\delta) + \sigma_0 \cos(\omega t) \sin(\delta). \quad (2.6)$$

Comparing Equations 2.5 and 2.6 shows that [19]

$$G' = \frac{\sigma_0}{\gamma_0} \cos(\delta) \quad (2.7)$$

$$G'' = \frac{\sigma_0}{\gamma_0} \sin(\delta) \quad (2.8)$$

$$G''/G' = \tan(\delta). \quad (2.9)$$

Equation 2.9, the ratio of the loss to storage modulus, is called the ‘loss tangent’.

The complex shear modulus can be expressed in terms of its real and imaginary parts, the elastic modulus from Equation 2.7 and the viscous modulus from Equation 2.8, respectively, as [31]

$$G^*(f) = G'(f) + iG''(f). \quad (2.10)$$

The loss tangent can be helpful to classify a material as more elastic or more viscous. When the loss tangent is  $G''/G' \gg 1$ , that is a phase lag of  $\delta = \pi/2$  ( $\tan(\pi/2) = \infty$ ), materials are liquid-like, and when  $G''/G' \ll 1$  ( $\delta = 0$ ;  $\tan(0) = 0$ ), materials are solid-like [31]. Newtonian fluids exhibit loss moduli,  $G''(f)$ , that increase linearly with frequency, as shown in Figure 2.1a. The intercept gives the viscosity,  $\eta$ , times  $2\pi$ . Since a purely viscous material does not store energy, the storage modulus,  $G'(f)$ , of a Newtonian fluid is zero at all frequencies. For a solid-like material,  $G'(f)$  is constant, as shown in Figure 2.1b, while the loss modulus is zero. In viscoelastic fluids, both the elastic and viscous moduli depend on frequency, and  $G''/G'$  can change throughout the range of frequencies probed, for example as shown in Figure 2.1c.

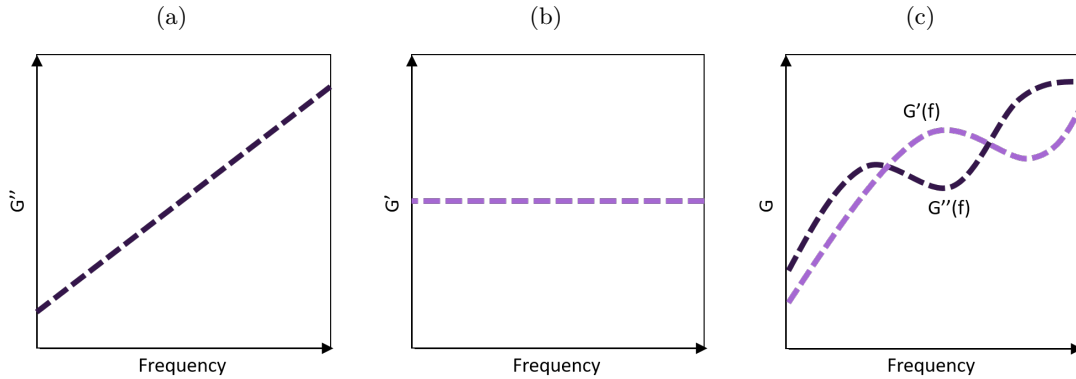


Figure 2.1: Example shear modulus for a (a) Newtonian fluid, (b) solid material and (c) viscoelastic fluid.

## 2.2 Microrheology

As opposed to relying on macroscopic stresses and strains to extract a material's moduli, microrheology detects the displacement of microscopic particles embedded in the material and uses their displacements to estimate the moduli. These displacements can be the result of either thermal fluctuations or an externally applied force. The former is known as passive microrheology, whereas the latter is active microrheology [32].

The advantages of microrheology over conventional bulk rheology are localized probes, smaller volumes of fluid, and a wide range of frequencies over which the properties can be measured. Commercial rheometers typically need millilitres of fluid, average the results over a whole sample, and can typically probe only up to frequencies of tens of Hz [33]. Microrheology techniques offer very localized probing to allow insight into the local heterogeneities of the fluid. Moreover, experiments only require volumes on the order of tens of microlitres ( $\mu\text{l}$ ) of fluid and can probe frequencies up to of 50 kHz [32].

The predominant techniques for microrheology include particle tracking, which examines particles' thermal diffusion trajectories while immersed in a viscoelastic medium [34]; diffusive-wave spectroscopy, analyses the time dependence of the light scattered from a collection of colloidal probe particles embedded in a semi-transparent viscoelastic material [35]; atomic force microscopy, where a microscopic bead is attached to a cantilever and oscillated above the surface of medium [36]; magnetic tweezers, where particles are manipulated in the medium of interest using a magnetic field [37]; and optical tweezers, where particles are trapped using a laser beam, as explained in greater detail in Chapter 3 [32, 38].

Diffusive-wave spectroscopy and particle tracking are passive microrheology techniques, where only the thermal forces are observed, whereas atomic force microscopy and magnetic tweezers techniques apply stresses to the medium to get a response and are thus classified as active microrheology. Optical tweezers can be used for both active and passive microrheol-

ogy [39, 40]. In this thesis, optical tweezers are used to observe the thermal fluctuations of a micron-sized particle within the confines of an optical trap, employing the passive approach to microrheology.

## 2.3 Dynamics of a trapped bead

A bead trapped using optical tweezers is held within a potential that is approximately harmonic, created by gradients in the electric field of the laser beam. It undergoes short-range thermal fluctuations but long-range motion is limited due to the restoring force, which increases with displacement, [41]

$$F = -\kappa x. \quad (2.11)$$

In other words, the trap acts as a Hookean spring, with spring constant or trap stiffness,  $\kappa$ . In Chapter 3, the optical tweezers instrument will be discussed for use as the mechanism of trapping the bead.

The short-range thermal motion of colloidal particles is used to obtain the viscoelastic response of the medium to their motion. This motion is the result of the ceaseless and randomly oriented movement of the molecules associated with the thermal energy of the system. In a purely viscous fluid, such as water, the mean-square displacement in one dimension of a particle is proportional to time via the diffusion constant,  $D$ , [31]

$$\langle x^2 \rangle = 2Dt. \quad (2.12)$$

The diffusion coefficient is related to the friction felt by the bead within the solvent,  $F_{\text{fr}} = -\gamma \frac{dx}{dt}$ , where  $\gamma$  is called the friction or drag coefficient whose value for a sphere of radius  $R$  in an unbounded [*i.e.*, far from any surface], viscous medium of viscosity  $\eta$  is  $\gamma = 6\pi\eta R$  [31]. The diffusion constant of a spherical bead, [31]

$$D = \frac{k_B T}{\gamma}, \quad (2.13)$$

is called the Stokes-Einstein relation, where  $k_B$  is the Boltzmann constant and  $T$  is the temperature.

## 2.4 Analysis methods for microrheology

### 2.4.1 The power spectrum

The one-dimensional diffusive motion of a particle in an optical trap can be used to calculate the power spectral density (PSD) of the particle's position. The PSD is an important step to

recovering the components of the complex shear modulus. It is calculated by the square of the Fourier transform (transformation from the time to frequency domain) of the particle's displacement:

$$PSD(f) = \frac{2|\tilde{x}(f)|^2}{T_{\text{msr}}}, \quad (2.14)$$

where  $\tilde{x}(f)$  is the Fourier transform of the particle's position,  $x(t)$ , and  $T_{\text{msr}}$  is the measurement time. For a trapped, spherical bead in a Newtonian fluid the power spectral density (PSD) of displacements takes the form of a Lorentzian function, [42]

$$PSD(f) = \frac{D}{\pi^2} \times \frac{1}{(f^2 + f_c^2)}. \quad (2.15)$$

This is the single-sided form of the PSD where  $D$  is the diffusion constant of the bead in the medium,  $f$  is the frequency, and  $f_c$  is the corner frequency. Figure 2.2 shows Equation 2.15 plotted as a function of frequency, with  $f_c = 100$  Hz and  $D = 0.226 \mu\text{m}^2 \cdot \text{Hz}$ . The corner frequency is the frequency at which the plateau at low frequencies, the frequencies over which the particle is confined (*i.e.*, over longer times), changes to the PSD decaying proportionally to  $f^{-2}$  at high frequencies, at which the particle freely diffuses, according to Equation 2.12, without feeling the confinement.

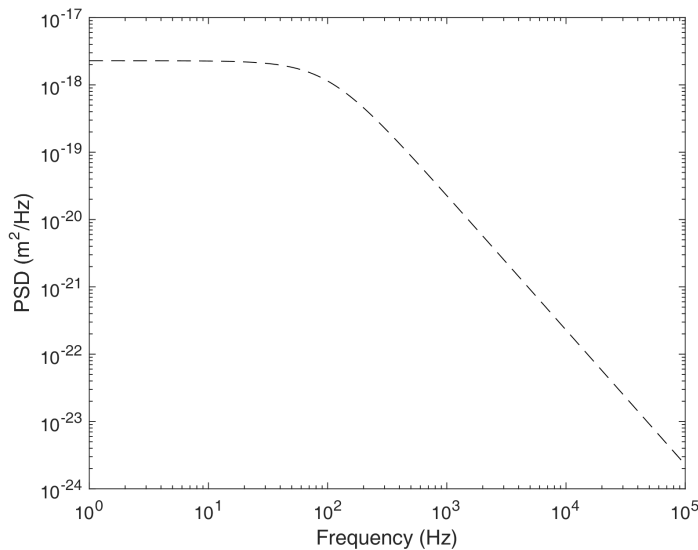


Figure 2.2: Equation 2.15 plotted with  $D = 0.226 \mu\text{m}^2 \cdot \text{Hz}$  and  $f_c = 100$  Hz. Notice the change from plateau to decay at  $f = 100$  Hz.

The amount of space the particle is able to explore, and hence the corner frequency, depends on the trap stiffness. The trap stiffness is related to the variance of the bead,  $\langle x^2 \rangle$ ,

by

$$\kappa = \frac{k_B T}{\langle x^2 \rangle}, \quad (2.16)$$

which has been derived from the equipartition theorem [43]. Then the corner frequency is [42]

$$f_c = \frac{\kappa}{2\pi\gamma}. \quad (2.17)$$

## 2.4.2 Viscous and elastic moduli

The complex shear modulus can be obtained following the work of Addas *et al.* [44]. The fluctuation-dissipation theorem relates the magnitude of the fluctuating force to the energy dissipation. Then a Kramers-Kronig relation determines the complex response of the material to fluctuations. This response connects the Fourier transform of the particle's displacement,  $\tilde{x}(f)$ , to the Fourier transform of the force,  $\tilde{F}(f)$ , as  $\tilde{x}(f) = A^*(f) \cdot \tilde{F}(f)$ , where  $A^*(f) = A'(f) + iA''(f)$ .

The dissipation of thermal energy,  $k_B T$ , relates to the power spectrum of a particle's displacement (fluctuations) by [44]

$$A''(f) = \frac{\pi f}{2k_B T} \times PSD(f) = \frac{Df}{2\pi k_B T(f^2 + f_c^2)}, \quad (2.18)$$

where  $A''$  is the imaginary part of the complex response function. To obtain the real part of the response function, the Kramers-Kronig relation is used, giving

$$A'(f) = \frac{2}{\pi} \int_0^\infty \frac{\xi A''(\xi)}{(\xi^2 - f^2)} d\xi. \quad (2.19)$$

Figure 2.3 shows the real and imaginary parts of the complex response represented mathematically by Equations 2.18 and 2.19 with  $f_c = 100$  Hz,  $D = 0.226 \mu\text{m}^2/\text{Hz}$  and  $T = 295$  K.

Finally the complex shear modulus can be calculated via the generalized Stokes-Einstein relation [44] to give

$$G^*(f) = \frac{1}{6\pi R A^*(f)}. \quad (2.20)$$

$R$  is the radius of the probe particle. Through this definition,  $G''$  should be negative but, by convention, its magnitude will be taken. Figure 2.4 shows the expected complex shear

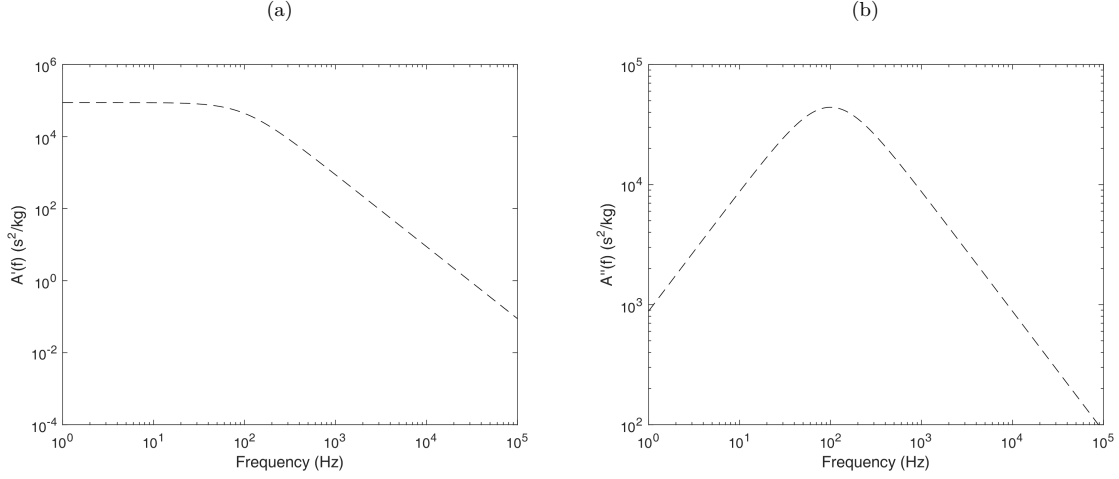


Figure 2.3: Expected (a) real (Equation 2.19) and (b) imaginary (Equation 2.18) parts of the complex response function due to the fluctuations of a bead in water with  $f_c = 100$  Hz,  $D = 0.226 \mu\text{m}^2 \cdot \text{Hz}$  and  $T = 295$  K.

modulus of a bead in water. Both  $A'$  and  $A''$  contribute (unequally) to  $G'$  and  $G''$  as

$$G'(f) = \frac{1}{6\pi R} \left( \frac{A'}{A'^2 + A''^2} \right) \quad (2.21)$$

$$G''(f) = \frac{1}{6\pi R} \left( \frac{A''}{A'^2 + A''^2} \right). \quad (2.22)$$

## 2.5 Microrheology of water

The elastic modulus of a purely viscous medium such as water should be zero, however in Figure 2.4, this is clearly not the case. The values of  $G'(f)$  are not those from the medium but those of the trap. The confinement results in an effective elastic modulus, meaning  $G'_{\text{measured}} = G'_{\text{medium}} + G'_{\text{trap}}$  [44]. This elasticity does not affect the viscous modulus and can be corrected by [45]

$$G'_{\text{medium}} = G'_{\text{measured}} - \frac{\kappa}{6\pi R}, \quad (2.23)$$

for a bead of radius  $R$  in a trap with stiffness  $\kappa$ . There are multiple methods of realizing this correction for purely viscous and viscoelastic media; however, in this thesis, only uncorrected  $G'(f)$  values are presented. Since  $G'_{\text{water}} = 0$ , the elastic modulus measured should be

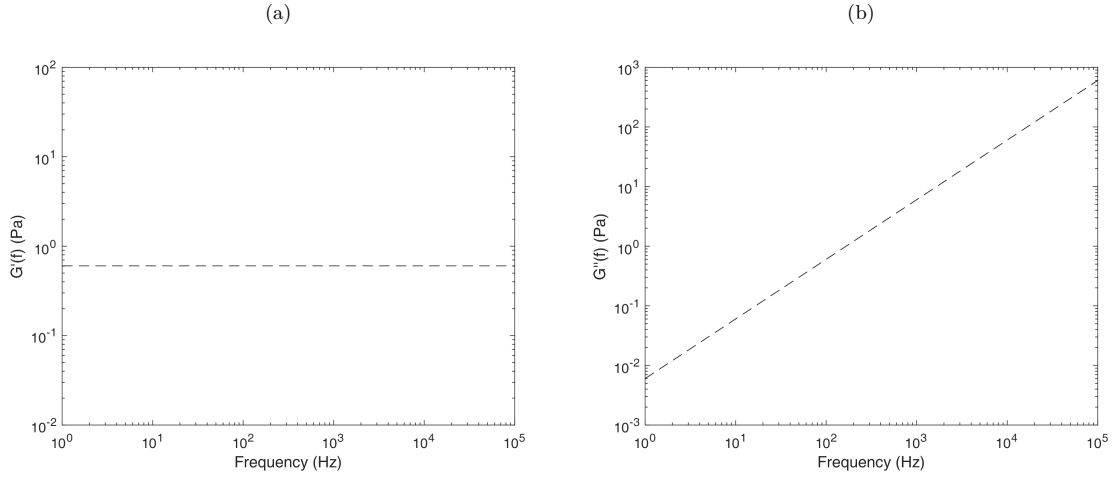


Figure 2.4: Expected (a) elastic modulus (Equation 2.21) and (b) viscous modulus (Equation 2.22) for a bead of radius  $R = 1 \mu\text{m}$  trapped in water, with  $f_c = 100 \text{ Hz}$ ,  $D = 0.226 \mu\text{m}^2 \cdot \text{Hz}$  and  $T = 295 \text{ K}$ .

$$G'_{\text{meas}} = \frac{\kappa}{6\pi R} = 2\pi\eta f_c, \quad (2.24)$$

using the relationship in Equation 2.17 to relate it to the values of the PSD.

The dynamic viscosity of a purely viscous fluid is independent of frequency and the viscous modulus results in [46]

$$G''(f) = 2\pi\eta f. \quad (2.25)$$

Therefore, when the viscous modulus is plotted as a function of frequency are plotted on logarithmic scales, a linear relation with a slope of 1 and intercept  $\log(2\pi\eta)$  is expected.

## 2.6 Microrheology of a complex fluid

Collagen solutions and gels are characterized by both viscous and elastic properties [13], and therefore exhibit richer frequency dependence than a Newtonian fluid like water. The approach of obtaining  $G^*(f)$  described in the previous sections has been validated in our lab for a non-Newtonian fluid. Figure 2.5 shows the complex shear modulus of PEO (polyethylene oxide) as measured by optical tweezers, diffusing-wave spectroscopy and bulk rheology [13, 47]. These are in excellent agreement for frequencies of 10 Hz to 1000 Hz.

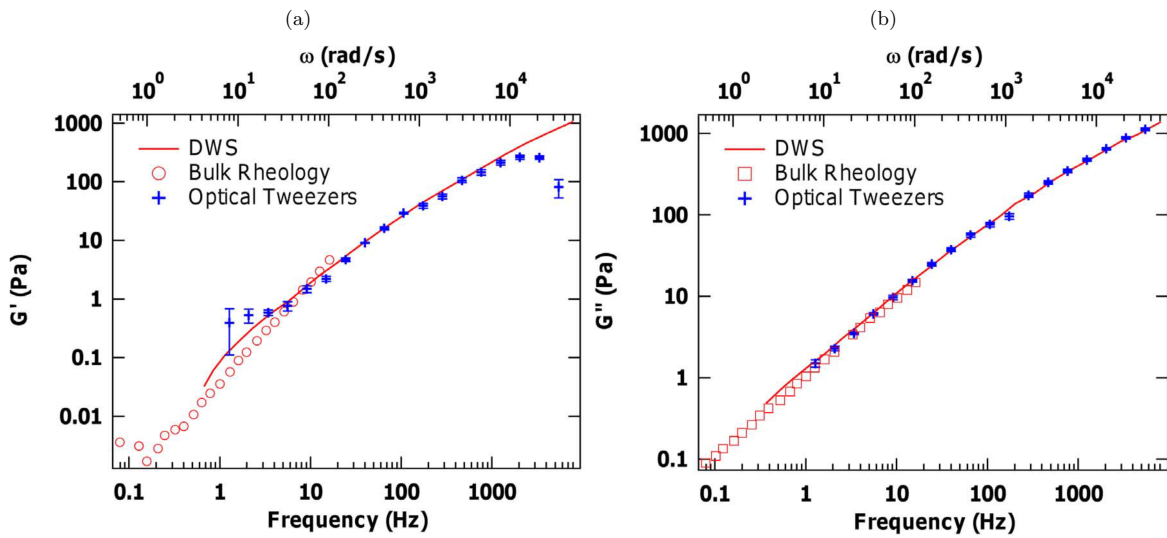


Figure 2.5: The (a) elastic and (b) viscous moduli of 6.7 wt% PEO obtained using optical tweezers (crosses) (from [13]), diffusing wave spectroscopy (DWS; solid line) and bulk rheology (open symbols) (from [47]). Crosses indicate the mean values over five independent measurements, and error bars represent the standard error of the mean. Figure adapted from [13].

## Chapter 3

# Optical tweezers for microrheological experiments

For the work described in this thesis, microrheological experiments are performed using optical tweezers (OT). Since their advent, optical tweezers have been used to trap microscopic objects such as viruses, living cells, and dielectric spheres within their highly focused laser beam and manipulate them with pN-scale forces in various applications in the biological and physical sciences [48]. For microrheology, optical tweezers provide highly localized probing of the viscous and elastic properties of a fluid. This chapter will cover an introduction to the mechanisms of optical trapping and provide the specifics of our apparatus and the data analysis protocol that we use for the microrheological experiments.

### 3.1 Application and principles of optical tweezers

The use of radiation pressure as a means of confining a microscopically sized particle was developed and realized by Arthur Ashkin in the 1970s and 80s [49, 50]. Since then, the technique has been employed to manipulate microscopic objects for many applications, such as sorting particles into different configurations [51, 52] and assembling semiconductor nanowires [53, 54]. The displacements of a trapped particle have proven useful not only in microrheology [32] but also in studies of the hydrodynamics of colloids [55] and nonequilibrium thermodynamics [56, 57, 58]. Optical tweezers have been particularly embraced by the biological sciences due to their small applied forces. The technique has been used to trap bacteria and monitor their movements [59, 60], to measure the forces exerted by molecular motors [61, 62, 63], and to measure the elasticity and unzipping forces of single DNA molecules [64, 65, 66]. OT have also been used to trap viruses, living cells, and other organelles [67, 68, 69]. The technique has been extended to trap multiple particles simultaneously [70, 71], as will be discussed. Neuman and Block [41] have written a comprehensive

review of optical trapping and its biological applications, to which the content of this section is indebted.

A differential intensity gradient across the optical axis of a laser beam results in a nearby dielectric particle experiencing a force towards the centre of the beam. This intensity gradient is created by using a laser beam with a gradient in the transverse direction (e.g., with a Gaussian intensity profile) and tightly focusing it through an objective lens with a high numerical aperture (NA). As the light interacts with the micron-sized particle, the photons are refracted and scattered, culminating in an exchange of momentum between the light and the bead. By Newton's third law, the change in momentum of the photons leads to an opposite reaction for the bead.

Despite incident light being scattered in a variety of directions, the force due to the reflection and absorption of the photons pushes the bead along the optical axis, since, for a bead centred on the optical axis, all scattered forces will cancel except in this direction. A second force due to the gradient in the beam can be experienced from the refraction of light through the bead. If it has a higher refractive index than the surrounding medium, this force will be directed towards the region of higher light intensity, *i.e.*, the centre of the beam. This gradient force acts both along the optical axis and in transverse directions.

Figure 3.1 illustrates these forces acting on a dielectric particle within a focused beam. When the bead moves laterally, the highest intensity rays at the beam centre will contribute most strongly, deflecting through the bead and imparting a restoring force. A three-dimensional stable trap occurs when the gradient force is stronger than the scattering force.

The displacement and subsequent restoring force acting upon the bead can be described in terms of a potential well in which long-range displacements are limited but short-range thermal fluctuations are allowed. In this sense, the optical trap can be thought of as a Hookean spring-like system, and the microrheology analysis presented in Chapter 2 can apply to this system. The spring constant,  $\kappa$ , defines the trap stiffness and is proportional to the intensity of laser light creating the trap.

The case for which the optical forces can be computed directly from ray optics (Figure 3.1) is called the Mie regime. In this regime, the size of the trapped sphere is much larger than the wavelength of the laser light, *i.e.*,  $R \gg \lambda$ , and the conditions for Mie scattering are satisfied. Conversely, the case where the  $R \ll \lambda$  is in the Rayleigh regime, where Rayleigh scattering conditions are met. In this regime, the particle is treated as a point dipole induced by the electromagnetic field of the incident light. The scattering force is given by

$$F_{\text{scatt}} = \frac{I\sigma n_m}{c}, \quad (3.1)$$

where  $\sigma = \frac{128\pi^5 R^6}{3\lambda^4} \left(\frac{m^2-1}{m^2+2}\right)^2$  is the scattering cross-section of the particle,  $I$  is the intensity of the incident light,  $c$  is the speed of light, and  $m = \frac{n_p}{n_m}$  is the ratio of the particle's

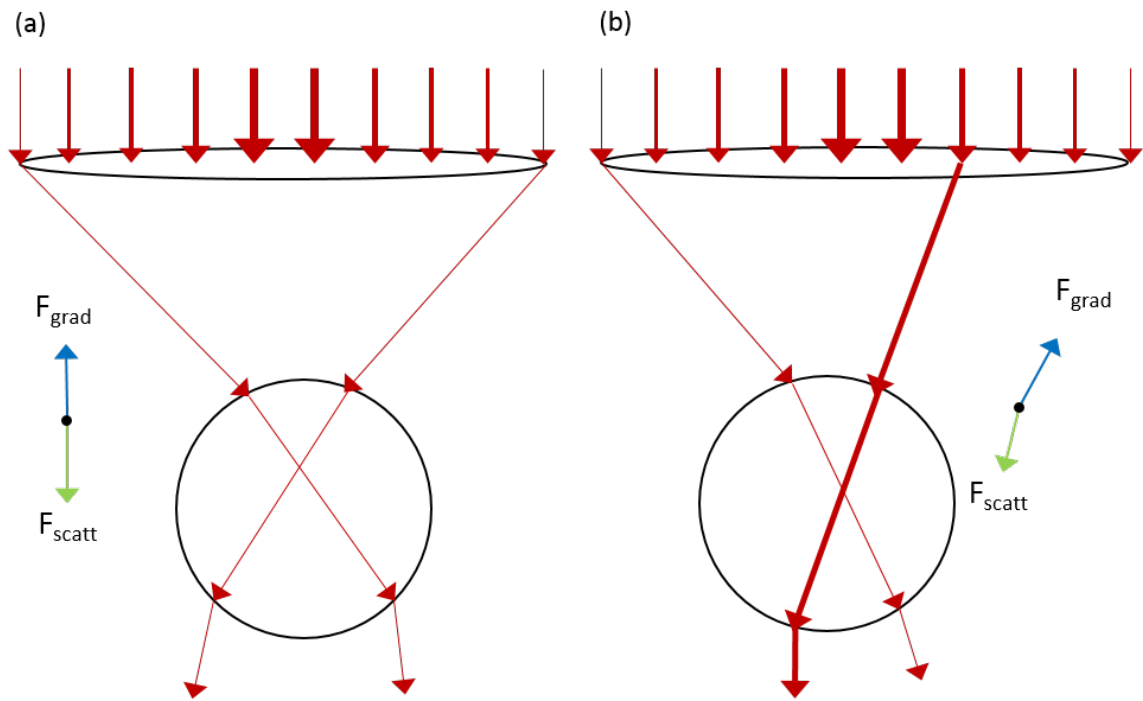


Figure 3.1: Scattering and gradient forces arising due to reflection/absorption and refraction, respectively, of a Gaussian profiled laser beam incident on a dielectric bead within a medium of lower refractive index than the particle. The thickness of the red arrows represents the intensity of the light. The bead experiences no net force while at the centre of the trap (a) but feels a net force towards the centre of the trap when off-centre (b).

refractive index,  $n_p$ , to the medium's refractive index,  $n_m$  [41]. The gradient force from the dipole interaction with the light is

$$F_{\text{grad}} = \frac{2\pi\alpha}{cn_m^2} \nabla I, \quad (3.2)$$

where the polarizability of the sphere is given by  $\alpha = n_m^2 R^3 \left( \frac{m^2 - 1}{m^2 + 2} \right)$  [41]. The scattering force is proportional to the intensity and points in the direction of propagation of the incident light, while the gradient force is proportional to the intensity gradient and is applied in the direction of the highest gradient when  $m > 1$ .

Unfortunately, for most practical cases, neither regime is valid because  $R \approx \lambda$ , and more careful analysis of electromagnetic theory is necessary [72, 73]. However, this analysis provides little added benefit to the treatment here and confirms that an optical trap can be treated locally as a harmonic potential.

As mentioned, optical tweezers have been found useful for a variety of applications [48]. The most relevant extension for these studies is the holographic optical tweezers (HOT) [70, 71]. This technique uses a single laser to establish multiple independent traps by spatially imprinting local phase modulations [16]. These traps can be manipulated individually in three dimensions in real time. This technique has a wide range of applications; in particular it can be used for multiple-particle microrheology [74]. The aim of this thesis is to establish techniques for implementation of HOT to study the inhomogeneous behaviour of collagen networks [13].

## 3.2 The optical tweezers instrument

The optical tweezers instrument used, shown schematically in Figure 3.2, has been previously described [16] and adapted for microrheological experiments by Marjan Shayegan [13, 45]. In brief, a 1064 – nm laser is directed towards a water-immersion objective lens with  $NA = 1.2$  via several lenses and mirrors, including a spatial light modulator (SLM). The SLM is used for HOT experiments; here, however, it is off and simply acts as a mirror. The laser intensity reaching the objective, and therefore the trap stiffness, is adjusted by the combination of a half-wave plate and polarizing beam splitter.

The optical trap is formed in a sample chamber, a diagram of which is shown in Figure 3.3. The chamber consists of two microscope coverslips separated by two thin strips of Parafilm or Nescofilm on opposing edges, leaving a slot of approximately 120  $\mu\text{m}$  in thickness. The wax film is melted to create a good seal. A micropipette is used to insert into the chamber the medium of interest to which polystyrene, 2.89  $\mu\text{m}$  diameter beads (Spherotech) have been added at a concentration of  $7 \times 10^{-4}\%$  w/v. At this concentration, it is possible to trap a single bead without interference from other particles. A volume of approximately 20  $\mu\text{l}$  of the medium/bead mixture is necessary to fill the sample chamber,

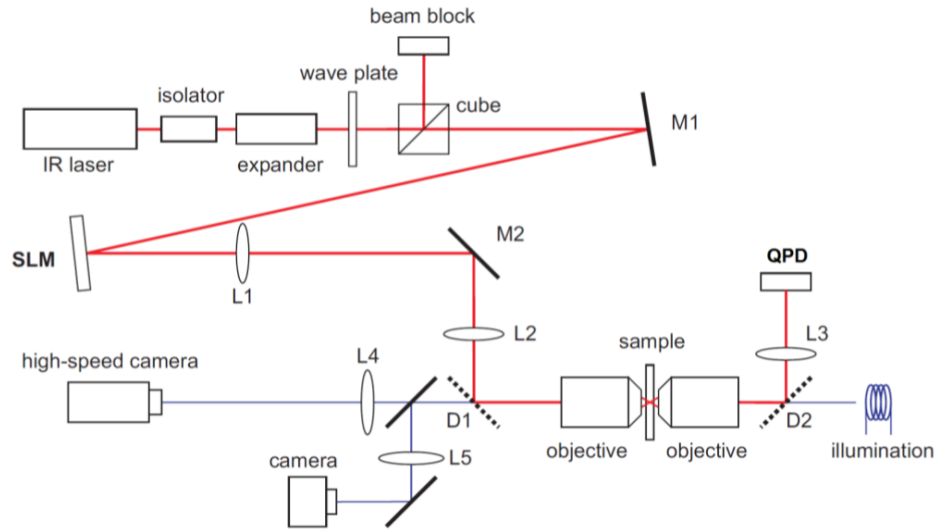


Figure 3.2: Schematic of our optical tweezers instrument, adapted from [16]. M1 and M2 are mirrors; L1-L5 are lenses; and D1 and D2 are dichroic mirrors.

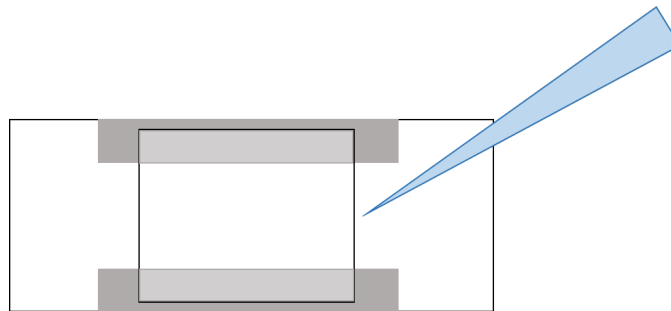


Figure 3.3: Diagram of a sample chamber consisting of two coverslips held together by two strips of Parafilm or Nescofilm (grey). The chamber is filled with sample using a micropipette (blue).

which is subsequently sealed using candle wax and nail polish. The chamber is placed on a manually-adjustable three-axis stage, giving the ability to move the trapping location within the chamber in all three dimensions.

A quadrant photodiode (QPD; QP154-Q-HVSD, Pacific Silicon Sensor) collects the laser light deflected by the trapped particle and is able to determine the relative position of the particle via its four photodiodes, as shown in Figure 3.4. The device can measure the position of the laser in the horizontal direction by taking the difference between the total voltages of the left two photodiodes and those of the right two photodiodes. Similarly, for the vertical direction, it computes the difference between the total voltages of the top and bottom photodiodes. Both these differences are normalized by the total sum of voltage across all of the photodiodes, as shown by the equations in Figure 3.4.

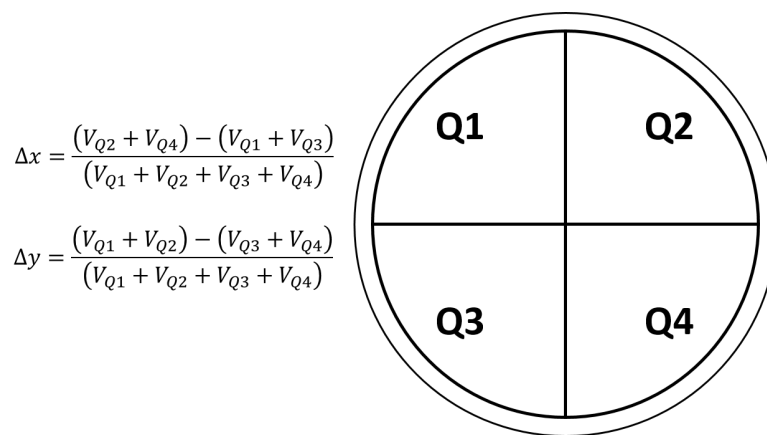


Figure 3.4: A schematic of a quadrant photodiode (QPD) with photodiodes labelled Q1, Q2, Q3 and Q4, and the calculations for the horizontal and vertical displacements where V is the voltage on a given photodiode.

A high-speed camera (PCO, 1200 hs,  $1280 \times 1024$  pixels) images the beads at bandwidths on the order of 1 kHz. The images were calibrated using a stage micrometer in place of the sample chamber to convert pixels to  $\mu\text{m}$ . Here,  $1 \text{ px} = 51.9 \pm 0.2 \text{ nm}$ . The relatively high bandwidth not only enables the use of images to calibrate the QPD signal (volts) to displacement units ( $\mu\text{m}$ ) but allows its use as a method of collecting position measurements for the microrheology experiments, as will be described in Section 3.3.

The optical tweezers instrument can also create multiple traps via a spatial light modulator (SLM) [16]. For the purposes of single-trap optical tweezers, the SLM acts as a mirror and reflects the incident laser light. However, it provides the opportunity to create multiple traps by modulating the laser's wavefront for the holographic optical tweezers for future applications.

### 3.3 Microrheology measurements and analysis

As explained in Chapter 2, a particle trapped in an optical trap undergoes local motion through thermal fluctuations. These fluctuations can be used to obtain the viscoelastic properties of the medium in which the particle is embedded. This section describes the two methods available in our experiment to measure the particle's positions: the QPD and the high-speed camera.

#### 3.3.1 QPD microrheology analysis

As previously explained, the QPD uses the deflection of the laser beam to determine the particle's position. Despite the QPD's high bandwidth with typical sampling frequency  $f_s = 100$  kHz, its sampled signal experiences aliasing. Aliasing refers to high-frequency signal components that become indistinguishable from lower frequencies. These high frequencies occur beyond the Nyquist frequency, which is defined as half the sampling frequency ( $f_{\text{Nyq}} = 1/2 \times f_s$ ) and their amplitudes add to the lower frequency amplitudes [42]. Therefore the power spectrum associated with a trapped bead in water can no longer be defined as a simple Lorentzian, as in Equation 2.15, but must also include the aliased frequencies, *i.e.*, [17]

$$PSD(f) = \sum_{n=-\infty}^{\infty} \frac{D}{\pi^2((2nf_{\text{Nyq}} - f)^2 + f_c^2)}. \quad (3.3)$$

For bead positions sampled at  $N$  discrete times, with  $\Delta t = 1/f_s$  results in an explicit form of the aliased power spectrum [75],

$$PSD(f) = \frac{D(1 - c^2)\Delta t}{2\pi f_c(1 + c^2 - 2c \cos(2\pi f/N))}, \quad (3.4)$$

where  $c = \exp(-2\pi f_c \Delta t)$ .

In reality, the relevant corner frequencies in our experiments are much lower than the Nyquist frequency of the QPD and aliasing only significantly alters the highest frequencies in the power spectrum. Therefore, when fitting the experimental QPD power spectrum, one can use the Lorentzian form in Equation 2.15 as long as the highest frequency powers are omitted.

As with every device, there is an error associated with the position tracking of the QPD. This error is on the order of  $10^{-11}$   $\mu\text{m}^2/\text{Hz}$ , which is very small compared to the plateau of the power spectrum (typically,  $10^{-6} - 10^{-5}$   $\mu\text{m}^2/\text{Hz}$ ) and therefore only only significantly affects high frequency values. Fitting to lower frequencies to avoid aliasing will also minimize any contributions from position-tracking error.

In experiments, the QPD collects position data at  $f_s = 100$  kHz for 100 seconds. The data is Fourier transformed separately in 1 second portions ( $T_{\text{msr}} = 1$  s) and the PSD is

averaged over the 100 sets to reduce uncertainty. The room temperature for all experiments was maintained at approximately 295 K.

The position measurements from the QPD have units of volts so a conversion factor into spatial units must be applied. This factor is determined for each bead separately since it depends on the radius and refractive index of the bead. Although we can assume that the indices of refraction of the particles are identical, there is always some variance in bead size.

With the high-speed camera, a correlation between position measurements from images from the camera and the QPD voltages can be extracted. Because the fluctuations of a trapped bead are very small (on the order of tens of nm), a good correlation signal requires forced, larger amplitude movements (on the order of hundreds of nm). Larger displacements are achieved, in both  $x$ - and  $y$ -directions, by manually moving the chamber back and forth using the micrometer screws on the stage. Smooth, quick motions create hydrodynamic drag forces that displace the bead while allowing it to stay trapped. The position measurements during these calibration trials are taken simultaneously by the QPD, at  $f_s = 10$  kHz, and the high-speed camera, at  $f_s = 500$  Hz. The images are analysed using a LabVIEW program written by Astrid van der Horst [16], which will be described in detail in Section 3.3.2.

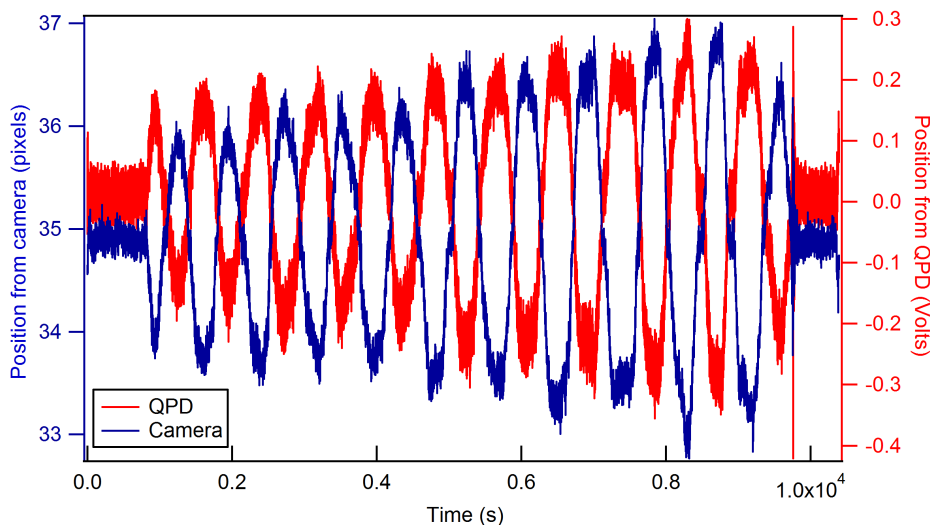


Figure 3.5: Positions of a trapped bead measured by the camera (blue) and the QPD (red) for forced, large-amplitude displacements for calibration. There is a negative correlation.

Before each manual shift of the chamber, the illumination and laser light were simultaneously blocked to synchronize the camera and QPD data. Figure 3.5 shows the position versus time of the large-amplitude displacements of a trapped bead as recorded by the camera and the QPD, for the select data between blockings. Figure 3.6 shows strong linear correlation of those position measurements, the slope of which gives the calibration factor. In the case of Figure 3.6, 1 volt = 11.7 px, and since 1 px = 51.9 nm, 1 volt = 0.608  $\mu\text{m}$ .

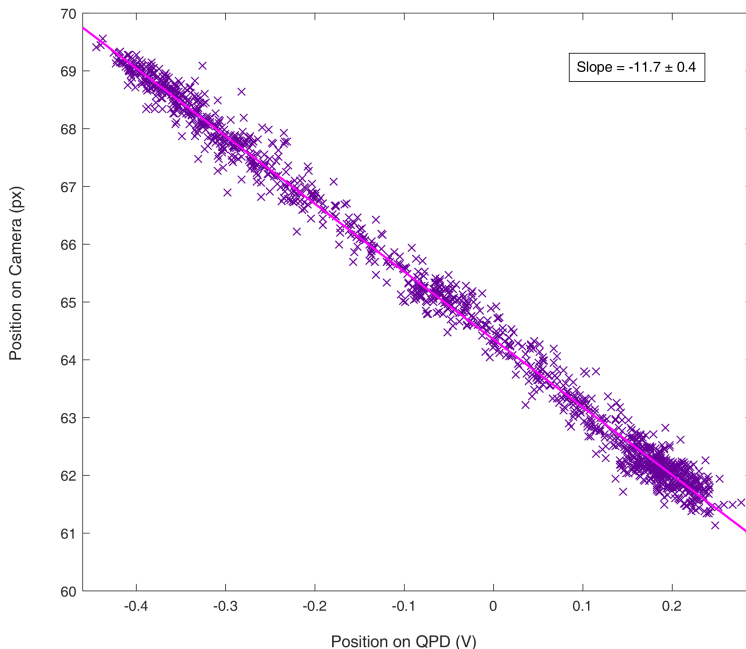


Figure 3.6: Positions as recorded by the camera versus those recorded by the QPD from Figure 3.5, plotted to extract a conversion factor. Here, 1 volt =  $-11.7 \pm 0.4$  px, and since 1 px =  $51.9 \pm 0.2$  nm, 1 volt =  $-0.61 \pm 0.02$   $\mu\text{m}$ .

Since the laser light is recombined through a back objective after forming the trap, in the case of multiple traps for the holographic optical tweezers, the deflections of the beam from each individual trap cannot be isolated. Therefore, the QPD is not the ideal device for analysing the displacements of multiple trapped particles simultaneously. Fortunately, the high-speed camera is already in place to image the beads at high frame rates and it is through this device that the displacements of multiple beads can be measured concurrently.

### 3.3.2 High-speed camera microrheology analysis

Though the high-speed camera images ( $160 \times 179$  px) the beads at  $f_s = 500$  frames per second (fps) for the QPD volts to  $\mu\text{m}$  calibration, it is capable of achieving frame rates up to 2500 fps and can be used to image the thermal fluctuations of the bead directly. As with the QPD, the power spectrum of a bead in water as collected by the camera must also include aliasing. As well, the camera has a limited shutter speed which translates to a time over which the image is blurred or averaged [76], referred to here as the integration time,  $W$ . The blurring effect must also be included and therefore, the expected power spectrum from the camera

is [17]

$$PSD(f) = \sum_{n=-\infty}^{\infty} \frac{D}{\pi^2((2nf_{Nyq} - f)^2 + f_c^2)} \frac{\sin(W\pi |2nf_{Nyq} - f|)}{W\pi |2nf_{Nyq} - f|} \Big)^2 + \frac{\sigma^2}{f_{Nyq}}. \quad (3.5)$$

The final term in Equation 3.5 is the error in position detection for the camera introduced as a result of the error in position tracking. This error was calculated by taking the power spectrum of a stuck bead with no expected variance. As shown in Figure 3.7, the  $x$ -position PSD for a stuck bead is relatively constant at all frequencies. The detection error is calculated as the area under the PSD (variance) divided by the Nyquist frequency,  $\frac{\sigma^2}{f_{Nyq}} = 6.5 \times 10^{-9} \mu\text{m}^2/\text{Hz}$ , equivalent to  $\sigma^2 = 8.1 \times 10^{-6} \mu\text{m}$ .

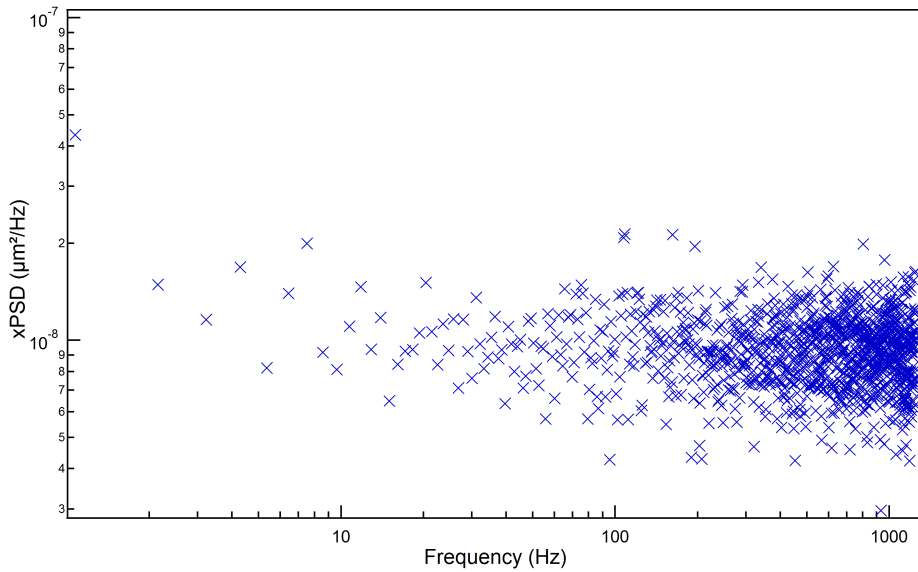


Figure 3.7: Power spectral density of the  $x$ -position of a stuck bead as collected by the camera, which is used to obtain the position detection error.

The limited 2500 fps frame rate, as compared to the QPD's 100 kHz, means that the Nyquist frequency for the camera's PSD is much lower and there is less high frequency data collected. As a result, the effects of aliasing, blur, and detection error are much more important to include in analysis since these are apparent much closer to the corner frequency.

For position-tracking experiments, the integration time on the high speed camera is set to  $W = 3.96 \times 10^{-4}$  s, which the camera's on-board software translates to a frame rate of approximately 2500 frames per second (fps). Images are taken for approximately 10 seconds and the PSD is calculated for 1 second portions ( $T_{msr} = 1$  s) of this time.

### Image detection software

The LabVIEW program used to analyse the images from the camera, for the purposes of both calibration and thermal fluctuation imaging, was originally written by Astrid van der Horst [16]. The program uses the first image in a sequence as a template then compares it to all subsequent images. The template is moved pixel by pixel across each image to generate a convolution of the spatial intensities. A two-dimensional parabolic surface is fit to the matrix of the convolution values for each frame, and the position of the bead is given by the maximum of this surface fit. For  $2\ \mu\text{m}$  polystyrene particles, this method has been shown to give a position accuracy of 0.02 px, or 1 nm [16].

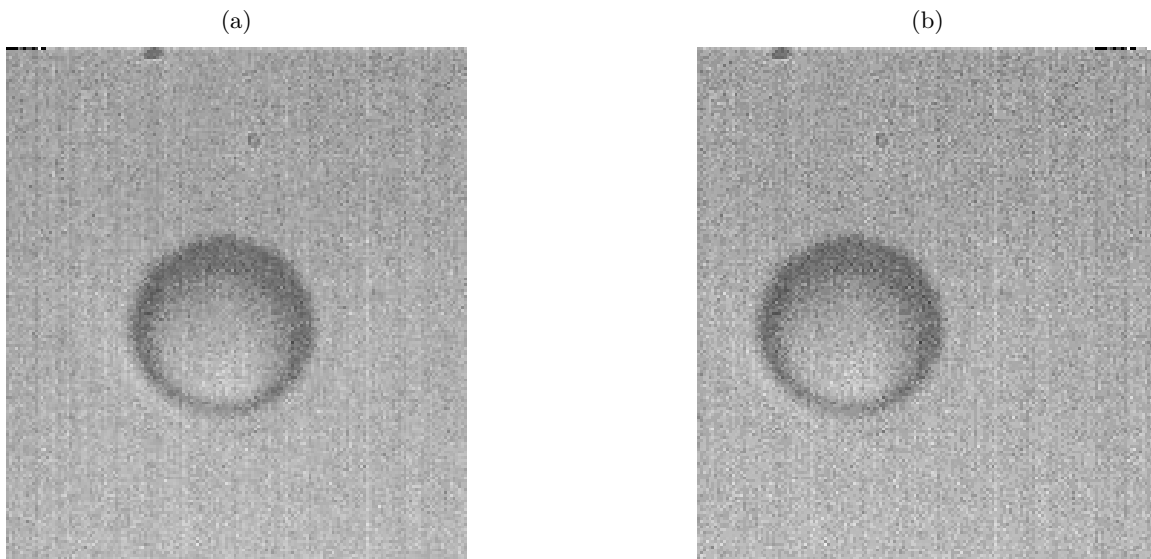


Figure 3.8: (a) First and (b) last bead in the image sequence resulting from shifted columns of pixels. The bead in (b) has been displaced a total of 22 px.

To convince myself of this resolution, I generated a stack of bead images in which the bead's position was computationally shifted in increments of 2 px. This was accomplished by transferring columns of pixels from the left to right edge of the image. Figure 3.8 shows the first and last images in the sequence. The results of running this sequence through the convolution program are presented in Figure 3.9. The program is able to accurately determine the 2 px motions in the  $x$ -direction up to 0.004 px or 0.2 nm, while the  $y$ -positions remain constant, though with less accuracy and an error of 0.015 px or 0.8 nm for this  $2.89\ \mu\text{m}$  bead with the current illumination. The error in  $y$ -positions is greater due to the inaccuracy in the first measurement of its position. For the stuck bead in Figure 3.7, the total detection error yields a position error of 2.8 nm, which is larger than the error from the analysis program due to other sources of error which affect detection, for example variation in illumination from image to image.

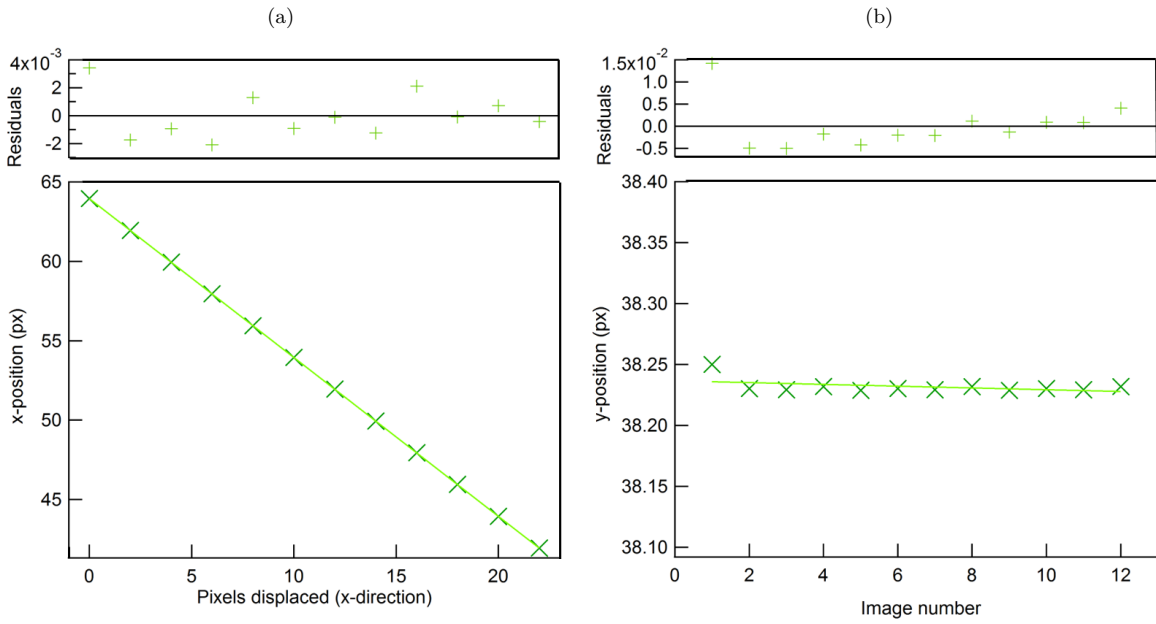


Figure 3.9: The positions in the (a)  $x$ - and (b)  $y$ -directions as detected by the analysis program for a bead moving 22 px in the  $x$ -direction over 12 images, with linear fits and residuals.

As a further test for potential bias in the  $x$  vs  $y$  directions, the images from one trial were rotated  $90^\circ$ . Figure 3.10 compares the original power spectrum to the rotated power spectrum. The two power spectra are nearly identical, therefore, the analysis program works equally for displacements in both  $x$ - and  $y$ -directions.

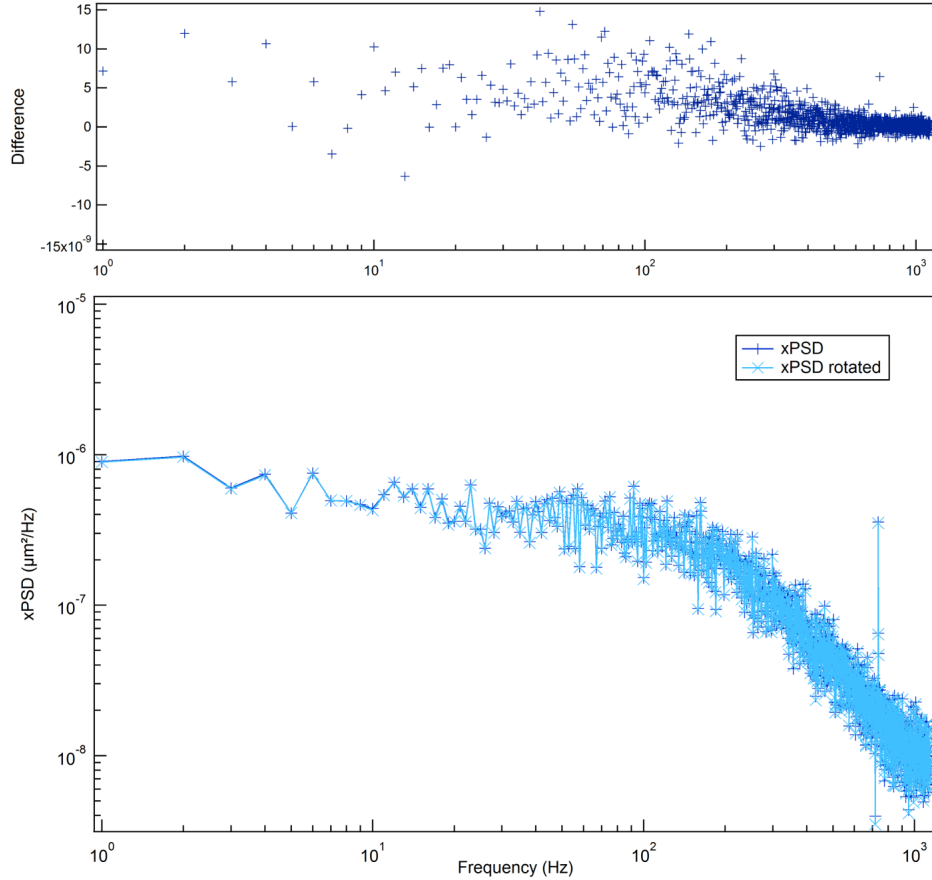


Figure 3.10: The power spectrum from a bead (blue) compared to the power spectrum for the same images but rotated  $90^\circ$  (light blue). The difference between the two power spectra (plotted above) is very small.

### 3.4 Effects of limited detection bandwidth on the viscoelastic moduli

When calculating the complex shear modulus from experimental data, the integration from the Kramers-Kronig relation (Equation 2.19) is cut off due to the limited bandwidth of detection devices. This causes a distortion at high frequencies for both the elastic and viscous modulus [45]. Figure 3.11 shows the complex shear modulus of a bead in water as measured by the QPD. It is distorted at frequencies higher than 100 Hz for  $G'(f)$  and 10 000 Hz for  $G''(f)$ , relating to the integration cut off.

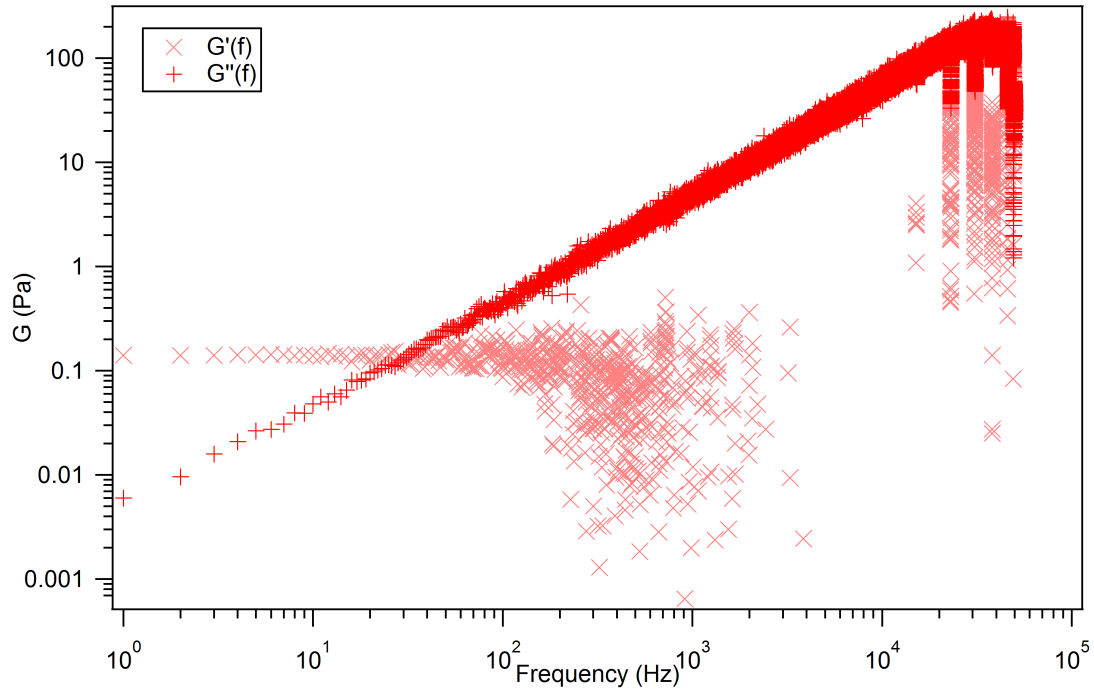


Figure 3.11: The viscous modulus (red) and the elastic modulus (pink) from data for a bead trapped in water, as measured by the QPD. The distortion at high frequencies is due to the limited bandwidth of the device.

For a bead in water, the distortion is obvious because certain trends are expected (see Section 2.5). However, for a complex fluid with unknown viscous and elastic properties, it is important to differentiate between real and distorted results. The high-speed camera has a lower Nyquist frequency than the QPD. So for data from this device, the distortion will appear at lower frequencies than in Figure 3.11. In Chapter 5, I numerically investigate where this distortion appears for both camera-like and QPD-like data.

## Chapter 4

# Optical tweezers-based experiments of a bead in water using a high-speed camera

As mentioned in Chapter 3, the use of holographic optical tweezers for multiple-particle experiments relies on the high-speed camera, instead of the QPD, for position tracking of the trapped beads. While the camera has proven useful for the calibration of the QPD instrument, it has not yet been implemented as the main source of data collection in our optical tweezers set-up. Therefore, the first step in implementing the holographic optical tweezers involves ensuring that data from the camera can produce the expected diffusion constant and corner frequency of a single bead trapped in water. In this chapter, I compare the power spectra inferred from both the QPD and the high-speed camera and find a discrepancy between the diffusion constants measured from each device, which I attempt to resolve.

### 4.1 Experimental power spectra

Figure 4.1 shows the power spectra from both the camera and QPD, for a single  $2.89 \mu\text{m}$  diameter polystyrene bead trapped in water. The curves show fits of Equations 3.3 and 3.5 to the QPD and camera data, respectively. The Nyquist frequency, as dictated by a sampling frequency for these measurements of 25008 fps, limits the camera power spectrum to only about 1250 Hz. There is a distinct flattening at the highest frequencies explained by the aliasing, blur, and noise, as discussed in Chapter 3, which has been taken into account in the superimposed fitting equation given by Equation 3.5 with a sum from  $n = -2$  to 2. At the highest frequencies, this flattening is also apparent for the QPD's power spectrum ( $f_{\text{Nyq}} = 50 \text{ kHz}$ ); however, the fit (Equation 2.15) avoids these frequencies. All data shown

in this thesis are for position data in the  $x$ -direction, however, this technique has been validated for both  $x$ - and  $y$ -directions.

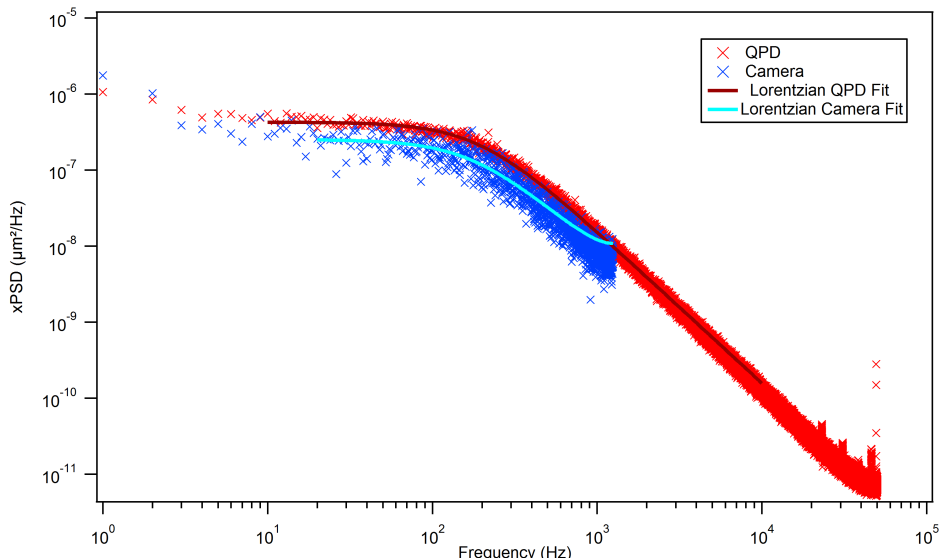


Figure 4.1: The power spectra as measured by the QPD (red) and the high-speed camera (blue), with appropriate Lorentzian function fits (Equations 2.15 for QPD and 3.5 for camera) for a  $2.89 \mu\text{m}$  diameter polystyrene bead in water. Fits were calculated from  $f = 10 \text{ Hz}$  up to  $f = 10\,000 \text{ Hz}$  for the QPD, and from  $f = 15 \text{ Hz}$  to  $f = 1249 \text{ Hz}$  for the camera. Their parameters were  $D = 0.1533 \pm 0.0005 \mu\text{m}^2 \cdot \text{Hz}$  and  $f_c = 189.6 \pm 0.4 \text{ Hz}$  for the QPD and  $D = 0.082 \pm 0.002 \mu\text{m}^2 \cdot \text{Hz}$  and  $f_c = 183 \pm 4 \text{ Hz}$  for the camera.

An immediately apparent difference between the camera’s PSD and QPD’s PSD is the height of the plateaus. The outputs of the fittings are the corner frequency and the diffusion constant. While the corner frequencies, in this and most cases, are in reasonable agreement,  $f_c = 189.6 \pm 0.4 \text{ Hz}$  from the QPD and  $f_c = 183 \pm 4 \text{ Hz}$  from the camera, the diffusion constants are not,  $D = 0.1533 \pm 0.0005 \mu\text{m}^2 \cdot \text{Hz}$  and  $D = 0.082 \pm 0.002 \mu\text{m}^2 \cdot \text{Hz}$ , respectively. The errors reported in the fitting parameters represent one standard deviation from the mean fit value, as calculated by the IGOR Pro software. The expected value for the diffusion constant of a  $2.89 \mu\text{m}$  diameter bead in water at  $T = 295 \text{ K}$  is  $D = 0.156 \mu\text{m}^2 \cdot \text{Hz}$ .

Since the set-up can never be completely isolated from external sources of noise, such as thermal drift in the objective alignment, the power spectrum at low frequencies often increases. This is particularly prevalent in camera power spectra because the measurements of the bead are taken in a lab-based reference frame, whereas the QPD is positioned to re-image the back focal plane and records deflections of the bead relative to the trap [77].

Because of the drift-related increases in power spectral density at low frequencies, it is therefore not always prudent or accurate to fit over the entire frequency range of data. For instance, in Figure 4.1, the fit for the camera is taken starting at  $f = 15 \text{ Hz}$  and includes the highest frequencies available (i.e. up to  $f = 1249 \text{ Hz}$ ). The QPD fit in this case starts

at  $f = 10$  Hz. All QPD fittings extend to  $f = 10\,000$  Hz, to avoid aliasing and detection error as mentioned before.

The fact that the diffusion constants from the QPD and camera do not match is problematic. As will be shown, it is a trend that I see in almost all of my trials, and forms the basis of the bulk of the experimental work I have performed. The acquisition of the position data of the bead is typically taken simultaneously for both QPD and camera, and therefore the diffusion constants should be identical. The expected radius based on the manufacturer’s specifications is  $1.45 \pm 0.10 \mu\text{m}$ . Using the diffusion constant from the fit and the Stokes-Einstein equation (Equation 2.13) with  $T = 295$  K and expected viscosity,  $\eta = 9.58 \times 10^{-4}$  Pa·s, the QPD average bead radius, for 21 independent trials, falls into that range at  $1.35 \mu\text{m}$  with standard deviation  $0.17 \mu\text{m}$ . The camera, for the same trials, reports well outside that range at  $2.6 \pm 0.3 \mu\text{m}$ . Therefore, the QPD agrees with the Stokes-Einstein prediction but the camera does not.

#### 4.1.1 Position-sensitive diode-derived power spectra

As a verification of the QPD’s results, I replaced the QPD with a position sensitive detector (PSD\*, the asterisk will distinguish this acronym from the power spectral density). The PSD\* (UDT Sensors, DL-10) operates in a similar manner to the QPD, using the laser deflection to track the bead’s location. It identifies the location of the laser spot via photocurrents generated by the change in resistance on a PIN diode. The current is collected by four electrodes which bound the sides of the PIN diode square. The  $x$ - and  $y$ -positions can be computed based on the current at each of the electrodes in a similar fashion to that of the QPD [78].

Figure 4.2 shows the bead position as function of time. The position sensitive detector, again, sees more variance in the bead’s motion ( $\langle x^2 \rangle = 1.37 \times 10^{-4} \mu\text{m}^2$ ) than the camera ( $\langle x^2 \rangle = 7.56 \times 10^{-5} \mu\text{m}^2$ ). Indeed, the power spectra, in Figure 4.3, still lead to a difference in diffusion constants, with the PSD\* reporting  $D = 0.1425 \pm 0.0005 \mu\text{m}^2 \cdot \text{Hz}$  and the camera reporting  $D = 0.075 \pm 0.002 \mu\text{m}^2 \cdot \text{Hz}$ . Therefore, the issue causing these differences is likely with the high-speed camera and not with the QPD.

#### 4.1.2 Surface effects

Another test of the PSD involves the bead’s potential interactions with the coverslip slides. The well-known ‘wall effect’ [79] that nearby surfaces have on a bead will increase its lateral drag coefficient by [80]

$$\gamma_{\text{effective}} = \frac{\gamma}{\left(1 - \frac{9R}{16h} + \frac{R^3}{8h^3} - \frac{45R^4}{256h^4} - \frac{R^5}{16h^5}\right)}. \quad (4.1)$$

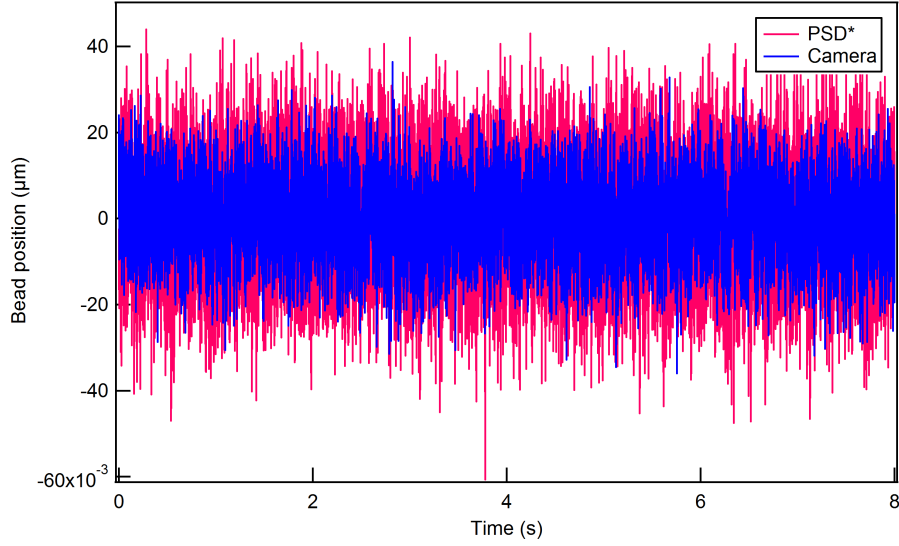


Figure 4.2: Position of the bead as detected by the position sensitive diode (pink) and the high-speed camera (blue). Time series are not coincident. The variances measured are  $\langle x^2 \rangle = 1.373 \times 10^{-4} \mu\text{m}^2$  for the PSD\* and  $\langle x^2 \rangle = 7.56 \times 10^{-5} \mu\text{m}^2$  for the camera.

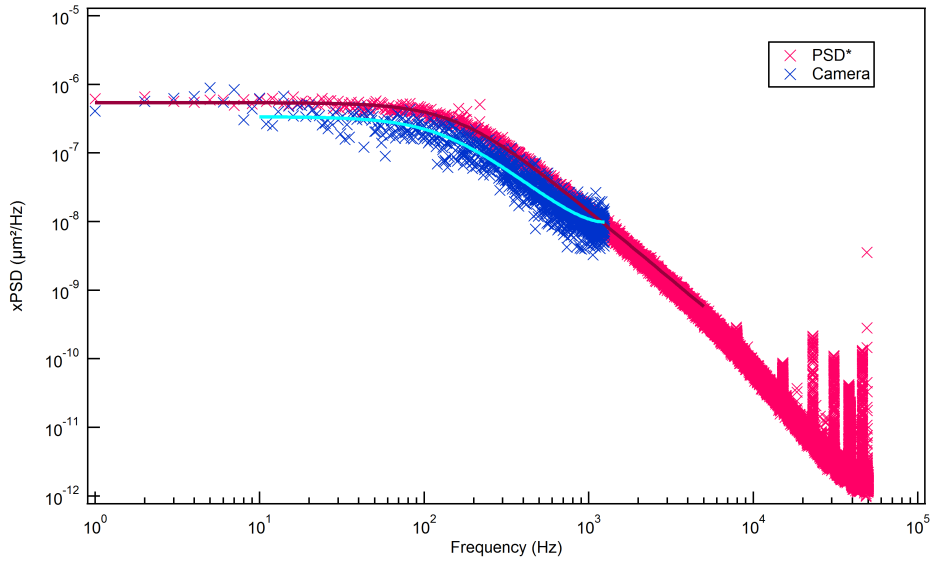


Figure 4.3: The power spectra as measured by the PSD\* (pink) and the high-speed camera (blue). Fitting parameters were  $D = 0.1425 \pm 0.0008 \mu\text{m}^2 \cdot \text{Hz}$  and  $f_c = 163.5 \pm 0.5 \text{ Hz}$  for the QPD and  $D = 0.075 \pm 0.002 \mu\text{m}^2 \cdot \text{Hz}$  and  $f_c = 168 \pm 4 \text{ Hz}$  for the camera.

$R$  represents the radius of the bead and  $h$  is the distance from the centre of the bead to the surface. I measured the thickness of the sample chamber to be approximately  $120\ \mu\text{m}$  and therefore the bead can be no further than  $60\ \mu\text{m}$  from a surface. The typical trapping location in my experiments is approximately midway through the chamber, at which position the drag constant is expected to be only about 1% larger than its bulk value. Even  $30\ \mu\text{m}$  from a surface, the increase should be only 2%.

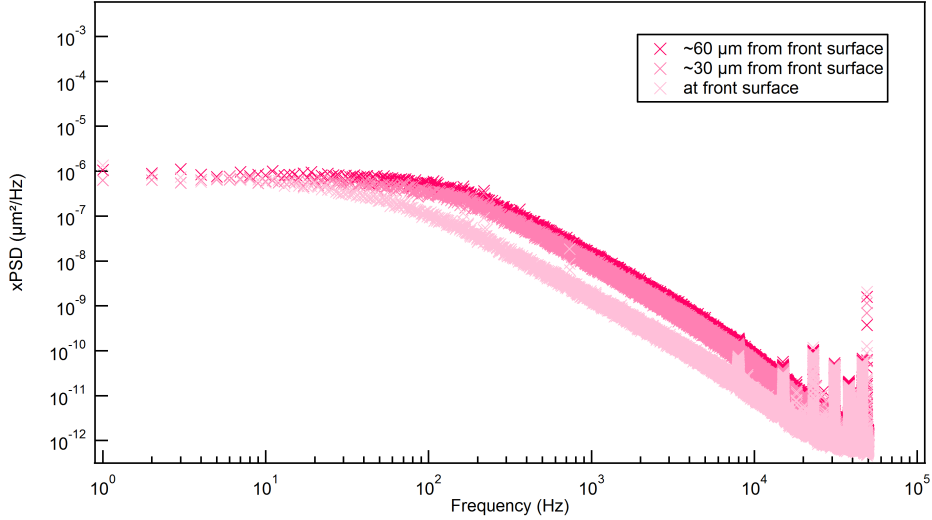


Figure 4.4: Power spectra from the PSD\* at several trap locations at different distances from a surface.

To test this, Figure 4.4 shows power spectra from the PSD\* for the same bead at different locations within the chamber. During experiments, it is easy to identify the front and back surfaces because they reflect more light, however all trapping locations are approximate. The output diffusion constant from the  $30\ \mu\text{m}$  location is lower by as much as 15% from the typical trapping location. However, since the surface effects should appear for both the camera and the PSD\*, and similar results occur for the camera data (data not shown), this does not add any information to resolve the discrepancy between the two measurements. However, it does highlight the importance of the trap placement as far from surfaces as possible.

The next several sections investigate the disagreement between diffusion constants as calculated by the camera and by the QPD through asking questions about how laser power affects the difference, how different fitting methods can effect the results, and about the underlying cause of the discrepancy: a difference in the variance of the bead's movement. As well, different camera frame rates are investigated.

## 4.2 Effects of laser power on power spectra

First, I looked at the effects of changing the laser power. The amount of laser power directed through the objective relates proportionally to the trap stiffness,  $\kappa$ . By Equation 2.17, an increase in trap stiffness leads to an increase in corner frequency. In the example of Figure 4.1, the corner frequency from the QPD agreed with that from the camera. Figure 4.5 shows the corner frequencies from both the QPD and the camera for multiple trials as a function of laser power. Laser power was measured directly before the first objective lens (Figure 3.2). The measured corner frequencies do scale linearly, as expected, with laser power. In general, the corner frequencies agree fairly well between the two devices, with an exception at high powers. The discrepancy at these high powers is likely explained by the limited data beyond the corner frequency for the camera. The more data available to fit the  $-2$  slope after the corner, expected from the power spectrum of a Newtonian fluid such as water, the more accurate the fitting parameters. Since the camera's frame rate limits the power spectrum to  $f_{Nyq} = 1250$  Hz and the tail end of this data is strongly influenced by aliasing and blur, with a high corner frequency, there is little  $-2$  slope to fit. Nonetheless, the corner frequencies still lie within 15% of each other.

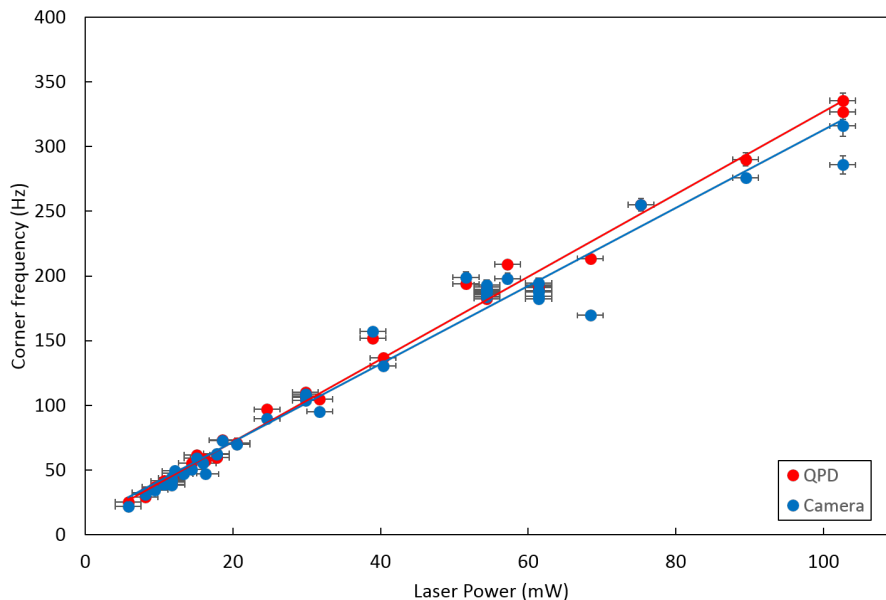


Figure 4.5: Corner frequency of QPD (red) and camera (blue) power spectra as a function of laser power. The linear fits are slightly different due to underestimating the corner frequency in the limited frame rate camera data at high laser powers.

The diffusion constant should be independent of laser power. The expected diffusion constant from the Stokes-Einstein relation (Equation 2.13) for this size bead is  $D = 0.156 \mu\text{m}^2 \cdot \text{Hz}$ , and though there may potentially be some local heating due to the increase

in laser power, it has been shown to be inconsequential for the powers and wavelength used here [81]. For all the diffusion constants, the QPD value is always higher than the camera value regardless of laser power, as shown in Figure 4.6. There is a large scatter in both QPD and camera diffusion constants, not accounted by a variation in bead size. The cause of this large scatter, particularly in the QPD, has not been investigated.

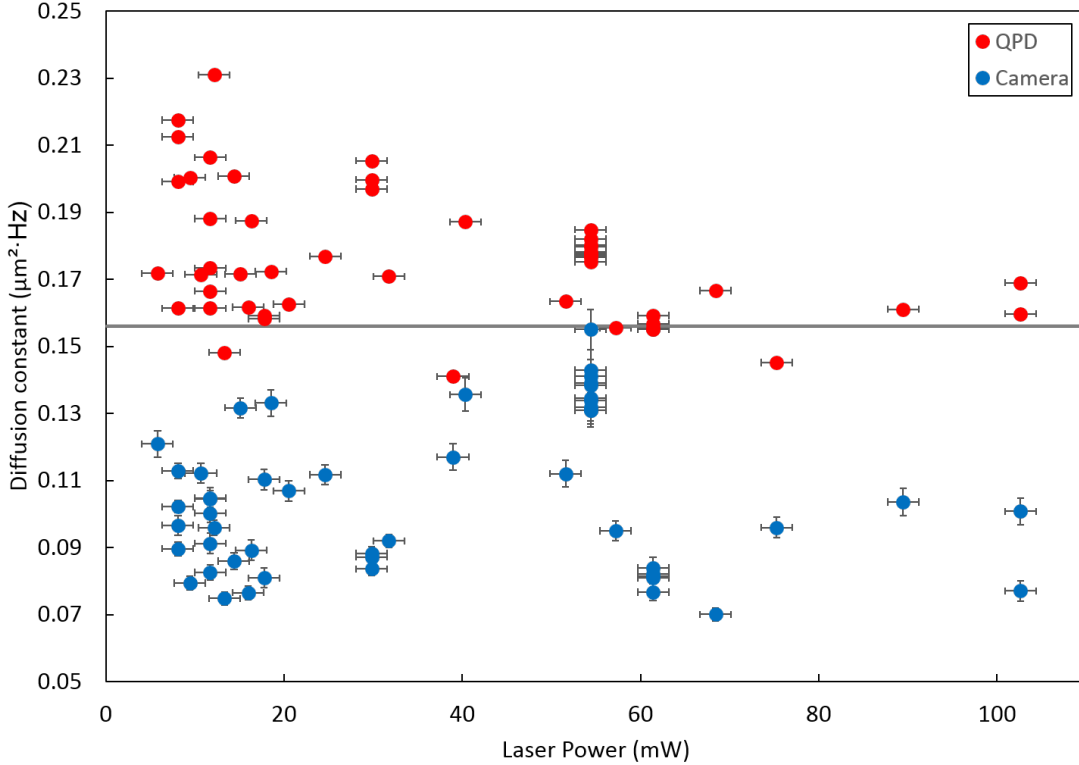


Figure 4.6: Diffusion constant obtained from QPD (red) and camera (blue) power spectra as a function of laser power. The black line indicates the expected diffusion constant for a  $2.89 \mu\text{m}$  bead in water at  $T = 295 \text{ K}$  using the Stokes-Einstein relation (Equation 2.13). No trend is observed with laser power and most diffusion constants from the camera are significantly lower than those from the QPD.

The amount of laser light directed through the objective might also affect the image quality extracted by the camera, since the visible light also passes through the same objective. Figure 4.7 shows the same bead trapped at two different laser powers. They appear similar and we would not expect a change in the image analysis. Furthermore, the similarity in appearance implies that both beads are trapped at approximately the same depth within the chamber.

While the bead appears similar for both high and low laser powers, and the corner frequencies scale appropriately with changing laser power (except at high laser powers), the difference between the diffusion constants persists.

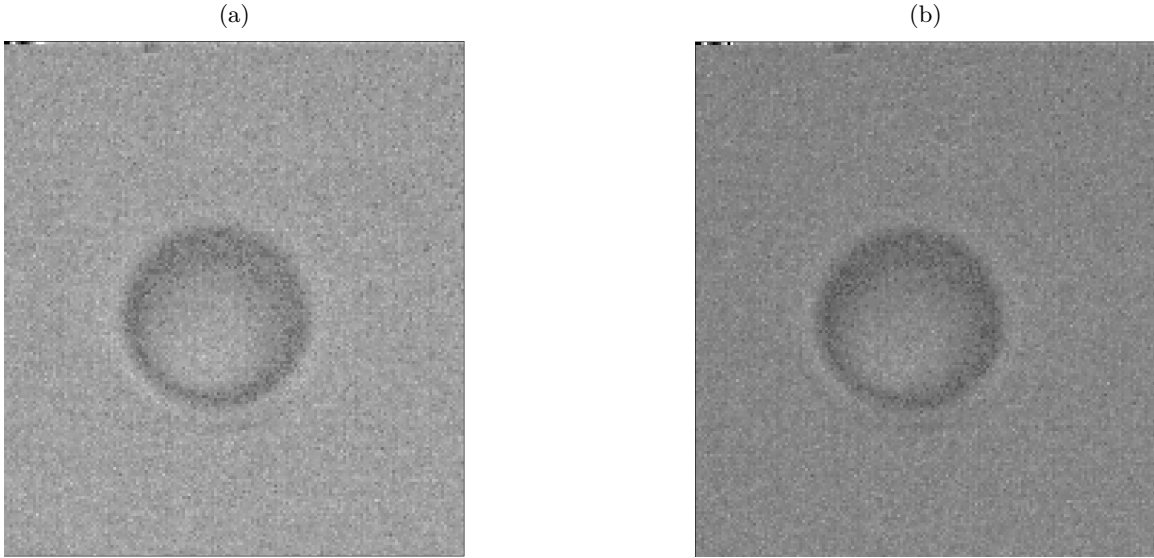


Figure 4.7: The same bead trapped in water by laser powers of (a) 17 mW and (b) 114 mW. The images appear very similar.

### 4.3 A different fitting method for the PSD

In this section, I investigate a different method of obtaining the diffusion constant which avoids the bias of choosing a correct fitting range when there is significant drift in the camera PSD. The power spectrum is multiplied by the square of the frequency to obtain a curve as in Figure 4.8, where the  $-2$  slope of the power spectrum now appears as a flat line. In other words, for  $f > f_c$ ,

$$PSD(f > f_c) \times f^2 = \frac{D}{\pi^2 f^2} \times f^2 = \frac{D}{\pi^2} \quad (4.2)$$

Therefore, the diffusion constant can be extracted as the intercept times  $\pi^2$  of a flat line fit (slope 0).

The example shown in Figure 4.8 yields a diffusion constant of  $D = 0.107 \pm 0.002 \mu\text{m}^2 \cdot \text{Hz}$ , whereas the diffusion constant calculated using the previous, original method was  $D = 0.097 \pm 0.003 \mu\text{m}^2 \cdot \text{Hz}$ . Since the QPD value in this instance was  $D = 0.1817 \pm 0.0007 \mu\text{m}^2 \cdot \text{Hz}$ , the non-biased fitting appears to improve the output value but not substantially. The corner frequencies agreed for both fits.

It is worth mentioning that this method could equally be used for fitting the QPD data, though because of the large quantity of high frequency data for this device, it makes little difference. In general, I found that although the  $PSD \times f^2$  fitting method does slightly improve the agreement between camera and QPD, it is not significant enough to explain the diffusion-constant discrepancy. Future studies may find this a more-reliable and less-biased

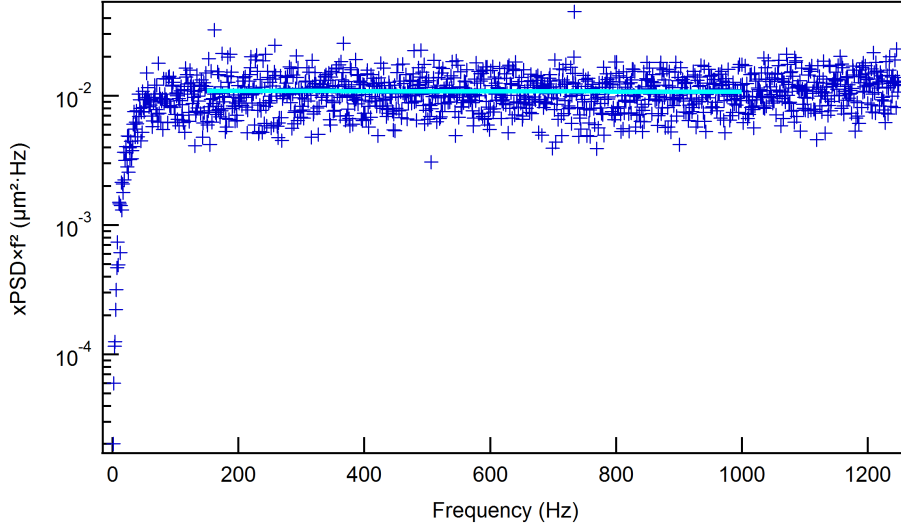


Figure 4.8: By multiplying the power spectrum by frequency squared, the intercept of the flat line fit to the tail gives the diffusion constant times  $\pi^2$ . Here,  $D = 0.1073 \pm 0.0011 \mu\text{m}^2 \cdot \text{Hz}$ .

method of fitting the power spectrum for the camera, but it is not implemented further in this work.

#### 4.4 Variance of a bead as measured by the QPD and high-speed camera

The fundamental issue underlying the discrepancy in diffusion constants is the difference between the observed variance from each device. The area under power spectral density should give the variance of the bead’s position. From the variance, the trap stiffness can be calculated using Equation 2.16 and, using the corner frequency from the fit, Equation 2.17 yields the drag coefficient,  $\gamma = 6\pi\eta R$ . The diffusion coefficient can be calculated using Equation 2.13. For any given trial, the diffusion constant calculated using the area under the curve for both QPD and camera agreed with the respective fitting results better than 5% (data not shown). However, the areas, as one might expect since the fit outputs do not agree, are not similar. The camera’s variance is less than that of the QPD.

Figure 4.9 shows the  $x$ -position versus time of a bead as measured by the QPD and high-speed camera. Most notably in Figure 4.9, according to the QPD, the bead explores more space than according to the camera, *i.e.*, the QPD curve is always visible behind the camera’s, and therefore the QPD reads a greater variance than the camera, consistent with previous results. The QPD variance is  $\langle x^2 \rangle = 1.50 \times 10^{-4} \mu\text{m}^2$  while the camera detects  $\langle x^2 \rangle = 1.14 \times 10^{-4} \mu\text{m}^2$ .

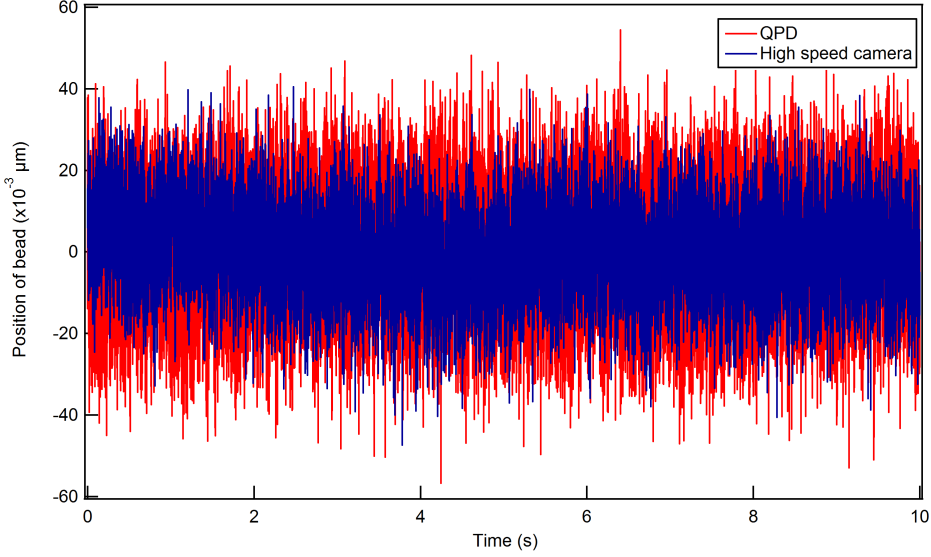


Figure 4.9: Position of a bead as a function of time as measured by the QPD (red) and camera (blue). Time series are not coincident. The variances measured are  $\langle x^2 \rangle = 1.498 \times 10^{-4} \mu\text{m}^2$  for the QPD and  $\langle x^2 \rangle = 1.136 \times 10^{-4} \mu\text{m}^2$  for the camera.

This revelation brought up an alarming query. Since the high-speed camera is also used as a method to calibrate the QPD voltage into position data, could the QPD-derived measurements be incorrect? Figure 4.10 shows bead position versus time for the calibration file used for this data. The forced, large amplitude movements of the bead match up quite well, so the calibration should be accurate. However, the difference in variances is noticeable even on this scale as the QPD position is always visible behind that of the camera.

Another way to visualize the difference in positions is through the histogram of the positions in Figure 4.9, shown in Figure 4.11. Both are well described by a Gaussian curve well, however the QPD has a larger standard deviation ( $0.01223 \pm 0.00002 \mu\text{m}$ ) than the camera ( $0.01065 \pm 0.00005 \mu\text{m}$ ).

A smaller bead variance obtained from the camera is expected due to the motion blur from the finite integration time,  $W$ . As derived by Wong and Halvorsen [76], the measured variance is expected to be

$$\langle x^2 \rangle_{meas} = \langle x^2 \rangle \left[ \frac{2}{\alpha} - \frac{2}{\alpha^2} (1 - e^{-\alpha}) \right], \quad (4.3)$$

where  $\alpha = WD\kappa/(k_B T) = 2\pi W f_c$ . For corner frequency and frame rate corresponding to data in Figure 4.9, the measured variance is expected to be reduced by 14.6% for the camera relative to the QPD. Therefore, the variance as measured by the camera should be  $\langle x^2 \rangle_{meas} = 1.45 \times 10^{-4} \times 0.854 = 1.28 \times 10^{-4} \mu\text{m}^2$ , however the actual variance from the camera in the experiment was  $\langle x^2 \rangle = 1.14 \times 10^{-4} \mu\text{m}^2$ . Unfortunately the measured variance from the camera is still less than the predicted variance due to the blur. This is not

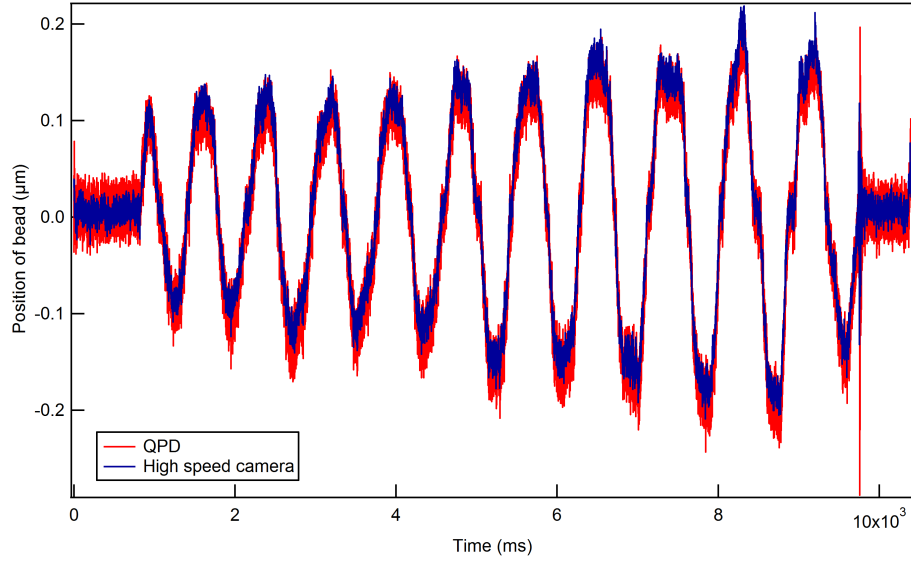


Figure 4.10: Position of a bead as a function of time as measured by the QPD (red) and camera (blue) during a calibration. The QPD's variance is clearly larger, however the forced large amplitudes of the calibration agree well.

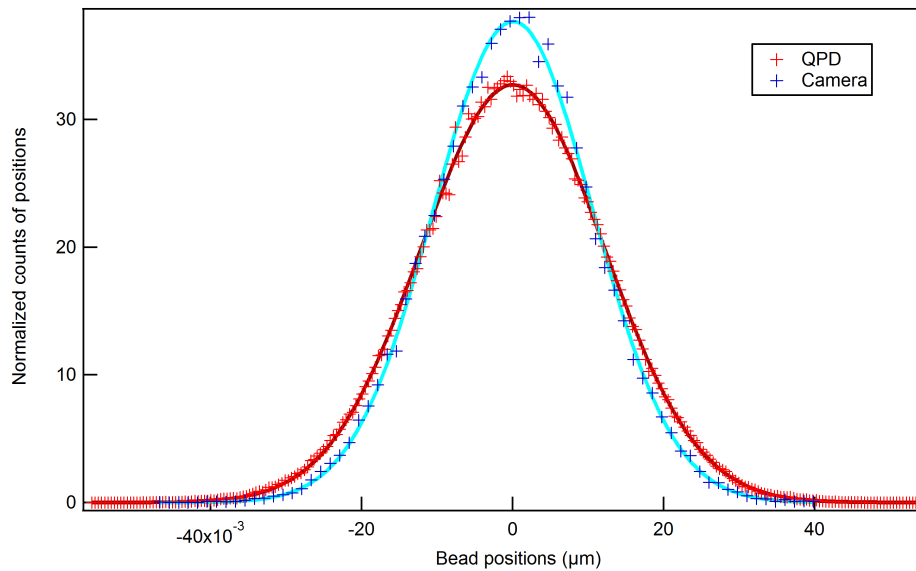


Figure 4.11: A normalized histogram (probability density function) of the position of a bead as detected by the QPD (red) and the camera (blue), corresponding to data shown in Figure 4.9. Both histograms are fit with a Gaussian curve; the QPD has standard deviation  $0.01223 \pm 0.00002 \mu\text{m}$  and the camera has standard deviation  $0.01065 \pm 0.00005 \mu\text{m}$ .

entirely surprising, since the equation used to fit the camera-derived power spectral density (Equation 3.5) includes this blur and still produces a discrepancy between the camera and QPD.

#### 4.4.1 Down-sampling of the QPD position data

In order to validate Equation 4.3, the QPD position data was computationally down-sampled to reflect changes in the sampling frequency and compare the variance obtained through down-sampling to the theoretical expectations. Blur was simulated by averaging appropriately sized portions of the position data. Figure 4.12 shows two examples of this down-sampling, resulting in effective sampling frequencies  $f_{s(\text{effective})} = 10\,000$  Hz and  $f_{s(\text{effective})} = 2\,000$  Hz, along with the original position versus time data from the QPD. The variance visually decreases as the data is down-sampled.

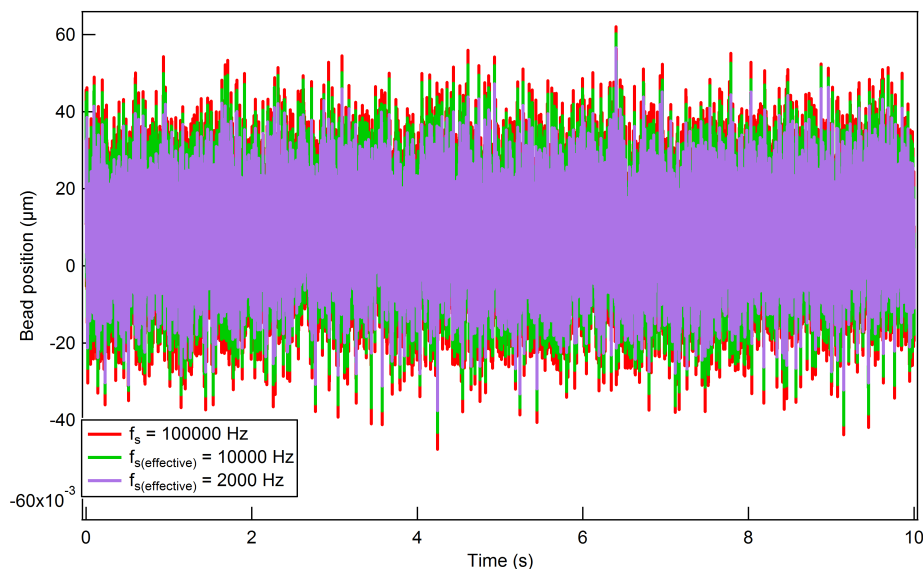


Figure 4.12: Down-sampled position of bead from the QPD. The original data ( $f_s = 100\,000$  Hz, red) gives a variance of  $\langle x^2 \rangle = 1.498 \times 10^{-4} \mu\text{m}^2$ , the down-sampled data to  $f_{s(\text{effective})} = 10\,000$  Hz (green) give a variance of  $\langle x^2 \rangle = 1.454 \times 10^{-4} \mu\text{m}^2$  and the down-sampled data to  $f_{s(\text{effective})} = 2\,000$  Hz gives a variance of  $\langle x^2 \rangle = 1.267 \times 10^{-4} \mu\text{m}^2$

Figure 4.13 shows the power spectra for eight different down-sampled trials all from the same experimental data, also shown. The tail ends of the PSDs get cut off earlier as the data gets down-sampled due to the changing effective sampling frequency (changing the Nyquist frequency), and the slight flattening due to aliasing and blur is also visible. However, the diffusion constant from fitting each of these down-sampled PSDs, including the expected effect of blur (Equation 3.5), does not change significantly and does not exhibit a trend with effective sampling frequency. The average diffusion constant was  $D = 0.172 \mu\text{m}^2 \cdot \text{Hz}$  with a standard deviation of just  $0.002 \mu\text{m}^2 \cdot \text{Hz}$ . By contrast, the camera power spectrum

for this trial yielded  $D = 0.132 \pm 0.004 \mu\text{m}^2\cdot\text{Hz}$ . It can be concluded that despite taking into account the blur by down-sampling the data, the QPD and camera still do not agree in the variance or power spectrum fittings.

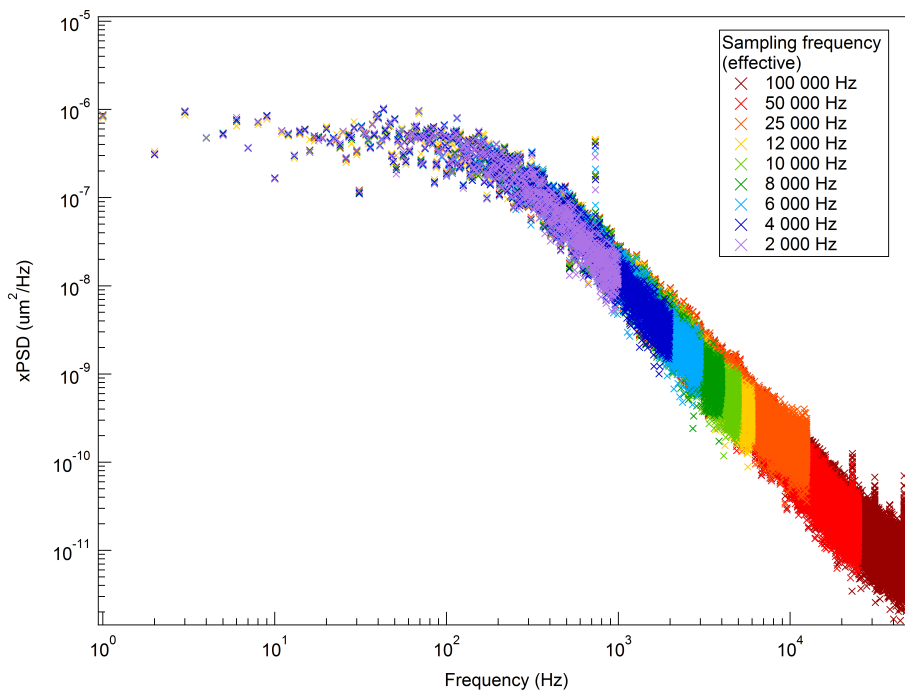


Figure 4.13: Power spectra for down-sampled PSD. The  $D$  values from fitting (not shown) averaged to  $D = 0.172 \mu\text{m}^2\cdot\text{Hz}$  with a standard deviation of  $0.002 \mu\text{m}^2\cdot\text{Hz}$  and the corner frequencies averaged to  $f_c = 181.0 \pm 1.6 \text{ Hz}$ .

To reiterate this conclusion, Figure 4.14 shows the expected variance as predicted by Equation 4.3 for a trial with  $f_c = 180 \text{ Hz}$  as a function of the integration time. Contrasted are the nine different down-sampled trials from Figure 4.13 along with the camera data at the usual  $W = 3.96 \times 10^{-4} \text{ s}$ . The down-sampled QPD data all agree with the predicted values, however the camera does not.

## 4.5 Varying the frame rate of the high-speed camera

Thus far the camera integration time has been exclusively set to  $W = 3.96 \times 10^{-4} \text{ s}$ , which, for our camera, corresponds to approximately  $f_s = 2500 \text{ fps}$ . In the last section, the bead's variance from the camera did not agree with the theoretically predicted value. However, by varying the camera integration time, could a similar but offset trend in the camera data be observed? Figure 4.15 shows the camera variance as a function of integration time, while maintaining a sampling frequency of approximately  $f_s = 2500 \text{ Hz}$ . From Equation 4.3, I expect a decrease in variance as the integration time is increased. However, Figure 4.15 shows an opposite trend: the measured variance increases with increased integration time.

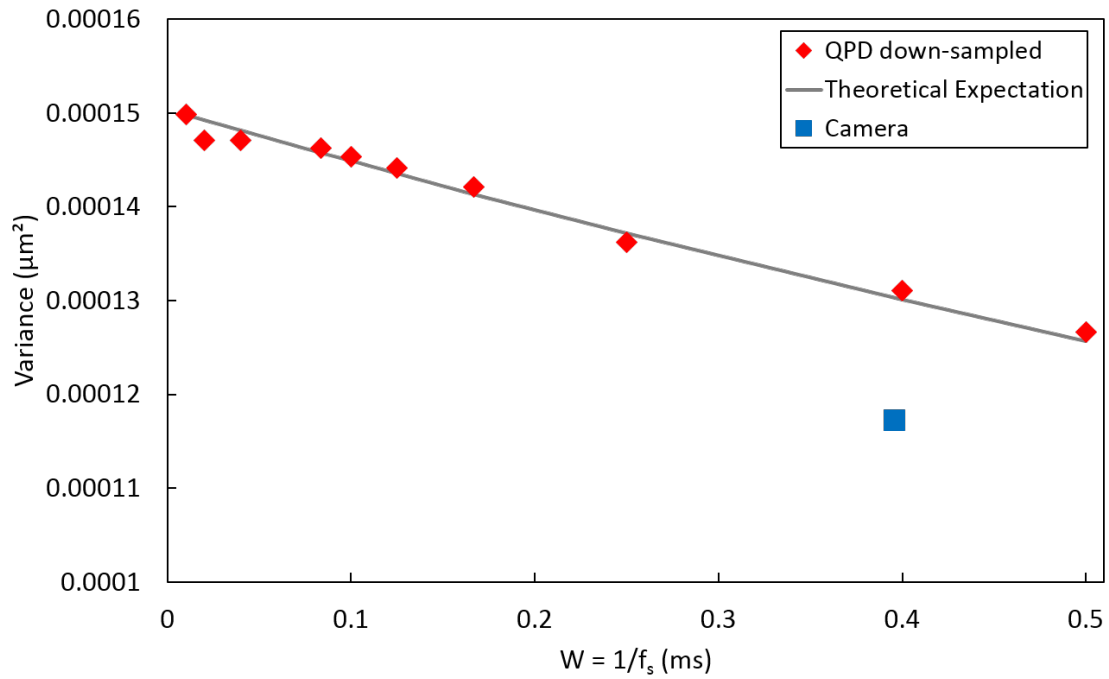


Figure 4.14: Variance as a function of the reciprocal of the effective sampling frequency from the down-sampled QPD data and the camera data at  $f_s = 2501.68$  fps in comparison with the theoretical expectation from Equation 4.3. Camera data do not agree with the theoretical expectation but down-sampled QPD do.

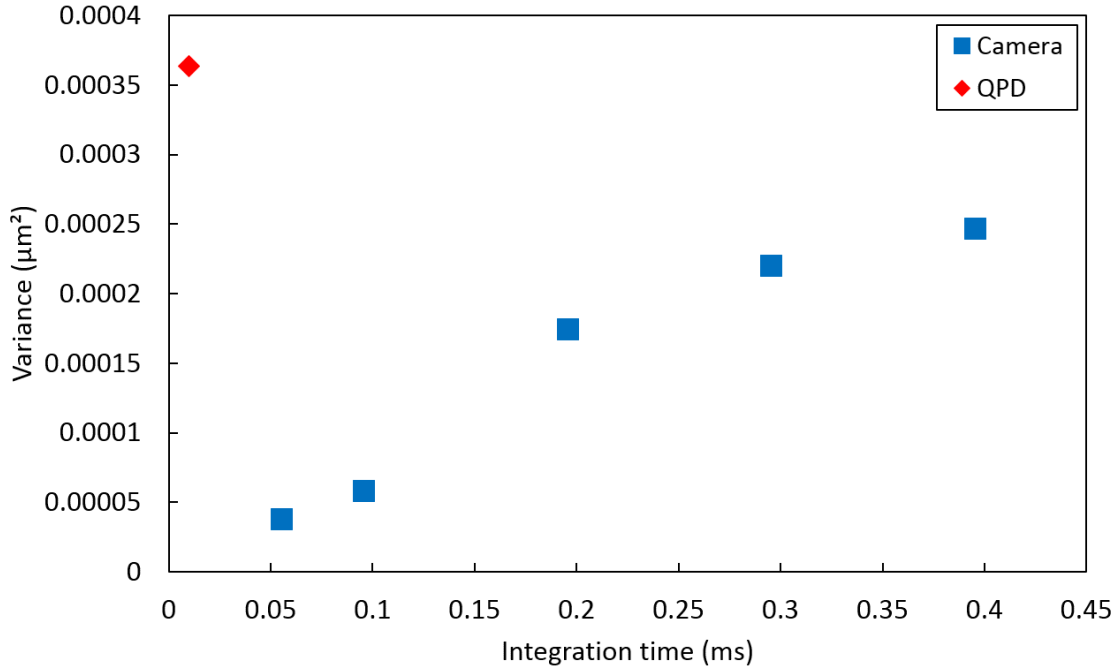


Figure 4.15: Variance as a function of integration time for the camera with  $f_s = 2500$  Hz (blue) for a bead trapped in water, with the QPD variance (red). The trap stiffness, here, is lower than in Figure 4.14.

A possible explanation of the unexpected trend is the change in brightness of the collected images. As the integration time is decreased, so is the amount of light that reaches the camera. Figure 4.16 shows two images of the same bead taken with two different integration times. The contrast between the bead and its surroundings is lower for the smaller integration time, due to the lower amount of light collected.

As a result, the analysis program is likely unable to properly detect the variance of the particle. To test this, I manually decreased the intensity in the recorded image from the illumination source. Figure 4.17 shows the variance as a function of the background intensity of light for the manually decreased light intensity and due to the change in integration time. For the same bead, with lower illumination, the variance detected by the camera is decreased.

Interestingly, the brightest intensities (navy blue triangles in Figure 4.17), which were taken from the calibration files ( $W = 2.00 \times 10^{-3}$  s), do not show a significant increase in the variance ratio between camera and QPD. According to Equation 4.3, the measured variance from the camera at these settings should be decreased by only 5.1%, relative to the true value, which is not reflected in Figure 4.17. The ratios of variance from the camera to the QPD in experiment for these values were 0.643 for light intensity = 17700 and 0.710 for light intensity = 8500, indicating a potential plateau for the variance.

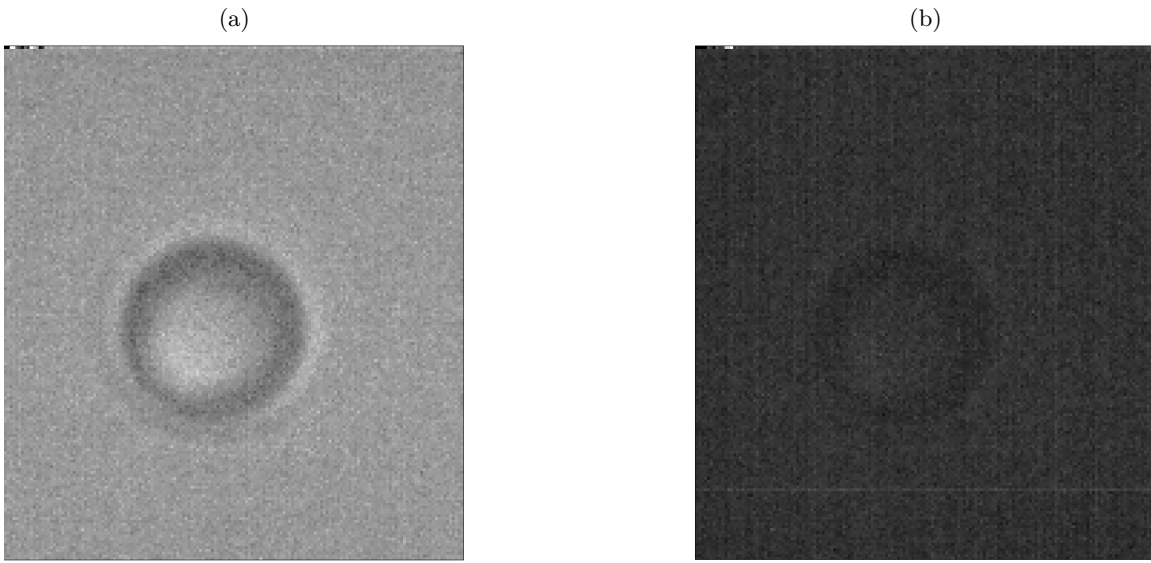


Figure 4.16: The same bead imaged with different integration times. (a)  $W = 3.96 \times 10^{-4}$  s and (b)  $W = 9.6 \times 10^{-5}$  s.

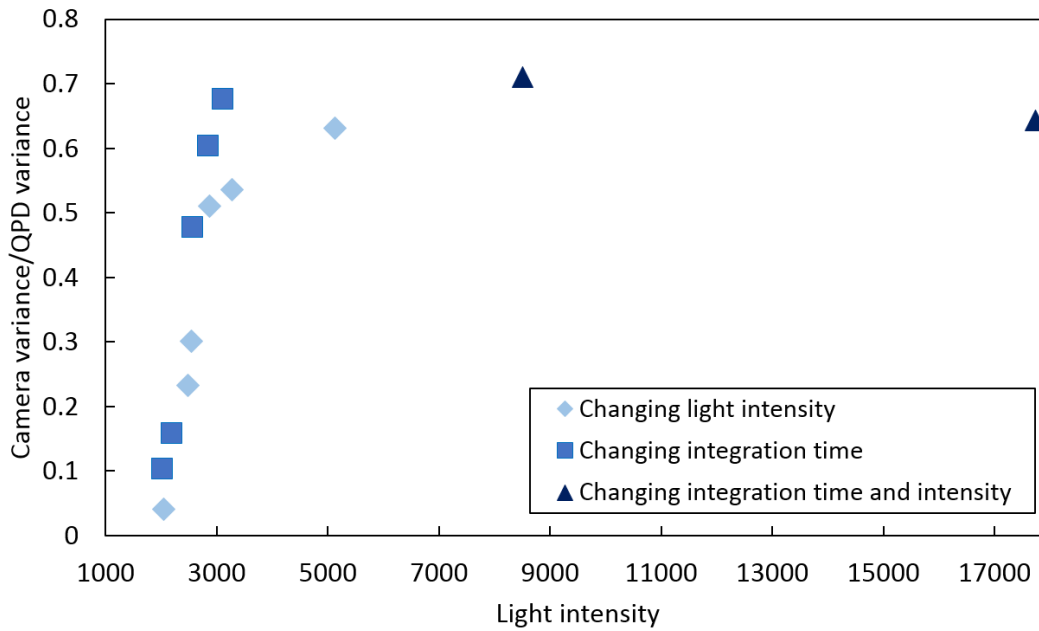


Figure 4.17: Variance as a function of background image intensity for the camera images. The illumination intensity was decreased manually while maintaining  $W = 3.96 \times 10^{-4}$  s (light blue), the integration time of the camera was varied, with a fixed illumination intensity (dark blue), or both (navy). The variance is presented as the ratio of variance as detected by the camera to that detected by the QPD to account for differences in bead size or trap stiffness between the two sets of measurements.

## 4.6 Conclusions from the OT-based experiments of a bead in water using the high-speed camera

To summarize the results of these experiments, Figure 4.18 shows the ratio of  $D$  from the camera to that of the QPD as a function of laser power. As observed, there is no trend between apparent diffusion constant and laser power. At lower light intensities, whether by manually adjusting the illumination or by decreasing the integration time, the variance of the particle as calculated by the analysis program decreases. However, even the brightest light intensities, obtained with  $W = 2.00 \times 10^{-3}$  s, show a variance discrepancy contrary to the expected values. Future experiments may want to investigate using an increased light intensity during experiments. Additionally, it may worthwhile determining bead position using other analysis routines, to see if other algorithms do better at capturing the expected variance of the particle. Unfortunately, the ratio between diffusion constants is also too disperse to allow the implementation of a simple rescaling factor between the two measurements.

Anticipating that the discrepancy between the camera and QPD diffusion constant might be resolved in the future, I now focus on the original question of determining how data acquisition with a high-speed camera might impact the extraction of the complex shear modulus.

Recall, the complex shear modulus is vital to understand the frequency-dependent behaviour of complex fluids, such as collagen. As a simple example, Figure 4.19 shows the complex shear modulus for water from the QPD and high-speed camera.  $G^*(f)$  has been averaged from three trials. Section 2.4.2 describes the analysis process of obtaining the components of the complex shear modulus from the power spectral density of bead positions. The data has been binned for clarity. The offset between QPD and camera is apparent. However, both  $G'(f)$  and  $G''(f)$  exhibit the expected trends associated with water (see Section 2.5):  $G'(f)$  exhibits a plateau characteristic of a constant-stiffness trap, and  $G''(f)$  increases linearly with frequency. Effects due to the measurement devices are also apparent. At high frequencies higher than approximately 100 Hz, the elastic modulus,  $G'(f)$ , decreases from the expected plateau due to the effects of limited integration, as discussed in Section 3.4.  $G''(f)$  is decreased by finite sampling, albeit at higher frequencies. From these, it is difficult *a priori* to estimate the range of data that should be fitted to extract the viscosity and elasticity (trap stiffness). Indeed, for a fluid of unknown viscous and elastic properties, it would be especially important to know where the trusted data lies. This is investigated in the following chapter.

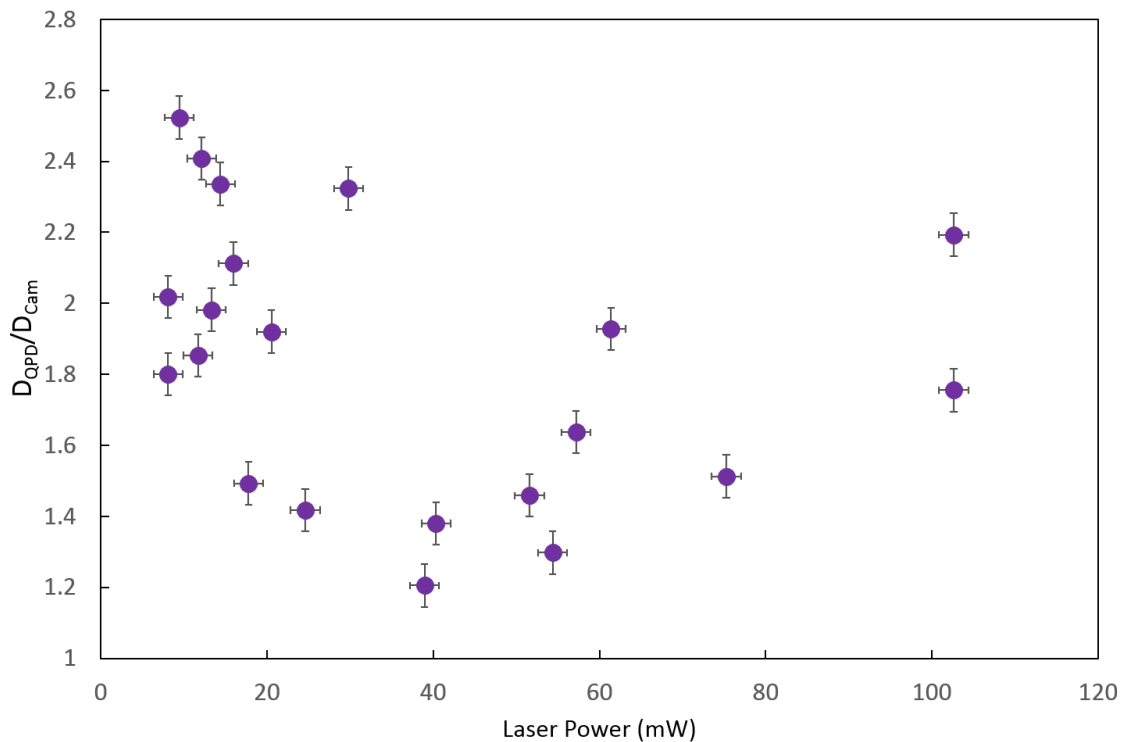


Figure 4.18: The ratio of diffusion constant of the camera to that of the QPD as a function of laser power for 21 independent bead measurements.

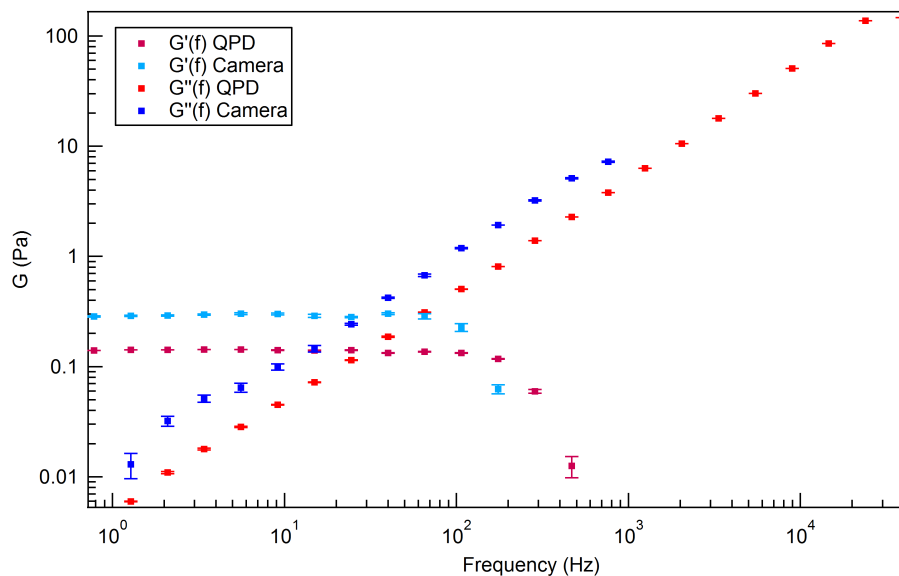


Figure 4.19:  $G'(f)$  (burgundy) and  $G''(f)$  (red) from the QPD and  $G'(f)$  (sky blue) and  $G''(f)$  (royal blue) from the camera. The camera values are similar but offset to the QPD values. At high frequencies, the moduli drop off due to the limited integration in Equation 2.19.

## Chapter 5

# Numerical representations of microrheological experiments using optical tweezers

As shown in Chapter 4, both components of the complex shear modulus of water drop off at higher frequencies in my experiments. It is therefore necessary to determine a range over which the data represent the correct values. Particularly, for a previously uncharacterised viscoelastic fluid, the frequency at which this drop-off occurs is of particular importance. In this chapter, I set out to numerically represent the QPD and camera data for a bead trapped in water, and determine the frequency range over which each device is accurate by comparing to a theoretical, expected trend. In addition to achieving this goal, I discuss how to apply what I have learned to achieve more accurate results in future work.

### 5.1 Introduction to the program

My code, written in Matlab and available in Appendix A, starts with the basics of a bead of radius  $R = 1 \mu\text{m}$  fluctuating in water within the confines of an optical trap. The system is given a temperature  $T = 21.85^\circ\text{C}$  ( $T = 295 \text{ K}$ ). I calculate the viscosity of water using

$$\eta(T [^\circ\text{C}]) = \eta(20^\circ\text{C}) 10^{\left(\frac{20-T}{96+T}\right) [1.2364 - 1.37 \times 10^{-3}(20-T) + 5.7 \times 10^{-6}(20-T)^2]} \quad (5.1)$$

from [82] and where  $\eta(20^\circ\text{C}) = 1.002 \times 10^{-3} \text{ Pa}\cdot\text{s}$  has been well established [83, 84, 85]. This gives  $\eta(21.85^\circ\text{C}) = 9.5812 \times 10^{-4} \text{ Pa}\cdot\text{s}$ . These chosen values differ somewhat from experiments directly (where the beads are typically of radius  $1.445 \mu\text{m}$  and the temperature is  $22^\circ\text{C}$ ) but provide convenient values for investigating trends, and may be of relevance to others. Based on these values, I am able to define a diffusion constant,  $D$ , as in Equation

2.13. I also introduce a trap stiffness via a corner frequency. To begin, I use  $f_c = 100$  Hz; therefore,  $\kappa = 1.13 \times 10^{-3}$  pN/nm from Equation 2.17.

Additionally, I create a discrete variable for frequency which increases from  $f = 1$  Hz (corresponding to a measurement time of  $T_{\text{msr}} = 1$  s) in 1 Hz increments up to a defined Nyquist frequency. The Nyquist frequency depends on the device being numerically represented. The power spectral density is defined at each frequency using Equation 2.15 and Equation 2.18 is used to convert the  $PSD(f)$  to  $A''(f)$ . The Kramers-Kronig relation (Equation 2.19) is used to achieve  $A'(f)$ . The complex shear modulus ( $G'(f)$  and  $G''(f)$ ) is established using Equation 2.20.

There are three varieties of data of interest: the data as if collected by a QPD (QPD-like); the data as if collected by a high-speed camera (camera-like); and the theoretically expected data (infinite bandwidth). The theoretical data avoids the drop-off at high frequencies and enables, by comparison, the determination of the effects of aliasing, blur, Nyquist frequency, and integration method. For the purpose of this exercise, errors associated with position detection (Sections 3.3.1 and 3.3.2) are omitted from the calculations for both QPD-like and camera-like data.

### 5.1.1 Numerical representation of the theoretical data

The theoretical power spectral density is described by a Lorentzian function (Equation 2.15), and is shown in Figure 5.1. The data are plotted over a frequency range which enables us to see the different regimes of behaviour, and will serve as reference for comparison with the camera-like and QPD-like results. It is important to note that while this data is technically produced as discrete points, because the PSD and the equations to follow ( $A'(f)$ ,  $A''(f)$ ,  $G'(f)$ , and  $G''(f)$ ) all have analytical forms, these are all exact for  $\Delta f = 1$  Hz.

Using Equation 2.18 and the data in Figure 5.1,  $A''(f)$  can be calculated, as shown in Figure 5.2b. According to Section 2.4.2 and the Kramers-Kronig relation,  $A''(f)$  must be integrated to get  $A'(f)$ . The principal value integral can be integrated directly from zero to  $\infty$ :

$$A'(f) = \frac{2}{\pi} P \int_0^{\infty} \frac{\xi A''(\xi)}{(\xi^2 - f^2)} d\xi = \frac{D}{2\pi^2 k_B T} \int_0^{\infty} \frac{\xi^2}{(\xi^2 - f^2)(\xi^2 + f_c^2)} d\xi. \quad (5.2)$$

where  $P$  denotes the Cauchy principal value integral. The result of this integration is

$$A'(f) = \frac{D f_c}{2\pi k_B T (f^2 + f_c^2)}. \quad (5.3)$$

The details of this calculation are in Appendix B. Briefly, it is calculated by breaking this integral into partial fractions and being mindful of the pole at  $\xi = f$ . The result is plotted in Figure 5.2a.

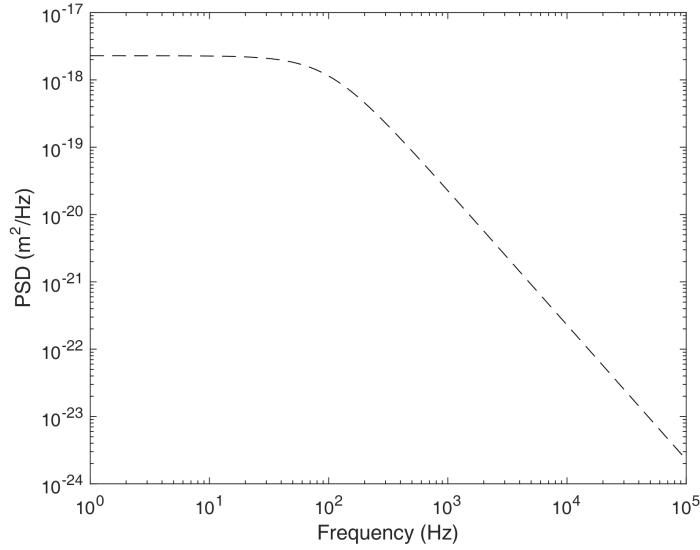


Figure 5.1: The theoretical power spectral density described by a Lorentzian function for a bead trapped in water with radius,  $R = 1 \mu\text{m}$ , temperature  $T = 295 \text{ K}$  and corner frequency,  $f_c = 100 \text{ Hz}$ .

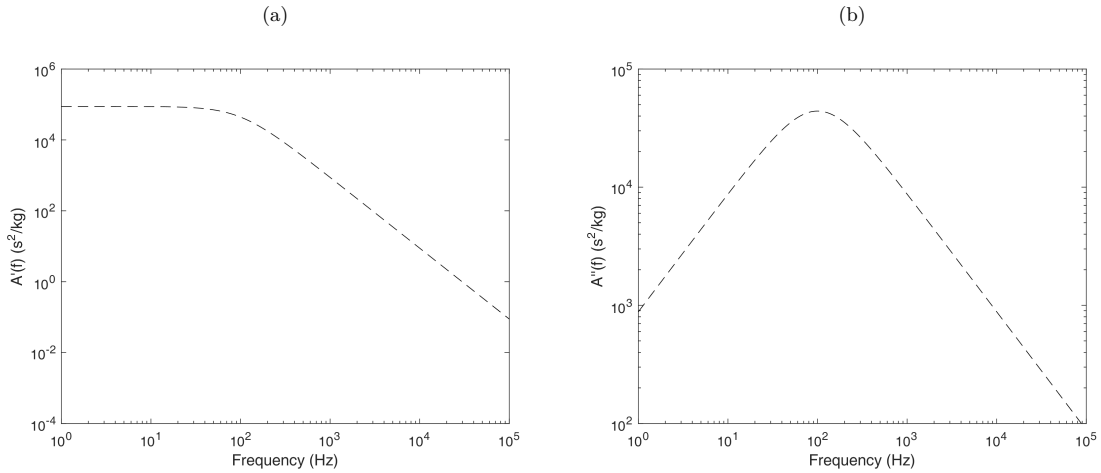


Figure 5.2: Theoretical (a)  $A'(f)$  and (b)  $A''(f)$  as described by Equations 5.3 and 2.18, respectively, generated using MatLab (Appendix A).

Subsequently, from Equations 2.21 and 2.22, we calculate the complex shear modulus,  $G'(f)$  and  $G''(f)$ , shown in Figure 5.3. In Figure 5.3a, the flat, straight line in the  $\log(G'(f))$  vs  $\log(f)$  is indicative of water's purely viscous nature and thus the only elasticity in the system is that of the optical trap, whose value of  $\kappa = 1.13 \times 10^{-3}$  pN/nm (equivalent to the input) is obtained through Equation 2.24 and the  $G'(f)$  intercept. The slope of the  $\log(G''(f))$  vs  $\log(f)$  plot in Figure 5.3b is exactly 1 and the intercept leads to the given input value of  $\eta = 9.5812 \times 10^{-4}$  Pa·s via Equation 2.25. In summary, the theoretical data shows the correct trends for the system of interest, thus validating my program.

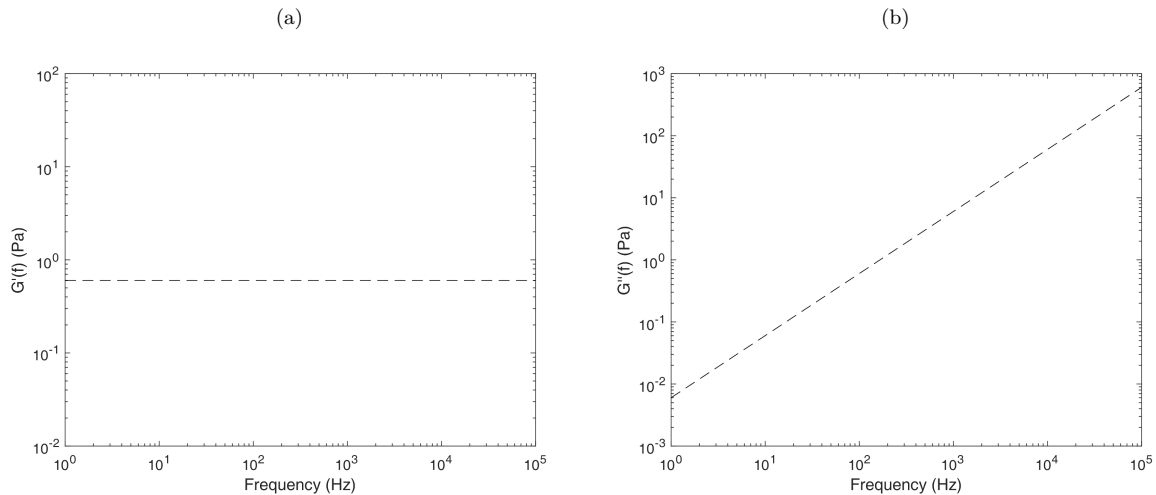


Figure 5.3: Theoretical (a) elastic and (b) viscous shear moduli as described by Equations 2.21 and 2.22, respectively. The output viscosity from the intercept of (b) gives the exact input value of  $\eta = 9.5812 \times 10^{-4}$  Pa·s while the plateau of (a) can be used to recover the input value of  $f_c = 100$  Hz.

### 5.1.2 Numerical representation of QPD-like data

In experiments in Chapter 4, the QPD has sampling frequency of  $f_s = 100\,000$  Hz. Because of this finite bandwidth, aliasing is taken into account in Equation 3.3, which is used to numerically represent the QPD-like PSD with  $N = 2$ . Equation 5.3 does not describe the QPD-like  $A'(f)$  since it requires an integration to infinite frequency. Therefore, I implement the use of the analysis code from experiment, initially developed by Marjan Shayegan [45], which uses the trapezoidal integration of the discrete PSD.

The calculated QPD-like PSD (Figure 5.4) appears unsurprisingly similar to the theoretical expectation, except at its tail end. At high frequencies, we can see the effects of limited bandwidth. First, the data is limited to the Nyquist frequency,  $f_{\text{Nyq}} = 50\,000$  Hz,

while the previous PSD extends to infinite frequency (until the end of the plotted range in Figure 5.1). Second, by making a comparison between aliased (Equation 3.3 and in red in Figure 5.4) and non-aliased (Equation 2.15 and in black in Figure 5.4) results, we see that the aliasing introduced due to the limited bandwidth causes the power at the highest frequencies of the QPD-like PSD to increase and flatten.

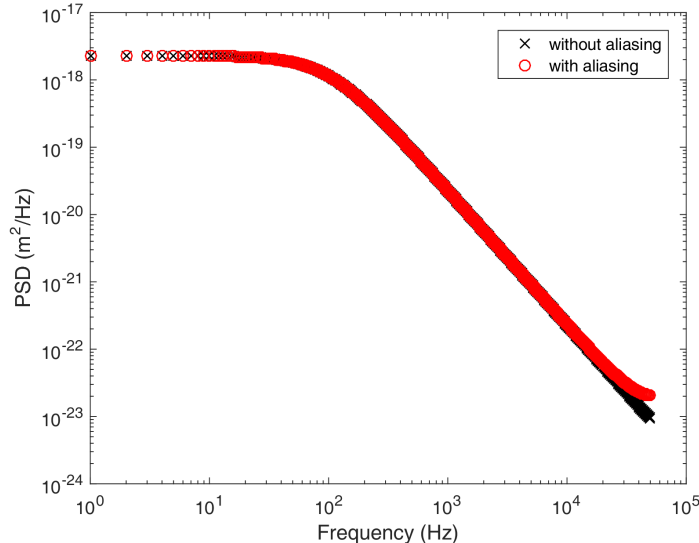


Figure 5.4: The numerically calculated QPD-like power spectral density describing a Lorentzian function with aliasing (red) and without aliasing (black). The PSD has sampling frequency  $f_s = 100\,000$  Hz, for a bead in water with radius  $R = 1\ \mu\text{m}$ , temperature  $T = 295$  K, and corner frequency  $f_c = 100$  Hz. The only significant difference between the aliased and non-aliased data is at frequencies approaching the Nyquist frequency.

Figure 5.5 shows the QPD-like  $A'(f)$  and  $A''(f)$ . The effects of the cut-off due to the Nyquist frequency and the resulting aliasing are apparent at high frequencies of  $A''(f)$  in Figure 5.2b.  $A'(f)$  in Figure 5.5a experiences a drop-off at high frequencies. This drop-off is expected because the absence of  $A''(f)$  values beyond the Nyquist frequency affects the area calculated in the integral in Equation 2.18 and therefore, the integral becomes highly underestimated. This will be discussed further in Section 5.2.3.

Figure 5.6 shows the components of the QPD-like complex shear modulus. From Equation 2.20,  $G'(f)$  and  $G''(f)$  are both calculated with  $A'(f)$  and therefore, both exhibit a drop-off at high frequencies. Specifically,  $G'(f)$  predicts a frequency-independent elasticity (trap only) up to approximately  $f = 1000$  Hz, after which the  $G'(f)$  values begin to fall rapidly.  $G''(f)$  appears to exhibit the expected linear dependence on frequency, up to higher but still limited frequencies. These will be compared quantitatively with theoretical predictions in Section 5.2.

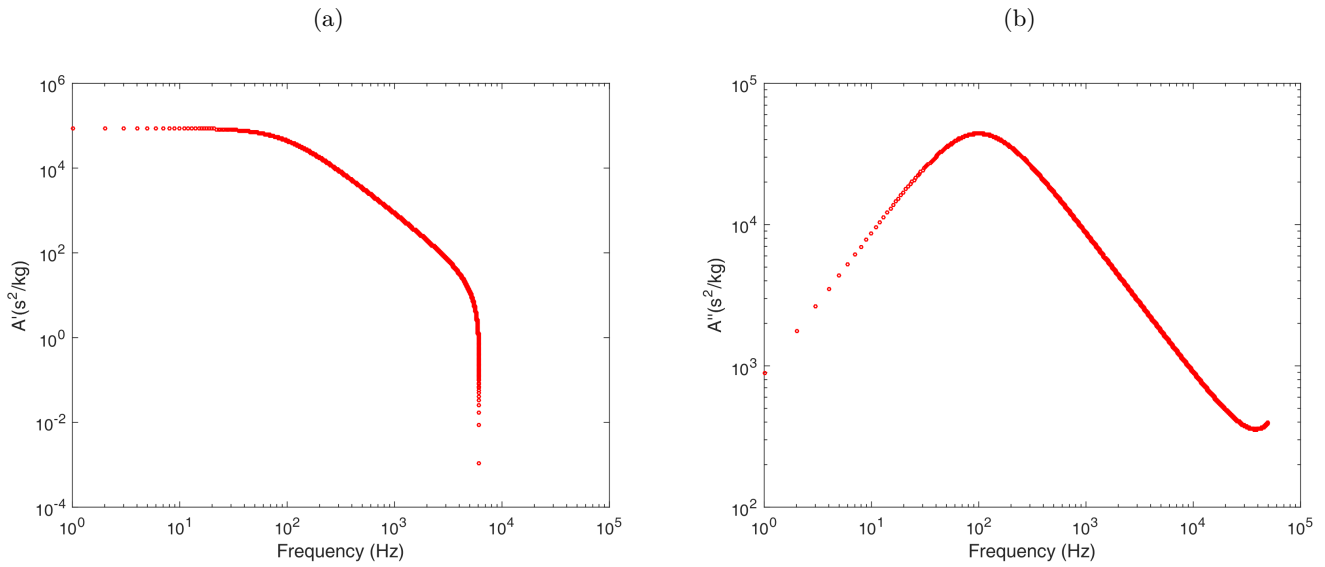


Figure 5.5: QPD-like (a)  $A'(f)$  and (b)  $A''(f)$  including aliasing.  $A''(f)$  is described by Equation 2.18 with input data from Figure 5.4 (red) and  $A'(f)$  is the integral of this  $A''(f)$  according to Equation 2.19 with the integration limited by the Nyquist frequency.

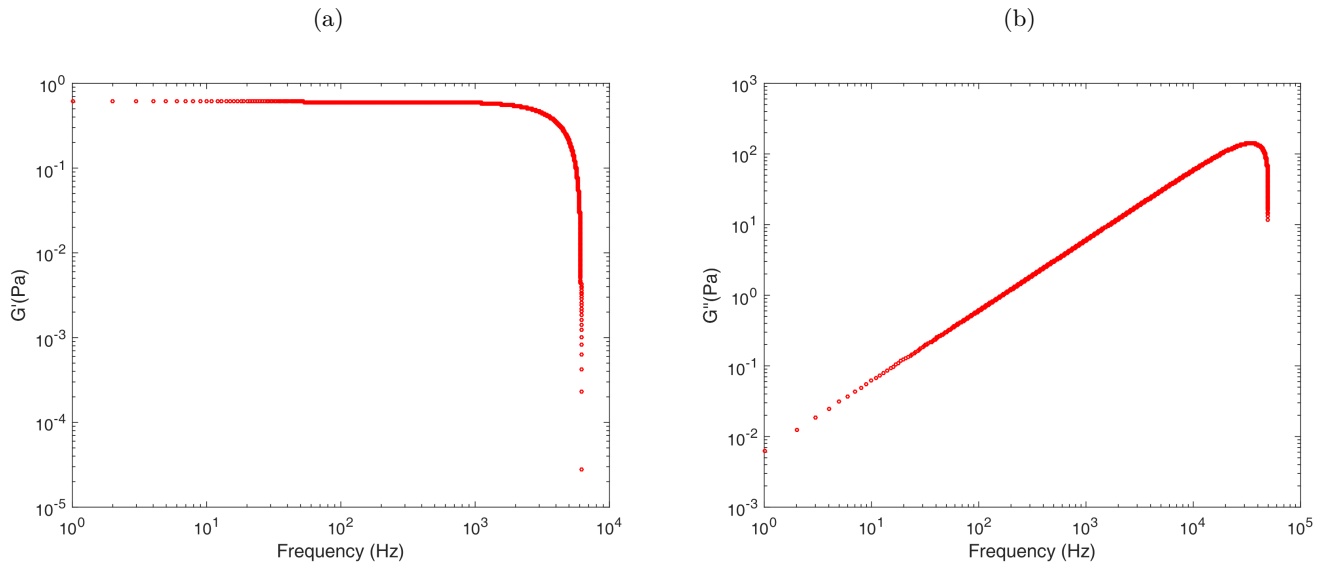


Figure 5.6: QPD-like (a) elastic and (b) viscous shear moduli including aliasing. A drop-off occurs in both moduli at high frequencies.

### 5.1.3 Numerical representation of the camera-like data

Equation 3.5, without the last term (detection error) and with a sum from  $n = -2$  to 2, is used to describe the camera-like PSD. Since experimental camera data is limited to approximately 2500 fps, I use  $f_{\text{Nyq}} = 1250$  Hz in the numerical calculations. Additionally, the integration time ( $W$ ) in experiments is selected in the camera's interface program and the frame rate is calculated accordingly. The relationship is not trivial, however, here, I used a simplified idea that  $W = \frac{1}{f_s} = 4.0 \times 10^{-4}$  s (in experiments, this value is  $W = 3.96 \times 10^{-4}$  s).

The resulting camera-like PSD is shown in Figure 5.7. The lower Nyquist frequency is evident because the cut-off occurs much earlier at 1250 Hz, rather than the QPD-like data's 50 000 Hz. The shape of the camera-like PSD is similar the QPD-like, however the 'curl-up' in power spectral density at the highest frequencies (greater than  $f = 1000$  Hz) is caused by the sinc function in Equation 3.5.

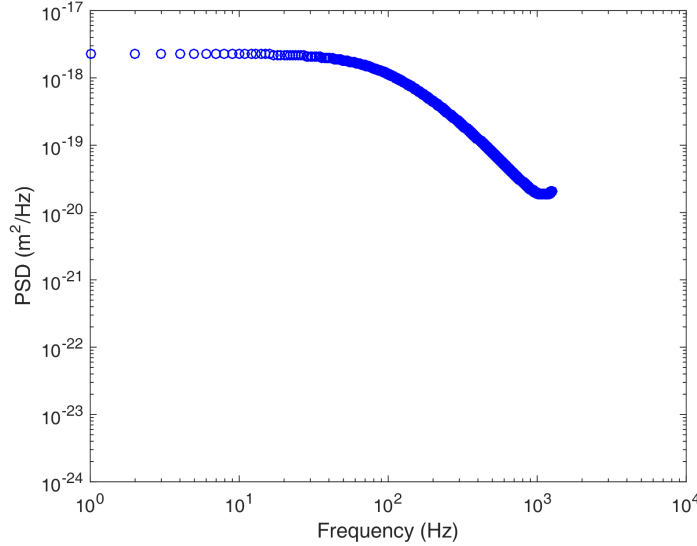


Figure 5.7: Camera-like power spectral density describing a Lorentzian function including aliasing and blur (Equation 3.5 without the last term) as numerically calculated for a bead in water with radius  $R = 1 \mu\text{m}$ , temperature  $T = 295$  K and corner frequency  $f_c = 100$  Hz.

The calculated camera-like  $A'(f)$  and  $A''(f)$  are shown in Figure 5.8. The camera-like  $A''(f)$  in Figure 5.8b has the same shape as that for the QPD-like  $A''(f)$ , with, again, a lower frequency cut-off. The shape of the  $A'(f)$  in Figure 5.8a, however, is slightly different. It lacks the region of a defined straight line slope following the corner at  $f_c = 100$  Hz, and instead, curves more continuously down.  $G'(f)$  and  $G''(f)$  in Figure 5.9 appear qualitatively similar to the QPD-like versions albeit with a lower-frequency cut-off.

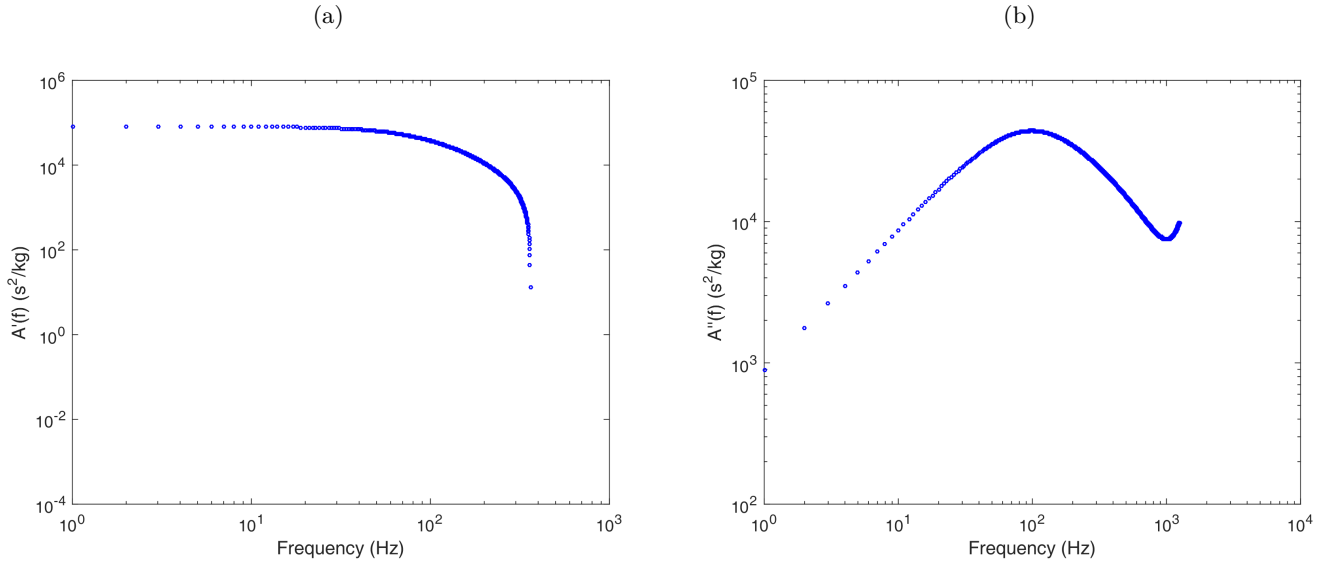


Figure 5.8: Camera-like (a)  $A'(f)$  and (b)  $A''(f)$  including aliasing and blur.  $A''(f)$  is described by Equation 2.18 with input data from Figure 5.7 and  $A'(f)$  is the integral of this  $A''(f)$  according to Equation 2.19 with the integration limited by the Nyquist frequency.

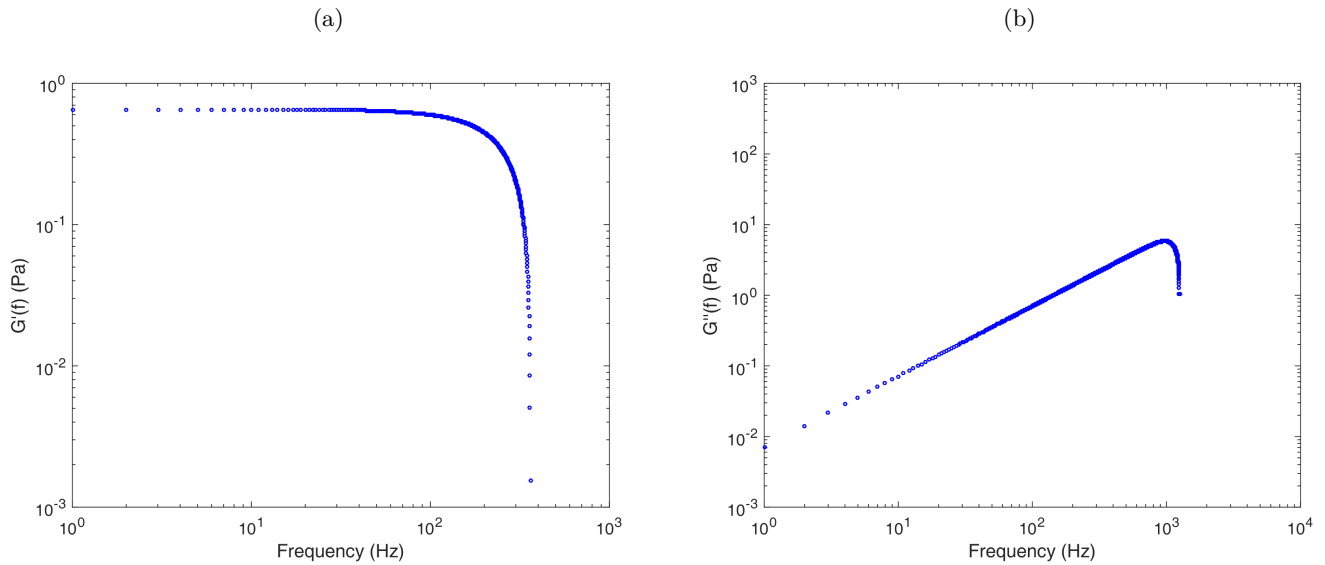


Figure 5.9: Camera-like (a) elastic and (b) viscous shear moduli including aliasing and blur. The frequency drop-off occurs in both graphs at high frequencies, which occur at lower frequencies than the QPD-like complex shear modulus due to the lower Nyquist frequency.

## 5.2 Comparison of camera-like, QPD-like, and theoretical data

Figure 5.10 shows a comparison of the power spectral density for the numerically represented QPD-like, camera-like, and theoretical cases. As expected, the only discrepancy observed is at high frequencies, wherein the Nyquist frequency, aliasing, and blur factors become apparent. Figure 5.11 contrasts  $G'(f)$  and  $G''(f)$  for all three cases. Upon close inspection, it is possible to identify a difference between the theoretical expectations and the data representing each device not just at high frequencies but also at the low frequencies, which was not anticipated. Therefore, in Figure 5.12, ratios of device-like to theoretical data are plotted to more clearly illustrate these phenomena. This analysis shows that  $G'(f)$  and  $G''(f)$  are overestimated at low frequencies by both device-like treatments. They then decrease at higher frequencies. For the QPD-like data,  $G'(f)$  is initially overestimated by 1% and  $G''(f)$ , by 2%. For the camera,  $G'(f)$  is initially overestimated by 9% and  $G''(f)$ , by 18%.

I sought to ascertain how much the determinations of solution viscosity and trap elasticity were affected by device-like measurements. In order to extract the correct values from  $G'(f)$  and  $G''(f)$ , I first set cut-off frequencies for each modulus to eliminate the expected high-frequency drop-offs from calculation. To determine these frequencies, the values of each modulus are compared to the expected trends of the data. For  $G'(f)$ , since we expect a flat line representing the elasticity of the trap in a Newtonian fluid, the maximum value of  $G'(f)$  from both device-like data is compared to each consecutive value. The frequency at which  $G'(f)/G'_{\max} \leq 0.9$  occurs is defined as the cut-off frequency for  $G'(f)$ . This value will be different for camera-like and QPD-like data. For  $G''(f)$ , a straight line with slope 1 is expected for a Newtonian fluid like water. Therefore, the cut-off frequency is the frequency at which the slope of  $G''(f)$  between consecutive points deviates from this by 10% (*i.e.*, if it falls to 0.9 or rises to 1.1).

Implementing these high-frequency cut-offs, viscosity was calculated from each  $G''(f)$  curve by fitting a line with a slope of 1 to the camera-like and QPD-like data up to the cut-off frequency. The intercept of that line, by Equation 2.25, leads to the viscosity. Similarly, the corner frequency obtained from this viscosity and the value of the plateau in  $G'(f)$  could be computed via Equation 2.24. For comparison purposes, I simply compare the plateau height of  $G'(f)$ .

The  $G''(f)$  intercept in Figure 5.11b from the QPD-like data reports a value of  $\eta_{\text{QPD}} = 9.31 \times 10^{-4}$  Pa·s while the camera-like data reports  $\eta_{\text{cam}} = 1.09 \times 10^{-3}$  Pa·s. Compared to the input (and theoretical output) value of  $\eta_{\text{theo}} = 9.58 \times 10^{-4}$  Pa·s, the QPD-like data underestimates the true value by 3% while the camera-like data overestimates it by 12%. It is obvious from the ratio plot of  $G''(f)$  in Figure 5.12b that the camera-like data overestimates the theoretical expectation at all points below  $f_{\text{cutoff}}$ , consistent with the overestimation of

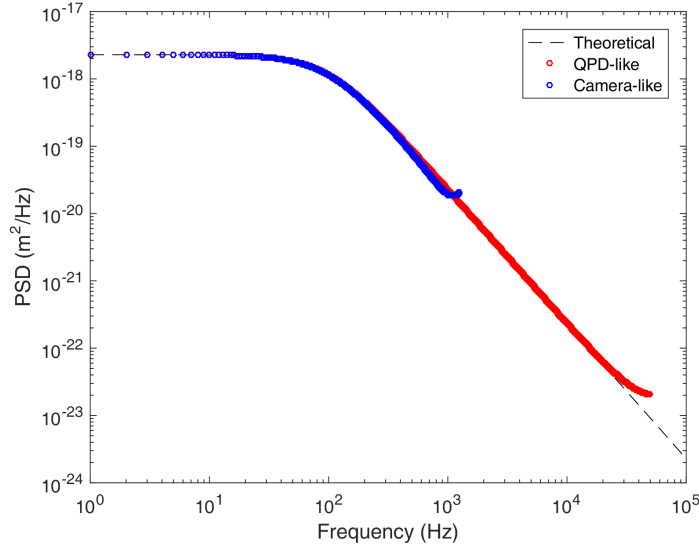


Figure 5.10: The power spectral densities for theoretical (black), QPD-like (red), and camera-like (blue) data describing a bead trapped in water with radius  $R = 1 \mu\text{m}$ , temperature  $T = 295 \text{ K}$ , and corner frequency  $f_c = 100 \text{ Hz}$ .

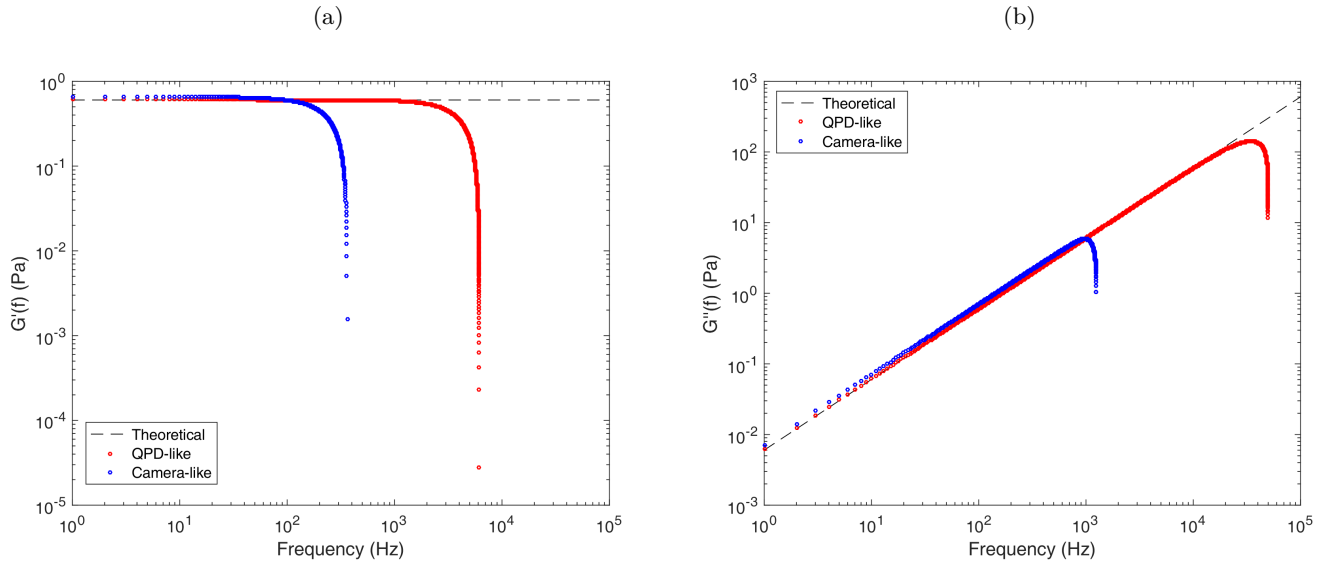


Figure 5.11: The (a) elastic and (b) viscous moduli for the theoretical (black), QPD-like (red), and camera-like (blue) data. The difference at high frequencies is evident and expected. The discrepancy at low frequencies, though more subtle, was not anticipated.

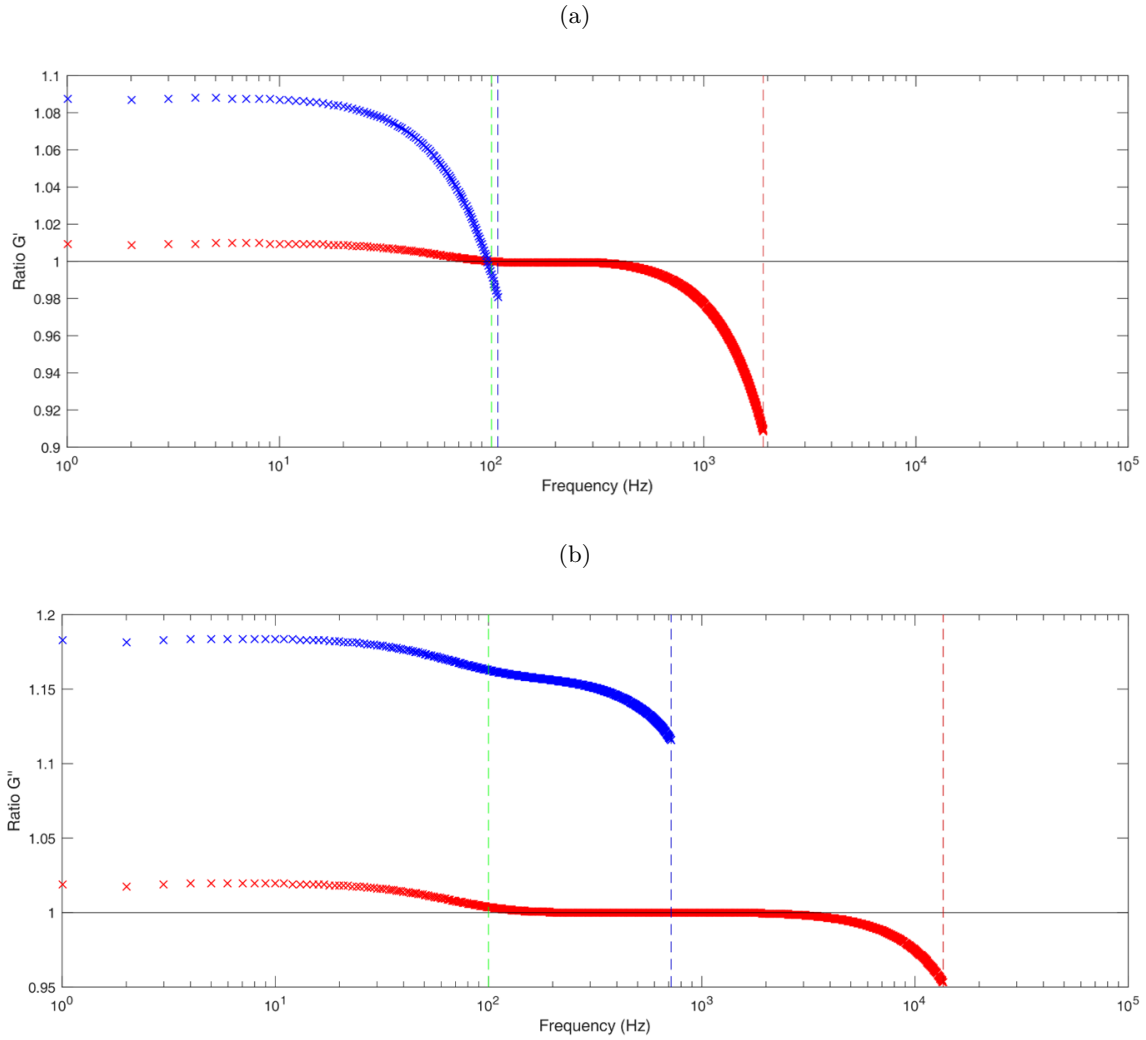


Figure 5.12: Ratios of (a)  $G'(f)$  and (b)  $G''(f)$  of the camera-like (blue) and QPD-like (red) to the theoretically expected  $G'(f)$  and  $G''(f)$ , respectively. The red and blue dashed lines show the cut-off frequencies as described in the text. For  $G'(f)$ :  $f_{\text{cutoff}} = 107$  Hz for the camera (blue) and  $f_{\text{cutoff}} = 1907$  Hz (red) for the QPD. For  $G''(f)$ :  $f_{\text{cutoff}} = 718$  Hz for the camera (blue) and  $f_{\text{cutoff}} = 13549$  Hz for the QPD (red). The green dashed lines show the corner frequency,  $f_c = 100$  Hz.

$\eta$ . In contrast, the ratios for the QPD-like  $G''(f)$  are underestimated at higher frequencies below  $f_{\text{cutoff}}$ . The underestimate of  $\eta$  from the QPD data likely arises because of the many data points at the tail end being included in the fit (the frequency axis is on the logarithmic scale but the data are sampled linearly).

Similarly, for  $G'(f)$ , the QPD-like data underestimate the theoretical plateau of  $G'_{\text{trap}_{\text{theo}}} = 0.602$  Pa with  $G'_{\text{trap}_{\text{QPD}}} = 0.585$  Pa and the camera-like data overestimate it with  $G'_{\text{trap}_{\text{cam}}} = 0.631$  Pa. The ratio plot of  $G'(f)$  in Figure 5.12a shows the camera-like data above the theoretical expectation, while the QPD-like data has many data points below the theoretical values at high frequencies.

Figure 5.13, which  $A'(f)$  and  $A''(f)$  as functions of frequency, illustrates that these differences (especially at low frequencies) in the plots from the QPD-like and camera-like complex shear modulus are caused by the finite integration, since  $A''(f)$  in Figure 5.13b, which doesn't involve any integration, shows only high-frequency discrepancies due to aliasing (and blur). In contrast,  $A'(f)$  (Figure 5.13a) shows differences at both low and high frequencies.

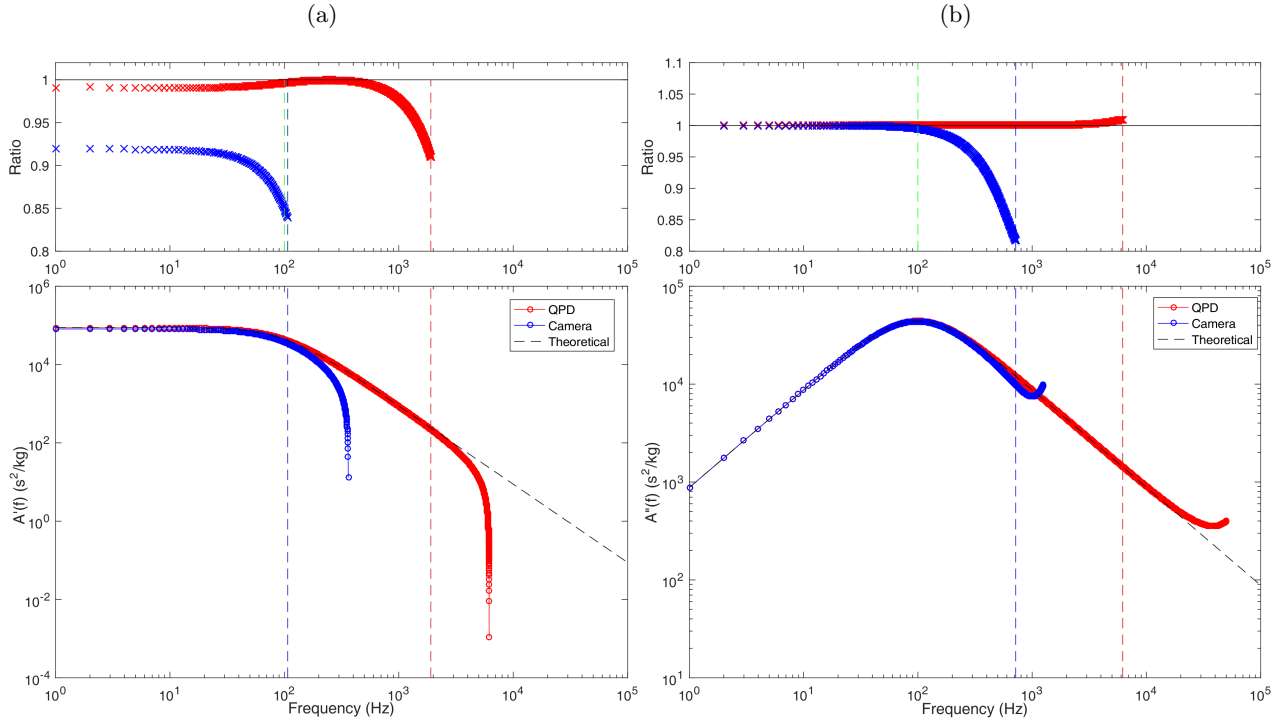


Figure 5.13: (a)  $A'(f)$  and (b)  $A''(f)$  for the theoretical (black), QPD-like (red), and high-speed camera-like (blue) data with ratio plots. Red and blue dashed lines show the cut-off frequencies for the QPD-like and camera-like data, respectively, and green dashed lines show the corner frequency, for reference. At low frequencies, there is a discrepancy only in  $A'(f)$ , implying that low-frequency differences arise from the finite integration that manipulates  $A''(f)$  into  $A'(f)$ .

### 5.2.1 The effects of varying corner frequency on the viscous and elastic outputs

Thus far, all data have been compiled with one corner frequency, namely  $f_c = 100 \text{ Hz}$ , which is an explicit input in the calculations. In this section, I aim to learn how the cut-off frequency varies with corner frequency, and how these changes might affect the viscosity output from  $G''(f)$ . Here, I present  $G'(f)$  and  $G''(f)$  for corner frequencies ranging from  $f_c = 50 \text{ Hz}$  to  $f_c = 350 \text{ Hz}$  with their respective ratio plots (Figures 5.14 - 5.16). The output values and frequency cut-offs from these plots are summarized in Figures 5.17 and 5.18. This range of corner frequencies is comparable to experiments.

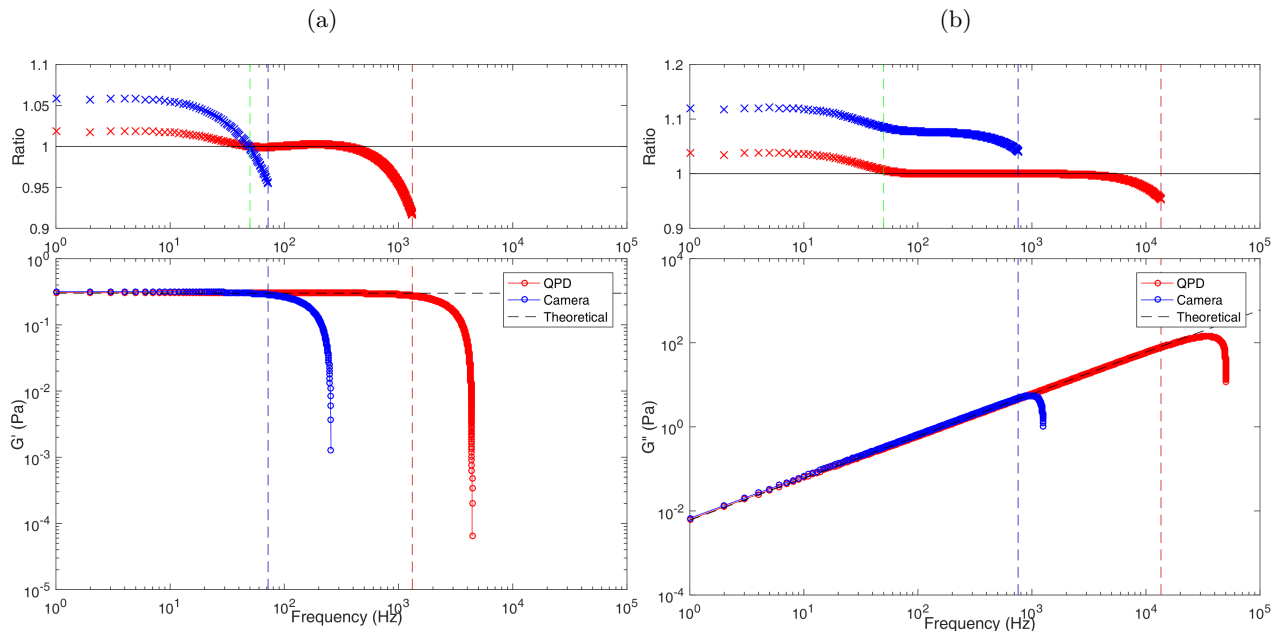


Figure 5.14: The (a) elastic and (b) viscous shear moduli for QPD-like (red), camera-like (blue), and theoretical (black) data with ratio plots for corner frequency,  $f_c = 50 \text{ Hz}$ . Red and blue dashed lines show the cut-off frequencies for the QPD-like and camera-like data, respectively, and green dashed lines show the corner frequency, for reference.

By examining in detail the ratio plots from  $G''(f)$  for the QPD-like data, it appears that the ratios start above 1, decrease to 1 for a range then decrease further. The inflections occur at a lower frequency than the corner frequency.

We can see a trend in cut-off frequencies as a function of increasing corner frequency in Figure 5.17. In general, the cut-off frequencies increase with corner frequency, with the exception being in  $G''(f)$  for the camera (Figure 5.17d) where the cut-off frequency decreases with increasing corner frequency. Figure 5.18 shows the output viscosity as a function of corner frequency. The QPD-like and camera-like viscosity both increase linearly with corner frequency.

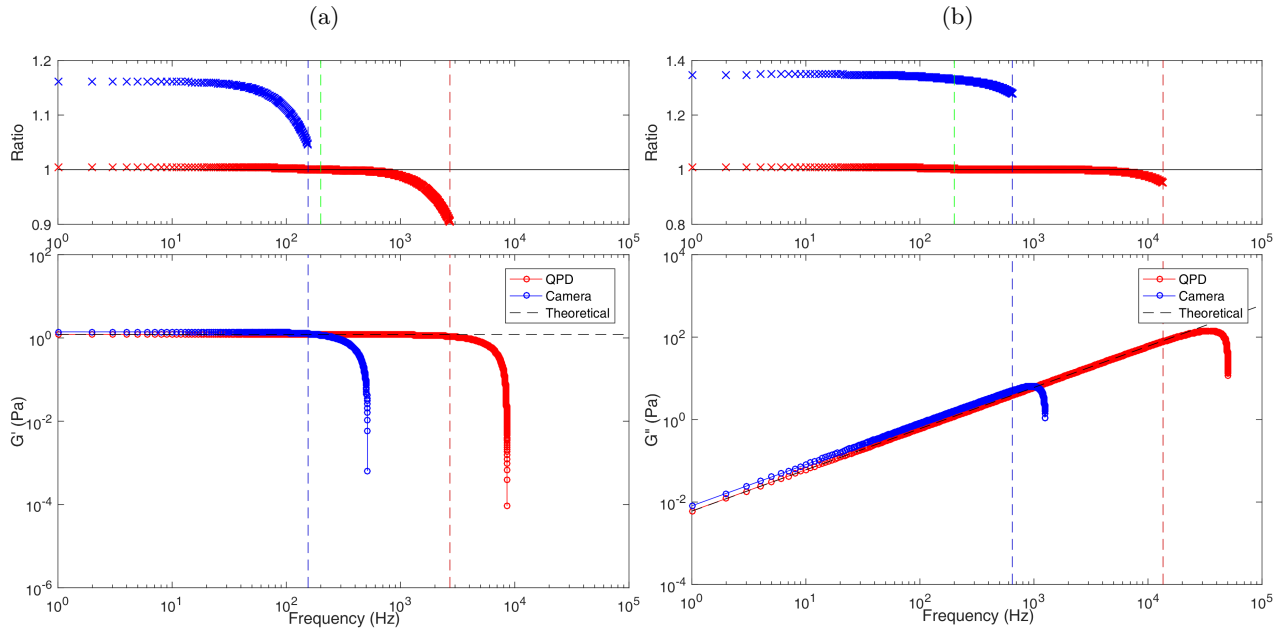


Figure 5.15: The (a) elastic and (b) viscous shear moduli for QPD-like (red), camera-like (blue), and theoretical (black) data with ratio plots for corner frequency,  $f_c = 200$  Hz. Red and blue dashed lines show the cut-off frequencies for the QPD-like and camera-like data, respectively, and green dashed lines show the corner frequency, for reference.

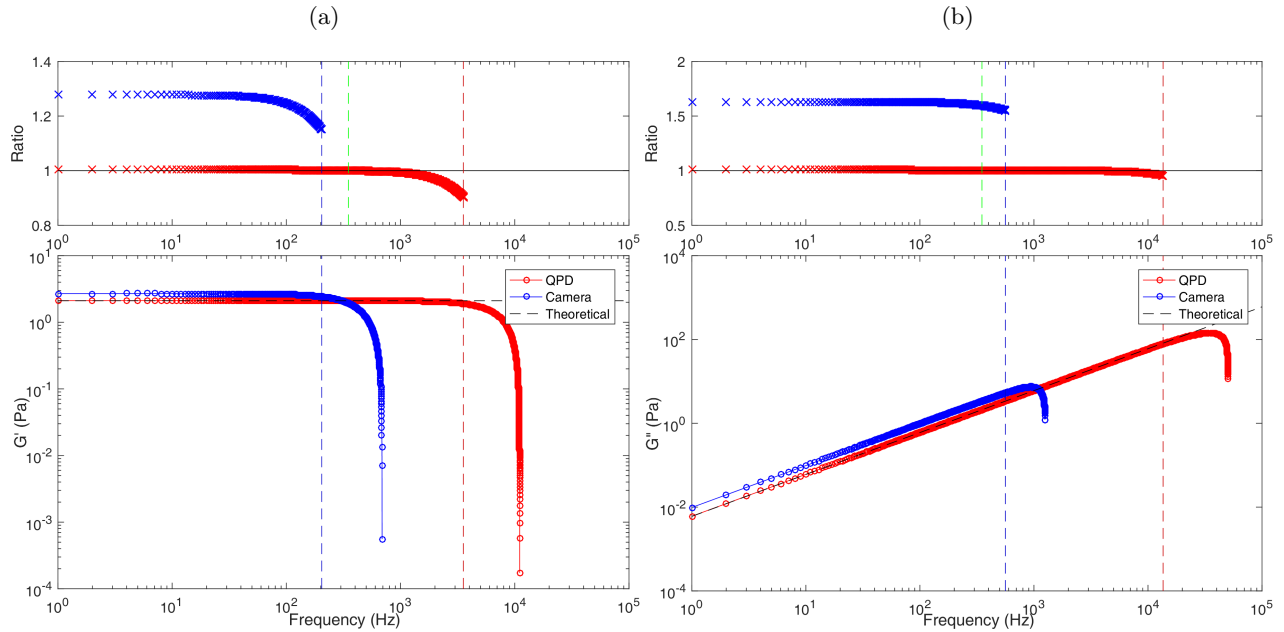


Figure 5.16: The (a) elastic and (b) viscous shear moduli for QPD-like (red), camera-like (blue), and theoretical (black) data with ratio plots for corner frequency,  $f_c = 350$  Hz. Red and blue dashed lines show the cut-off frequencies for the QPD-like and camera-like data, respectively, and green dashed lines show the corner frequency, for reference.

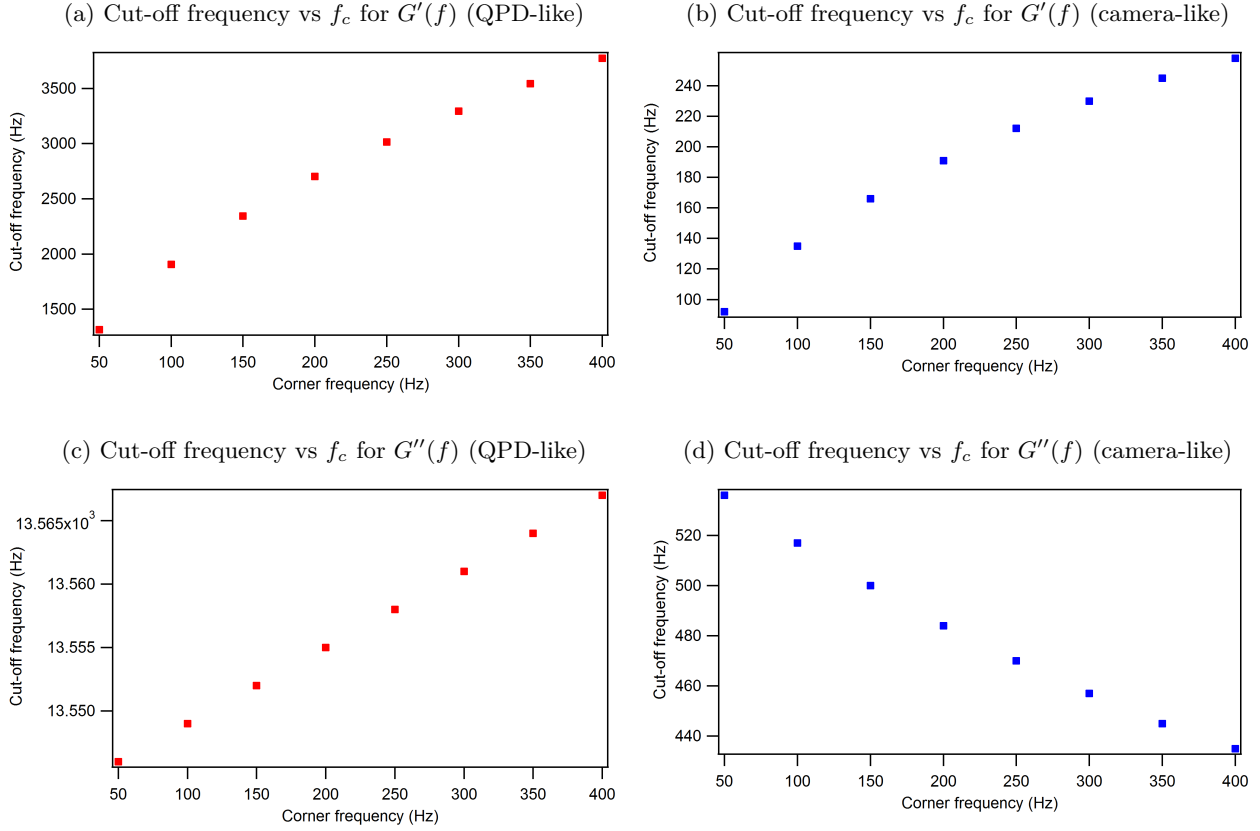


Figure 5.17: Variation of cut-off frequency with corner frequency for  $G'(f)$  ((a) QPD-like, (b) camera-like) and  $G''(f)$  ((c) QPD-like and (d) camera-like).

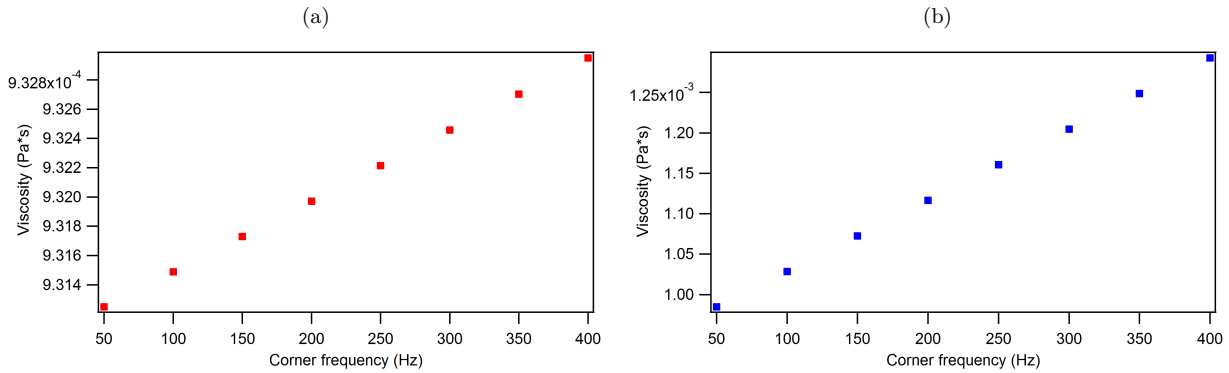


Figure 5.18: Calculated viscosity as a function of corner frequency for (a) QPD-like and (b) camera-like data. The expected (input) viscosity is  $\eta_{\text{theo}} = 9.58 \times 10^{-4}$  Pa·s.

Figure 5.19 shows  $G'_{\text{trap}}/f_c$  as a function of corner frequency. This plot reveals the deviations from the expected linearity. For low corner frequencies, the agreement between device-like data and the expected values is better. The camera-like  $G'_{\text{trap}}$  diverges more dramatically from the theoretical values and expected linear trend than the QPD-like  $G'_{\text{trap}}$  at higher corner frequencies.

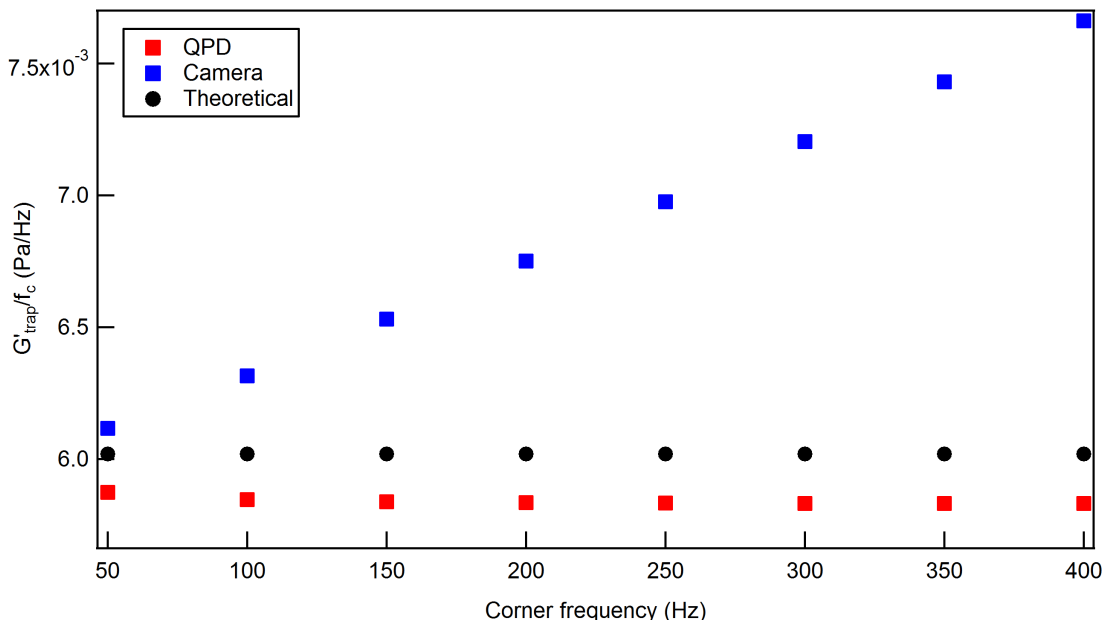


Figure 5.19:  $G'_{\text{trap}}$  versus corner frequency for QPD-like data (red), camera-like data (blue), and the expected value (black).

This study of the effects of corner frequency on the device-like complex is an important reminder that the range of data that follows the expected trend changes depending on the chosen trap stiffness, and therefore, the calculated viscosity and  $G'_{\text{trap}}$  change as well. For camera-like data, the change in viscosity is on the order of 25% over the range investigated here. For future experiments using the QPD, it is important to choose a high trap stiffness to maximize the data which can be included in  $G''(f)$  fits. However, to minimize the overestimation of the camera viscosity and  $G'_{\text{trap}}$ , it is advisable to use a lower corner frequency.

### 5.2.2 Effects of sampling frequency on QPD-like data

In this section, the sampling frequency for the QPD-like data is varied to try to understand how the limited bandwidth affects the integration in the Kramers-Kronig relation in Equation 2.19. Additionally, I hope to learn whether it is the blur or very limited frame rate that contributes to the higher ratios for the camera-like data.

Figure 5.20 shows  $A'(f)$  with sampling frequencies ranging from the usual  $f_s = 100$  kHz to  $f_s = 1900$  kHz. Only  $A'(f)$ , which shows the effects of limited integration, is shown,

since it is more strongly affected by finite sampling than  $A''(f)$  (Figure 5.13). Since  $A'(f)$  is the precursor to both  $G'(f)$  and  $G''(f)$ , any improvements made to  $A'(f)$  will improve the viscoelastic moduli.

The overall shape of  $A'(f)$  for the many  $f_s$  is maintained, while the cut-off frequency increases with sampling frequency. In the ratio plot, for higher  $f_s$ , the range of frequencies over which the ratio = 1 is extended, however, the low-frequency discrepancy is unchanged.

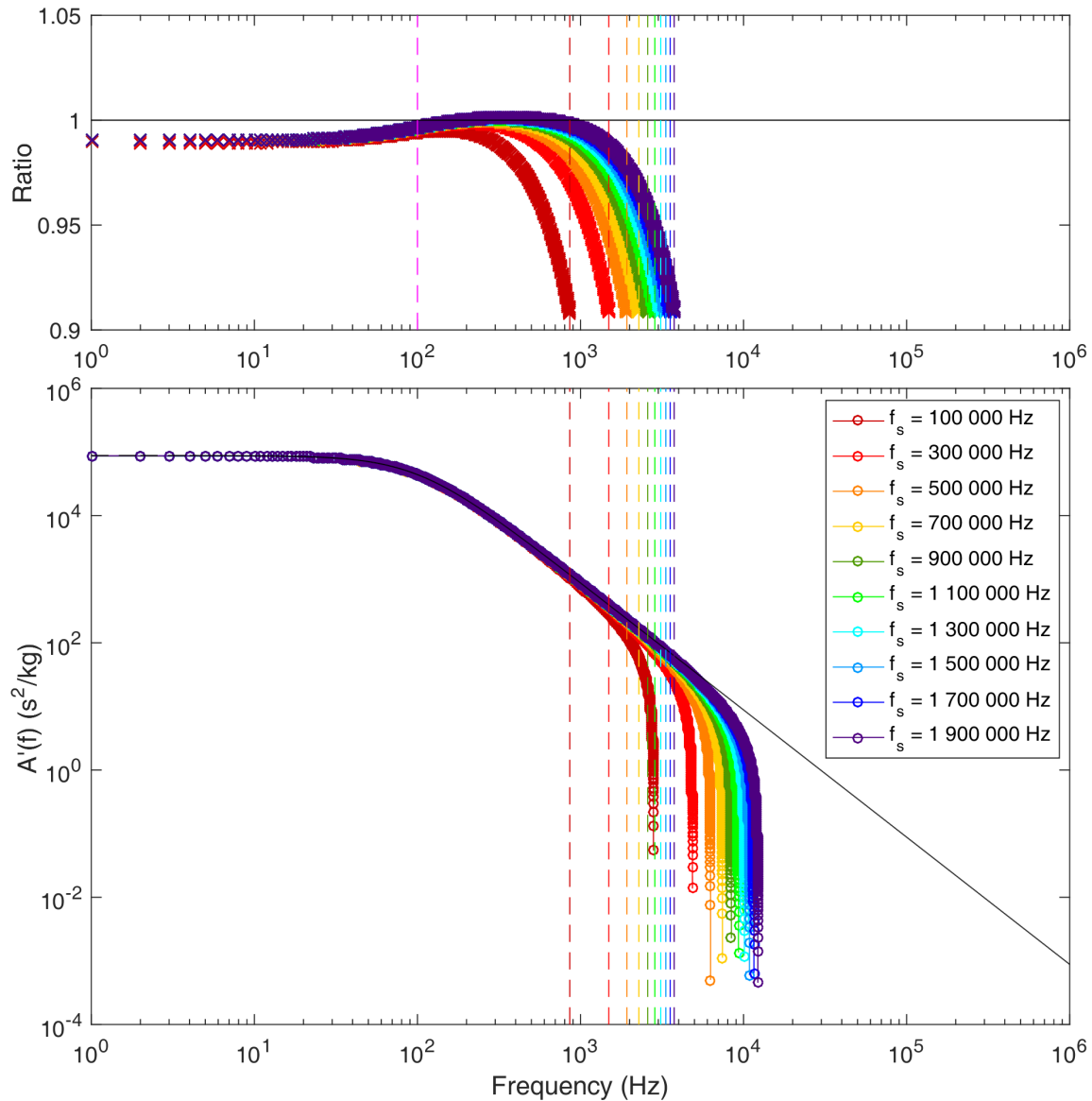


Figure 5.20: QPD-like  $A'(f)$  for sampling frequencies of  $f_s = 100\,000$  Hz to  $f_s = 1\,900\,000$  Hz, with ratios. The cut-off frequencies are represented by the dashed lines colour-corresponding to the sampling frequency, with the exception of the magenta dashed line in the ratio plot which is the corner frequency,  $f_c = 100$  Hz, for all results.

To differentiate between the effects of blur and reduced sampling frequency of camera-like data, Figure 5.21 compares camera-like shear modulus with a decrease in sampling frequency in the QPD-like data to  $f_s = 2500$  Hz. The cut-off frequency for  $G'(f)$  is worsened by the blur (107 Hz for camera-like vs 221 Hz for QPD-like), while it is improved for  $G''(f)$  (718 Hz for camera-like vs 344 Hz for QPD-like).

The added effect of blur in the camera-like data significantly affects the output values since the QPD-like data with  $f_s = 2500$  Hz continues to underestimate the  $G'(f)$  plateau, with  $G'_{\text{trap}_{\text{QPD}}} = 0.591$  Pa (compared to  $G'_{\text{trap}_{\text{theo}}} = 0.602$  Pa and  $G'_{\text{trap}_{\text{cam}}} = 0.631$  Pa). The viscosity from the QPD-like data for this case is overestimated, but not to the same extent as the camera-like data:  $\eta_{\text{QPD}} = 9.81 \times 10^{-4}$  Pa·s,  $\eta_{\text{cam}} = 1.09 \times 10^{-3}$  Pa·s, and  $\eta_{\text{theo}} = 9.58 \times 10^{-4}$  Pa·s.

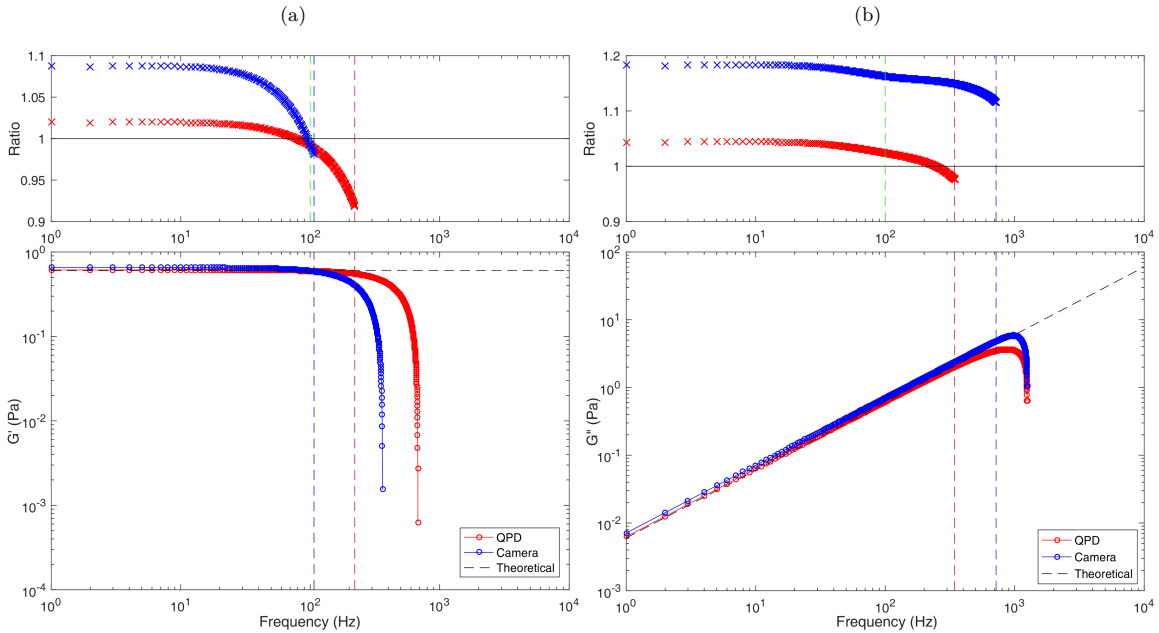


Figure 5.21: The (a) elastic and (b) viscous moduli for the theoretical (black), QPD-like at sampling frequency  $f_s = 2500$  Hz (red), and camera-like (blue) data, with ratio plots. The blur associated with the camera-like data worsens the estimate of the  $G'(f)$  plateau (trap stiffness) and the  $G''(f)$  intercept (viscosity). Red and blue dashed lines show the cut-off frequencies for the QPD-like and camera-like data, respectively, and green dashed lines show the corner frequency, for reference.

An increase in sampling frequency of the QPD-like data leads to a longer range over which the data exhibits the expected trend, however it does not affect the discrepancy at low frequencies. A decrease in sampling frequency of the QPD-like data and comparison

the camera-like data shows that the main reason for the overestimation of the camera-like outputs is due to the effects of blur.

### 5.2.3 Effects of the frequency spacing between discrete points

As previously mentioned, it is surprising that there exists a discrepancy between the QPD-like and theoretical moduli at low frequencies. To understand these low-frequency discrepancies, I investigate how the frequency step size affects the calculated data. Up until now, all QPD-like and camera-like power spectra (and subsequent mathematical calculations using the PSD) have used step sizes of  $\Delta f = 1$  Hz (or measurement time  $T_{msr} = 1/\Delta f = 1$  s), chosen as analogue to the experiment. Figure 5.22 shows the effect of varying  $\Delta f$  on the QPD-like  $A'(f)$  for step sizes of 1 Hz, 0.5 Hz, 0.2 Hz, and 0.1 Hz ( $T_{msr} = 1$  s, 2 s, 5 s, and 10 s, respectively).

At first glance, changing the spacing between data points has very little effect on the shape of  $A'(f)$ ; however, as the number of points per Hz is increased, the ratios at low frequencies get closer to 1. Take for example  $f = 1$  Hz. With the usual  $\Delta f = 1$  Hz (red in Figure 5.22), the ratio of  $A'(f)_{\text{QPD}}/A'(f)_{\text{theo}}$  is 0.9897 whereas for  $\Delta f = 0.1$  Hz, the ratio is 0.9977. Despite the difference being less than 1%, for a complex fluid with unknown shear modulus, improving estimates of the response function is important.

The camera-like data are slightly different. Figures 5.14, 5.15, 5.16, for example, show that the camera-like data always overestimate  $G'(f)$  and  $G''(f)$ , and never achieve an extended range of agreement. Figure 5.23 shows  $\Delta f = 1$  Hz,  $\Delta f = 0.1$  Hz, and  $\Delta f = 0.01$  Hz for the camera-like  $A'(f)$ . We see, again, a slight increase in  $A'(f)$  with decreasing  $\Delta f$ . Despite this shift, the camera-like data do not get as close to the ideal value as the QPD-like data. The ratio for  $\Delta f = 0.1$  Hz at  $f = 1$  Hz is 0.9275, compared to 0.9194 for  $\Delta f = 1$  Hz; again, less than a 1% improvement.

Figure 5.24 shows the QPD-like complex shear modulus for  $\Delta f = 0.1$  Hz and  $\Delta f = 1$  Hz. For both cases, the output viscosity remains the same,  $\eta = 9.31 \times 10^{-4}$  Pa·s, while the plateau of  $G'(f)$  is lowered to 0.582 Pa for  $\Delta f = 0.1$  Hz from 0.585 Pa  $\Delta f = 1$  Hz. This is further from the  $G'_{\text{trap,theo}} = 0.602$  Pa. These subtle changes are not unsurprising due to the influence of the values at the tail are included in these calculations.

Figure 5.25 shows the camera-like complex shear modulus for  $\Delta f = 0.1$  Hz and  $\Delta f = 1$  Hz. Again, the output viscosities are the same,  $\eta = 1.086 \times 10^{-3}$  Pa·s, and the plateau of  $G'(f)$  changes only slightly: 0.627 Pa for  $\Delta f = 0.1$  Hz ( $G_{\text{trap,cam}} = 0.531$  Pa for  $\Delta f = 1$  Hz). In the camera-like case, the  $G'(f)$  plateau is closer to the theoretical value for smaller  $\Delta f$ .

In all cases, the low-frequency estimates of  $G'(f)$  and  $G''(f)$  better approximate the theoretical expectation for lower  $\Delta f$ . This is due to the method of integration. In Equation 2.19, there is a pole at  $\xi = f$ , which makes the integration challenging. The analysis code [45] uses the trapezoidal method of approximating the result of the integral [86]. Essentially, it calculates the summation over all possible values and leaves out the pole

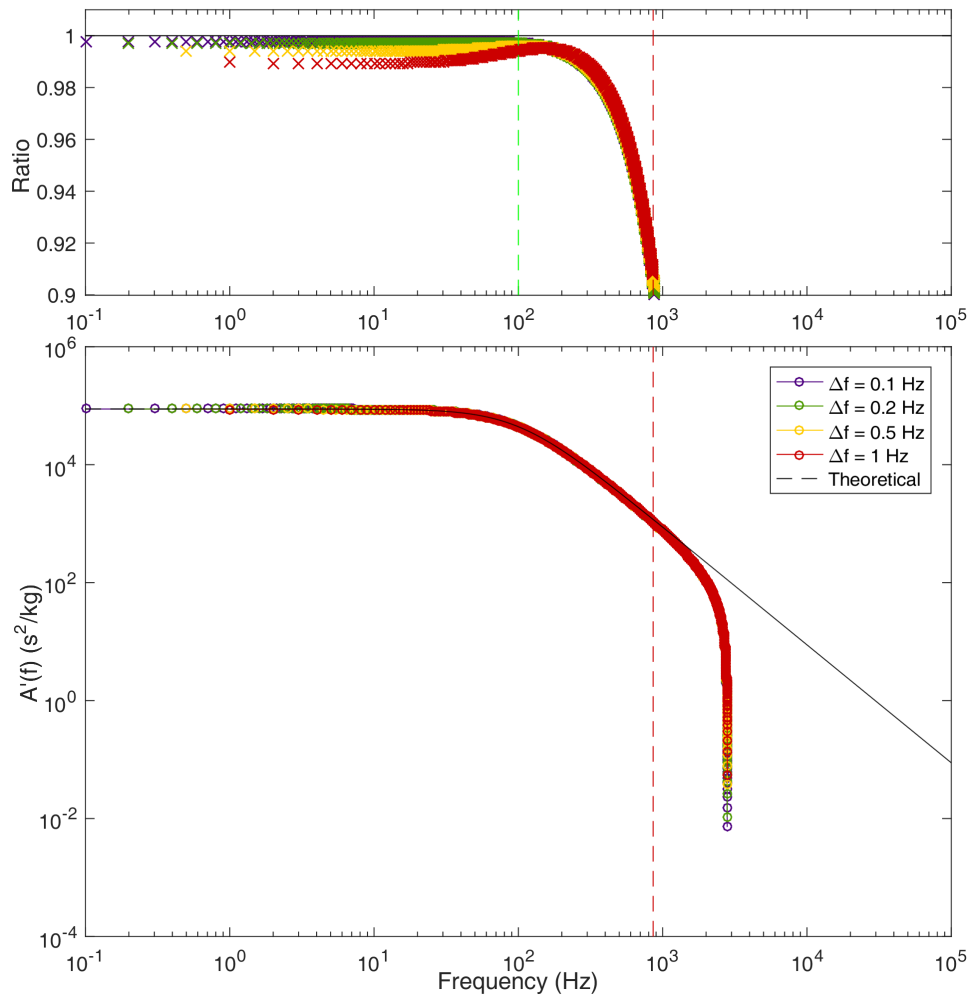


Figure 5.22: Changing the frequency step sizes that lead to the QPD-like  $A'(f)$ . The cut-off frequency (red dashed line) is 1907 Hz for all data, and the corner frequency (green dashed line) is 100 Hz. The ratio gets closer to 1 at low frequencies with decreasing step sizes.

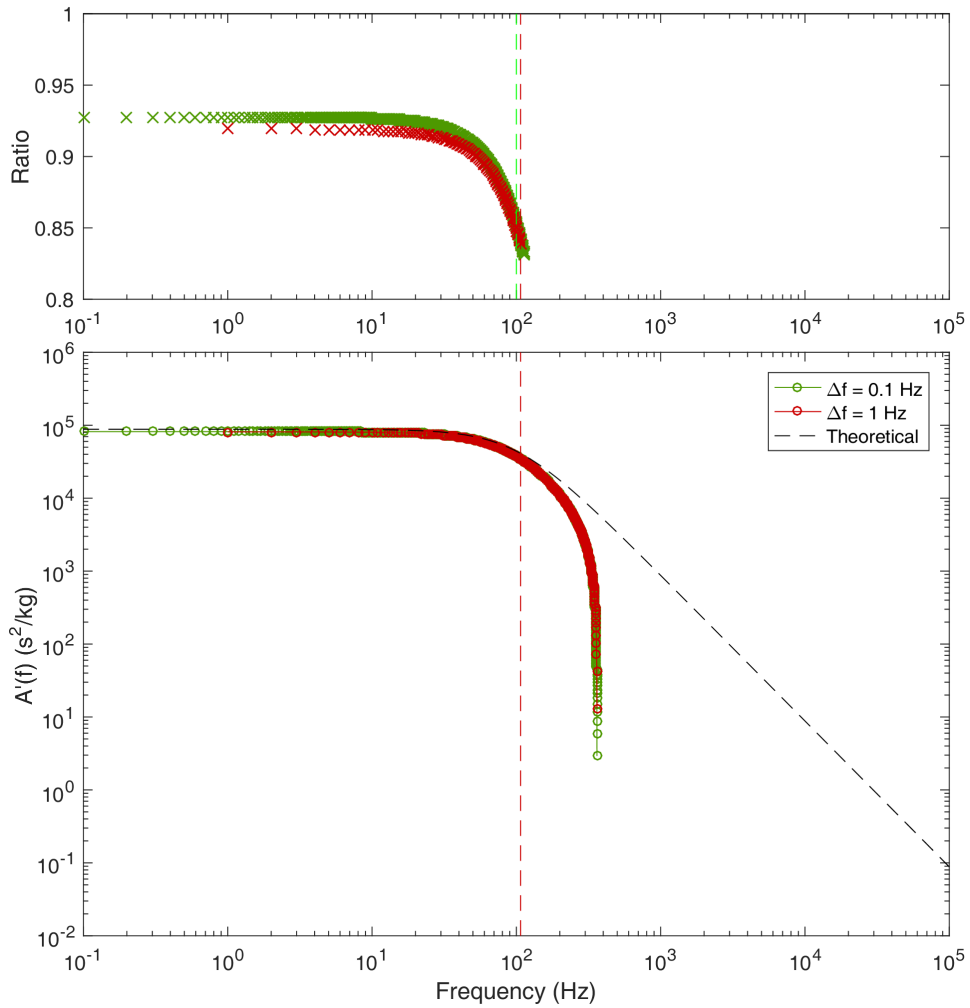


Figure 5.23: Changing the frequency step sizes of the camera-like  $A'(f)$ . The cut-off frequency (red dashed line) is 107 Hz for all curves, and the corner frequency (green dashed line) is 100 Hz. The ratio approaches to 1 at low frequencies with decreasing step size.

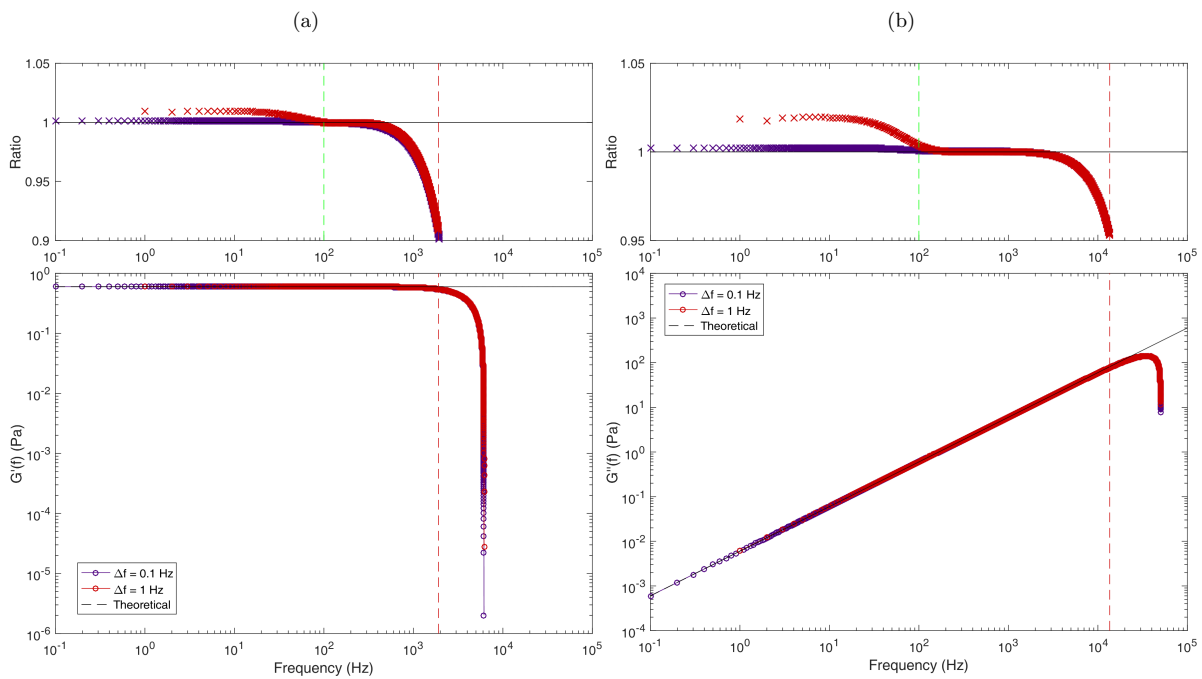


Figure 5.24: The QPD-like (a) elastic and (b) viscous shear moduli for  $\Delta f = 0.1$  Hz (navy) and  $\Delta f = 1$  Hz (red), and theoretical (black) dashed moduli with ratio plots. The green dashed lines show the corner frequency,  $f_c = 100$  Hz, and the cut-off frequencies are shown by red dashed lines.

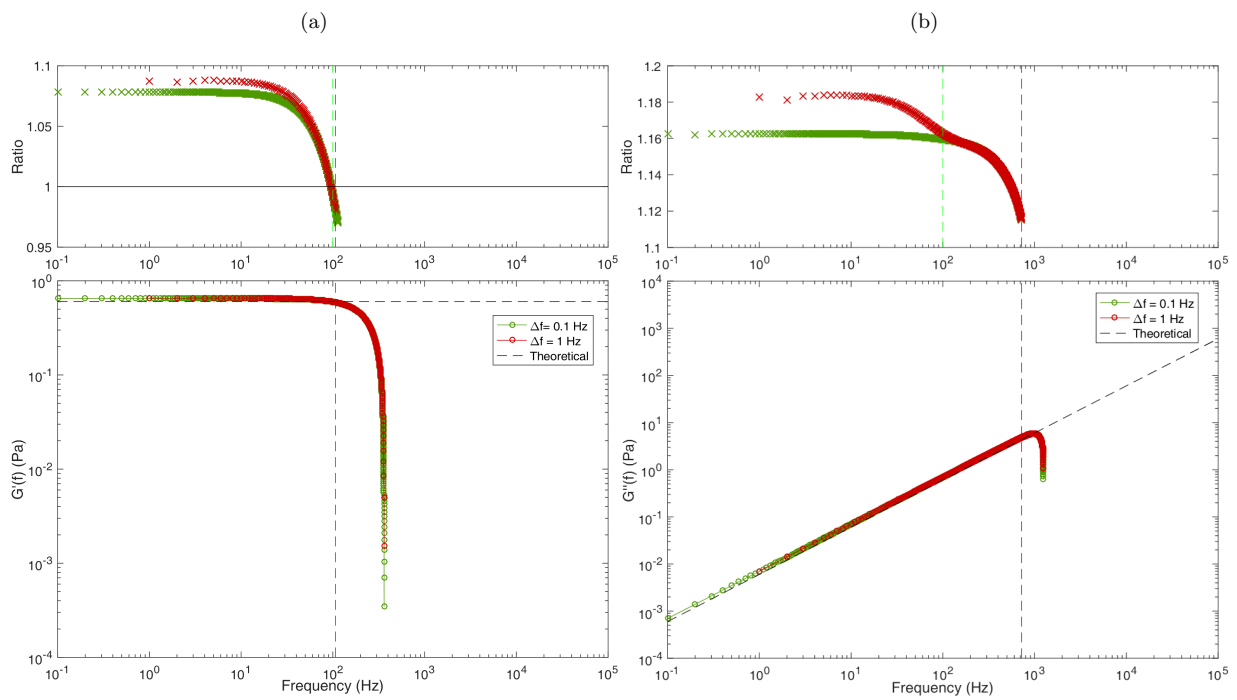


Figure 5.25: The camera-like (a) elastic and (b) viscous shear moduli for  $\Delta f = 0.1$  Hz (green) and  $\Delta f = 1$  Hz (red), and theoretical (black) data with ratio plots. The green dashed lines show the corner frequency,  $f_c = 100$  Hz, and the cut-off frequencies are shown by red dashed lines.

value. This results in an underestimation of the true integral value. The underestimation is particularly prevalent at the extrema, where the data above the Nyquist frequency and below  $f = \Delta f$ , the first frequency value, also cannot be included. In other words, the code tries to approximate

$$A' \approx \frac{2}{\pi} P \int_{\Delta f}^{f_{\text{Nyq}}} \frac{\xi A''(\xi)}{(\xi^2 - f^2)} d\xi \approx \frac{2}{\pi} \left[ \int_{\Delta f}^{(f-\Delta f)} \frac{\xi A''(\xi)}{(\xi^2 - f^2)} d\xi + \int_{(f+\Delta f)}^{f_{\text{Nyq}}} \frac{\xi A''(\xi)}{(\xi^2 - f^2)} d\xi \right], \quad (5.4)$$

using the trapezoidal approximation

$$\int_a^b f(x) dx \approx \frac{b-a}{2N} \sum_{n=1}^N (f(x_n) + f(x_{n+1})). \quad (5.5)$$

To take the principal value integral, the integral needs to be taken in the limit as  $\Delta f \rightarrow 0$  and  $f_{\text{Nyq}} \rightarrow \infty$ ; however, with discrete data, this is not possible. With smaller  $\Delta f$ , more of this integral is being included. Therefore, data with  $\Delta f = 1$  underestimates the true result of the integral more than a smaller  $\Delta f$ , where more of the integral is accounted for. This is the reason we see improved agreement with expected values at low frequencies with smaller  $\Delta f$  values. As shown in Section 5.2.2, the camera-like data never achieves a ratio as close to 1 as the QPD-like data due to the (necessary) inclusion of the effects of blur.

### 5.3 Achieving better estimates in experiment

Due to external sources of noise, such as thermal drift, obtaining data with smaller  $\Delta f$  (longer  $T_{msr}$ ) is not practical experimentally. However, similar improvements may nonetheless be possible to achieve by interpolating the PSD of  $\Delta f = 1$  Hz intervals, in order to produce more densely spaced frequency points between  $\Delta f$  and  $f_{\text{Nyq}}$ , producing a more correct results of the integration of Equation 5.4. In order to do this, points were linearly interpolated between each successive 1 Hz point starting at 1 Hz to produce a PSD with effective frequency spacing of  $\Delta f = 0.1$  Hz. As an example, I show, in Figure 5.26, a PSD of experimental data of a trapped bead in water, collected using the QPD.

Figure 5.27 shows the numerically represented complex shear modulus, with both QPD-like and camera-like data, corresponding to the experimental case in Figure 5.26, *i.e.*, for a  $1.445 \mu\text{m}$  radius bead in water at  $T = 22^\circ\text{C}$  with  $\Delta f = 1$  Hz. The conditions for the cut-off frequency for both  $G'(f)$  and  $G''(f)$  have been changed to 98% of the expected trend (as opposed to 90%, as described in Section 5.2). This change eliminates the excess higher frequency data that lead to an underestimation of  $\eta$  and  $G'_{\text{trap}}$  for QPD-like data.

The numerically calculated cut-off frequencies for the QPD-like case ( $f_{\text{cutoff}} = 1098$  Hz for  $G'(f)$  and  $f_{\text{cutoff}} = 6211$  Hz for  $G''(f)$ ) are used as limits to fit the experimental complex shear modulus. In other words,  $G'(f)$  is fit with a line of slope 0 from  $f = 1$  Hz to  $f_{\text{cutoff}} = 1098$  Hz, and  $G''(f)$  is fit with a line of slope 1 from  $f = 1$  Hz to  $f_{\text{cutoff}} = 6211$  Hz.

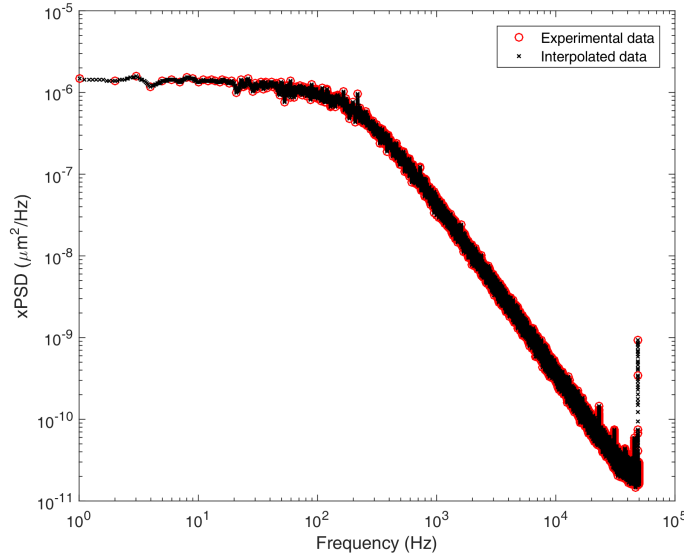


Figure 5.26: Experimental PSD for the positions of a bead in water (red) from the QPD with linearly interpolated points (black). Output parameters from fitting both experimental and interpolated data are  $D = 0.1551 \pm 0.0006 \mu\text{m}^2 \cdot \text{Hz}$  and  $f_c = 193 \pm 2 \text{ Hz}$ .

Figure 5.28 shows both interpolated and non-interpolated experimental complex shear moduli from the data in Figure 5.26. The difference between these is subtle. Note that the bin sizes are slightly different in the interpolated case, which accounts for the discrepancy along the x-axis. A large difference in complex shear modulus is not expected, based on previous improvements to  $A'(f)$  (1% at most; Section 5.2.3). Fits are not shown; their output values are reported in Table 5.1.

The same process is applied to the camera experimental data, with cut-off frequencies for  $G'(f)$  and  $G''(f)$  (66 Hz and 310 Hz, respectively) determined from the numerically calculated camera-like data. Figure 5.29 shows the interpolated and non-interpolated PSD from the camera for the same bead as in Figure 5.26. Figure 5.30 shows the complex shear modulus derived from this PSD. Again, the difference between interpolated and non-interpolated data is subtle, which is reflected in the difference in  $G'_{\text{trap}}$  and  $\eta$  reported in Table 5.1.

The values in Table 5.1 were extracted for one experimental trial. The interpolated data do provide values slightly closer to the expected values of  $G'_{\text{trap}}$ . However, the expected value is based on the mean bead size of  $R = 1.445 \mu\text{m}$ . Therefore, multiple experimental trials are necessary for better comparison with expected values and validation of this technique.

### 5.3.1 Interpolating data from a complex fluid

Interpolated data points can also be added to power spectra for complex fluids. Figures 5.31a and 5.31b show the PSDs for a bead in a 1 mg/mL collagen solution in 20mM acetic

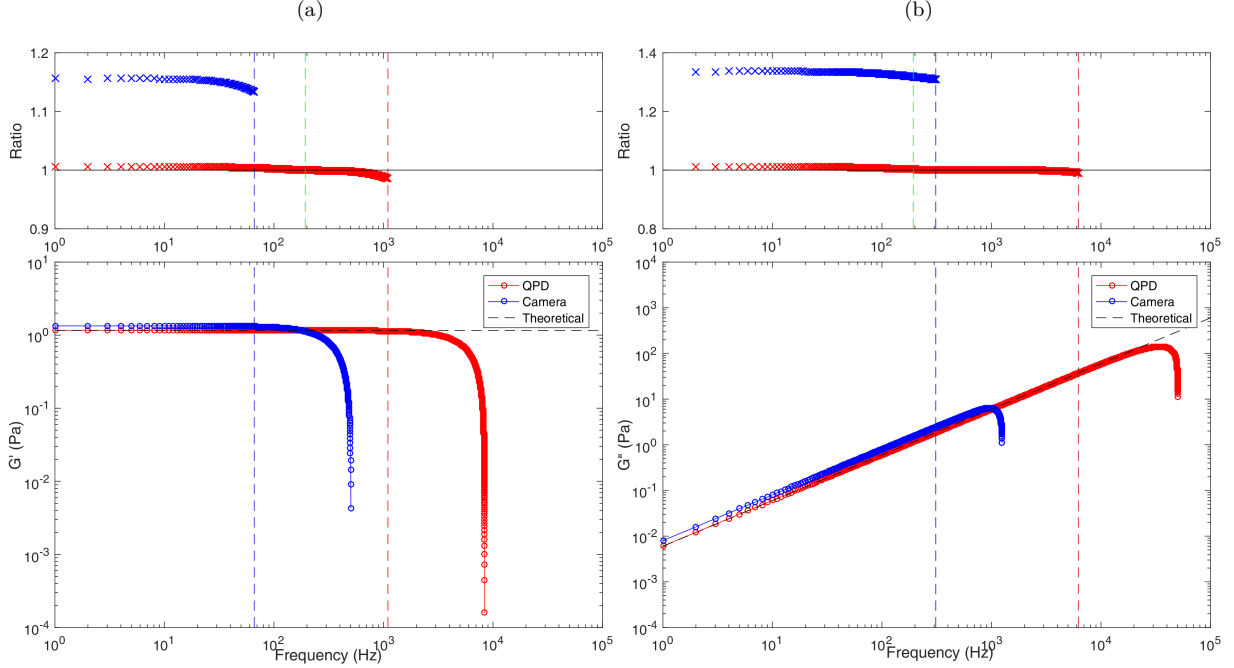


Figure 5.27: Calculated (a) elastic and (b) viscous moduli for the theoretical (black, dashed), QPD-like (red) and camera-like (blue) data, with ratio plots, for values corresponding to experimental data in Figure 5.26. Red and blue dashed lines show the cut-off frequencies for the QPD-like and camera-like data, respectively, and green dashed lines show the corner frequency, for reference.

	$G'_{\text{trap}_{\text{QPD}}}$ (Pa)	$G'_{\text{trap}_{\text{cam}}}$ (Pa)	$\eta_{\text{QPD}}$ (Pa · s)	$\eta_{\text{cam}}$ (Pa · s)
Theoretical expectation	1.158		$9.547 \times 10^{-4}$	
Numerical representation	1.153	1.329	$9.500 \times 10^{-4}$	$1.26 \times 10^{-3}$
Non-interpolated experiment	$1.10 \pm 0.04$	$2.264 \pm 0.004$	$(1.048 \pm 0.005) \times 10^{-3}$	$(2.11 \pm 0.02) \times 10^{-3}$
Interpolated experiment	$1.10 \pm 0.04$	$2.252 \pm 0.005$	$(1.021 \pm 0.006) \times 10^{-3}$	$(2.10 \pm 0.02) \times 10^{-3}$

Table 5.1: Complex shear modulus outputs from experiment and numerical representation. Interpolated data slightly improve the results.

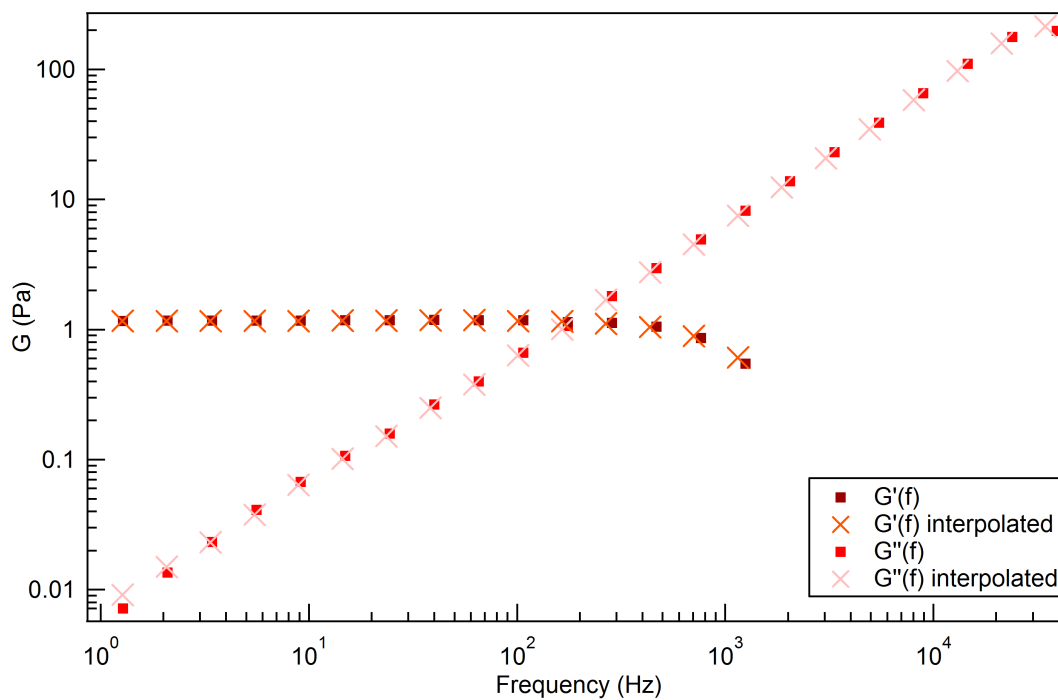


Figure 5.28: Interpolated (X's) and non-interpolated (squares) experimental  $G'(f)$  (dark red) and  $G''(f)$  (light red) from the QPD for a bead in water, averaged into logarithmically spaced blocks for clarity. The differences between interpolated and non-interpolated data are subtle.

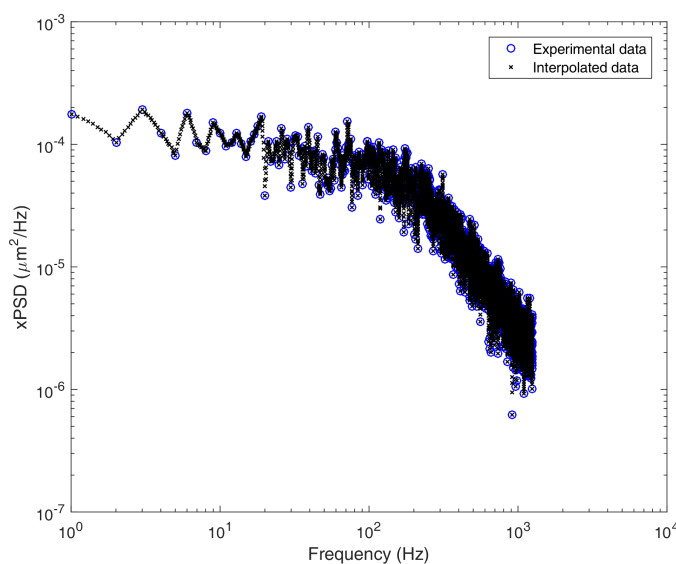


Figure 5.29: Experimental PSD data for the positions of a bead in water (blue) from the high-speed camera with linearly interpolated points (black).

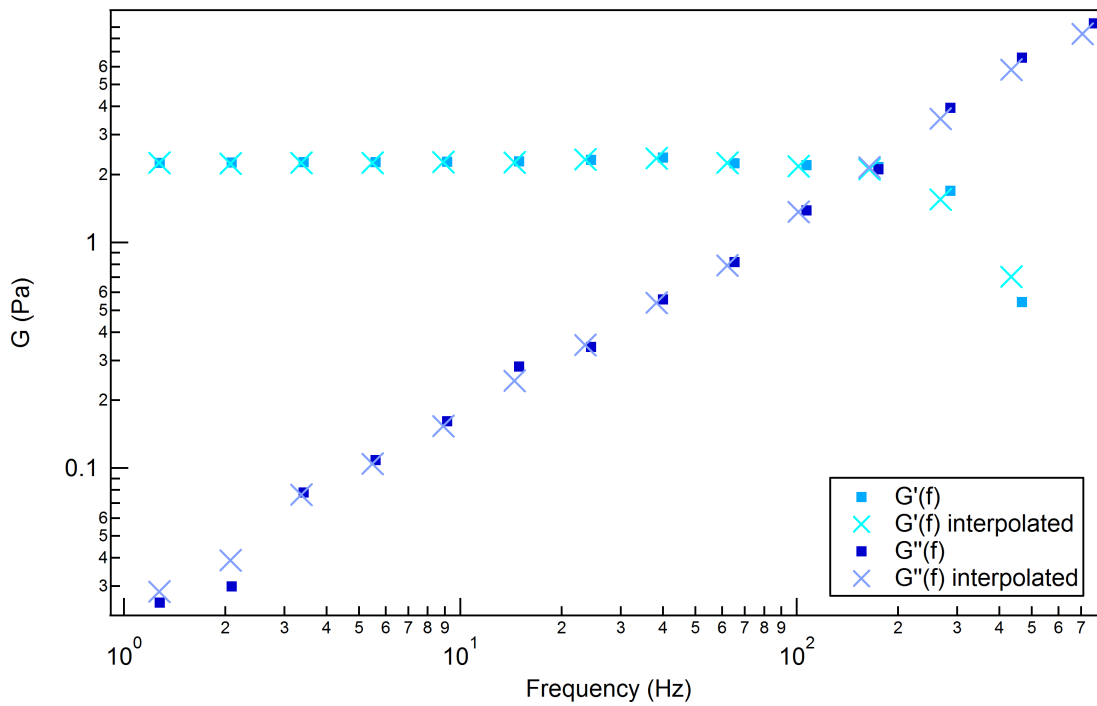


Figure 5.30: Interpolated (X's) and non-interpolated (squares) experimental  $G'(f)$  (light blue) and  $G''(f)$  (dark blue) from the high-speed camera for a bead in water, averaged into logarithmically spaced blocks for clarity. The difference between interpolated and non-interpolated data is apparent but small.

acid, obtained using the QPD and high-speed camera, respectively. The shape of these power spectra is different than those for water. This is due to the elasticity of the collagen solution. In water at low frequencies (over long times), the bead is only able to move according to the elasticity of the trap, whereas at high frequencies (over short times), it is able to diffuse freely. For a complex fluid such as collagen, the elasticity is present over the whole frequency range. In Figure 5.31, this is identifiable by the lack of plateau at low frequencies followed by a slope which is not characterized by diffusion only.

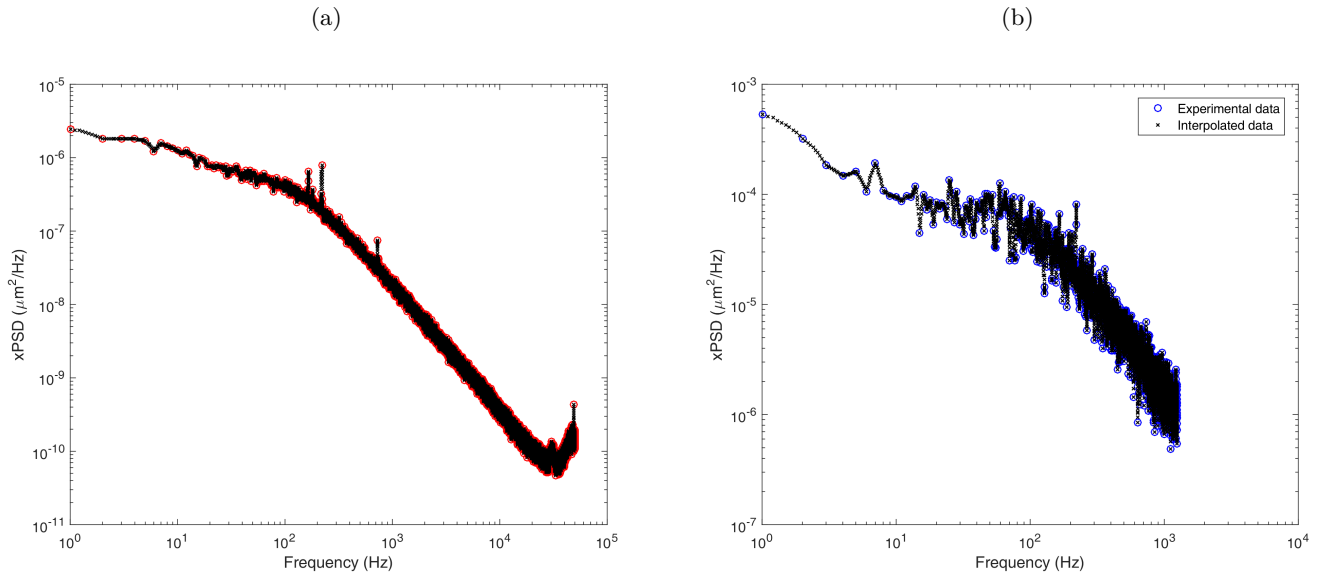


Figure 5.31: Experimental PSD data for a bead in collagen from the (a) QPD (red) and (b) camera (blue), both with interpolated points (black) along the linear line connecting each experimental point.

Figure 5.32 shows the resultant complex shear moduli for both interpolated and non-interpolated data, obtained from QPD measurements. The difference between collagen and water is particularly noticeable at high frequencies in  $G'(f)$ . While the low frequencies are dominated by the elasticity of the trap (in this case, slightly higher than in Figure 5.26), the high frequencies exhibit frequency-dependent elasticity. As with water, the difference between the interpolated and non-interpolated data in Figure 5.32 is subtle.

Figure 5.33 shows the complex moduli obtained using the high-speed camera, with both interpolated and non-interpolated data. In this case, the limited frame rate prohibits the higher frequency elastic behaviour of the collagen solution from becoming apparent. The difference between the interpolated and non-interpolated data is small.

Despite the only slight distinction between interpolated and non-interpolated data, this simple method allows for a more accurate representation of the results from microrheological experiments. As I have shown, the interpolation of power spectral density data can be

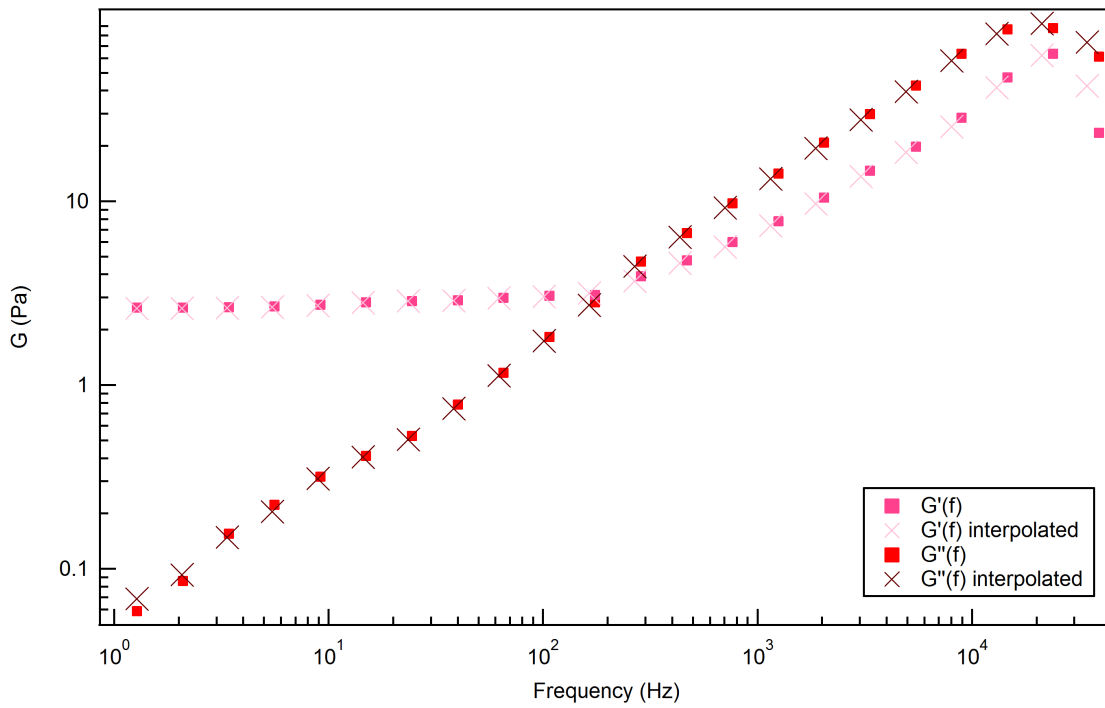


Figure 5.32: Interpolated (X's) and non-interpolated (squares) experimental  $G'(f)$  (light red) and  $G''(f)$  (dark red) from the QPD for a bead in collagen, averaged into logarithmically spaced blocks for clarity. The difference between interpolated and non-interpolated data is apparent but small.

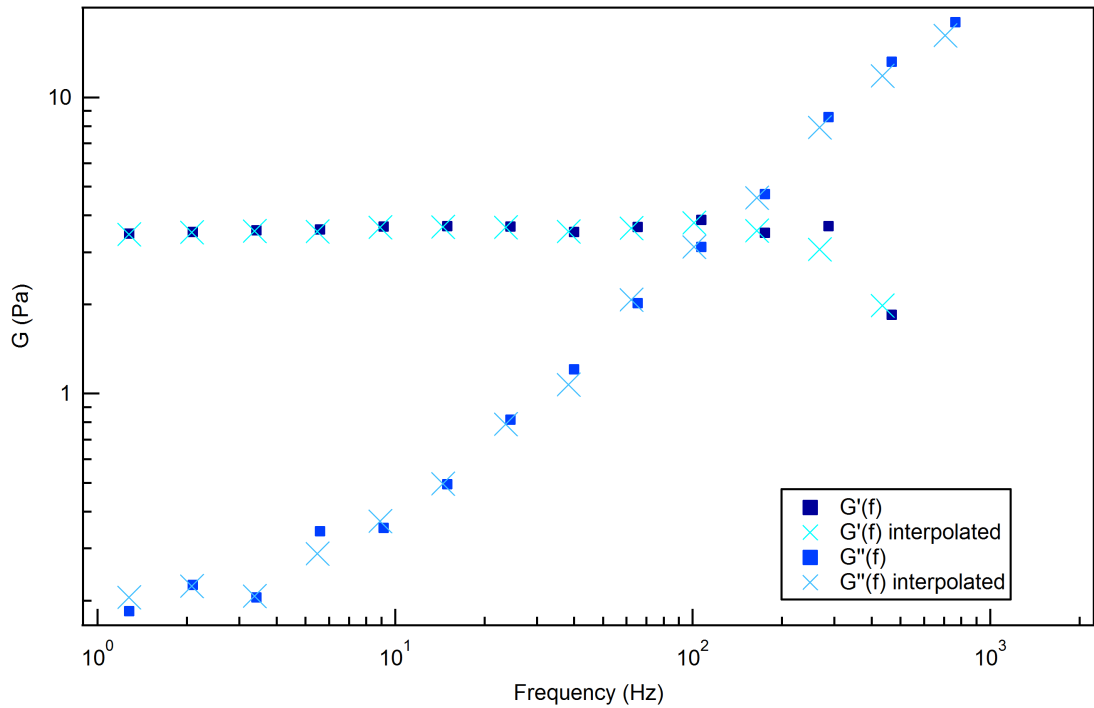


Figure 5.33: Interpolated (X's) and non-interpolated (squares) experimental  $G'(f)$  (light blue) and  $G''(f)$  (dark blue) from the high-speed camera for a bead in collagen, averaged into logarithmically spaced blocks for clarity. The difference between interpolated and non-interpolated data is apparent but small.

applied successfully to non-Newtonian and Newtonian fluids alike, obtained using either a QPD or a camera.

## Chapter 6

# Conclusions and Future Directions

In this thesis, I used a high-speed camera as a method of particle detection in the optical tweezers set-up for use in microrheological experiments. The high-speed camera will be necessary for holographic optical tweezers, which pattern the laser beam into multiple, independent traps, to measure the motions of multiple particles simultaneously. The eventual goal of implementing the high-speed camera is to characterize the motion and local viscoelastic environment of multiple particles trapped at desired locations within a collagen gel.

Previous studies [13, 14, 15] found that the viscoelastic properties of collagen gels vary at different locations within the gel, during assembly and afterwards. Understanding the cross-correlation between developing viscoelasticity at different locations within an assembling gel will provide improved comprehension of the self-assembly process, which affects many physiological processes [5, 6], and may lead to better design of tissue engineering applications [10] and substrates for studies in cellular engineering [8, 9].

The first step of introducing the holographic optical tweezers is using the high-speed camera to analyse the positions of the bead in the trap. In Chapter 4, I determined the power spectra of beads' motion in water using the camera and found that these did not agree with data from the QPD, which detects the positions via the deflection of the laser by the bead. The QPD method cannot be used for the holographic optical tweezers set-up because it cannot detect the independent motion of more than one bead simultaneously.

Due to the very limited sampling frequency ( $f_s = 2500$  fps), the effects of aliasing, blur, and detection error are much more important in the camera PSD than in the QPD's. Despite taking these into account in the fit function of the camera's power spectra, the output diffusion constant is consistently lower than that from the QPD, which results in overestimates of sample viscosity and elasticity.

There is significant spread in both QPD- and camera-derived diffusion constants. The QPD-derived diffusion constant overestimates the expected value from the Stokes-Einstein

relation, while the camera-derived diffusion constant underestimates it. The cause of the overestimated QPD-derived diffusion constant was not investigated.

The corner frequency, the frequency at which the bead begins to feel the constraints of the trap, consistently scales with laser power, which is directly proportional to the stiffness of the trap. The diffusion constants, which are expected to be independent of laser power, are scattered and show no systematic trend with laser power.

Avoiding the complications of the camera by fitting a flat line to  $PSD \times f^2$  results in a slightly higher diffusion constant than fitting to the PSD directly. For future studies, it is recommended that this method be used for the most accurate results. Unfortunately, this method did not resolve the discrepancy between the diffusion constants from the QPD and camera.

I replaced the QPD with a position-sensitive diode (PSD\*). This detector also measures the deflection of the laser beam and would not be appropriate for the holographic optical tweezers, but useful for verifying the results from the QPD. The diffusion constant from the PSD\* is larger than that from the camera and appears similar to that from the QPD. While the PSD\* was connected, I also examined the effects on the bead's power spectrum due to a nearby surface (*i.e.*, the microscope slide) and found that in the typical trapping region, the power spectrum should not be affected by surface interactions.

In order to investigate the discrepancy between the results from the camera and QPD further, I went directly to its source: a difference in the measured value of the bead's variance. The variance as seen by the camera is smaller than that seen by the QPD. Indeed, the areas under the PSDs confirm this. While this difference doesn't appear to affect the calibration of the QPD's position (which uses positions from the camera), future studies would do well to examine other possibilities of calibrating the QPD, such as using a piezoelectric stage.

Because of the integration time of the camera, the time over which an image is averaged while the shutter is open, the variance of particles as measured by the camera is not expected to be the same as that of the QPD. Therefore, I down-sampled the QPD data by averaging multiple position readings to mimic the effect of camera blur. The results indicate that the down-sampled QPD data follow the theoretically expected trend, but the camera data, using multiple different integration times, do not. The measured variance of the particle decreased as the integration time decreased as well as for manually decreased illumination, which indicates an issue with the analysis program. Future work should compare these results with alternative bead position detection algorithms, to determine how best to determine the variance of the trapped particle's position, as measured with a high-speed camera intensities.

In Chapter 5, I numerically represented the expected output from the optical tweezers-based microrheology experiments in water for the QPD and camera, and compared these to the theoretically expected output.

The camera and the QPD have finite sampling frequencies, which leads to a cut-off in the integration which calculates the real response function ( $A'(f)$ ). As a result, this and the complex shear modulus drop off at the highest frequencies. The location of this drop-off is dependent on the sampling frequency, which is smaller for the camera than for the QPD.

The rationale for numerically representing this data was to determine an appropriate drop-off frequency after which the data could no longer be included to produce the correct value. I defined a cut-off frequency as the frequency at which the numerical data fell off the expected trend by 10%. On logarithmic scales, the expected trend of  $G'(f)$  is a flat line with height related to the corner frequency, and for  $G''(f)$ , the expected trend is a linear line with slope 1 and intercept  $\log(2\pi\eta)$ .

Surprisingly, I found that the QPD underestimates the output viscosity and the camera overestimates it, using a fit from  $f = 1$  Hz to the cut-off frequency. The ratios of the QPD-like data to the theoretical data reveal that there is a discrepancy also at low frequencies. This was consistent across many different numerical calculations while independently changing the corner frequency and sampling frequency.

By changing the corner frequency, I showed that the trap stiffness affects the cut-off frequency and therefore also the output viscosity and plateau of  $G'$ . An increase in corner frequency led to an increase in viscosity for both the QPD- and camera-like data. Since the QPD-like data underestimates the viscosity, future experiments using the QPD are advised to use a high corner frequency. Contrarily, experiments using the high-speed camera, *i.e.*, future experiments using the holographic optical tweezers, should use a low corner frequency to minimize the overestimation of the viscosity. Similarly, for  $G'_{\text{trap}}$ , at high corner frequencies, the camera-like data overestimates more dramatically, thus a lower corner frequency would be desirable.

An increase in the sampling frequency of the QPD-like data increases the range over which the data exhibits the expected trend (increases the cut-off frequency) but did not affect the discrepancy at low frequencies.

Decreasing the sampling frequency of the QPD-like data to the camera's frame rate ( $f_s = 2500$  s) revealed that the blur, included in the camera data's calculation but not in the QPD's, greatly affects the viscosity and  $G'_{\text{trap}}$  outputs.

To understand the low frequency discrepancies, I decreased the frequency step size between each consecutive point ( $\Delta f$ ). I found that the smaller the  $\Delta f$ , the closer the ratio of device-like to theoretical data was to 1 at low frequencies, for both camera- and QPD-like data. This was due to the method used for integration, which provides a better estimate of the true integral value for  $\Delta f \rightarrow 0$ .

Experimentally, obtaining data with smaller  $\Delta f$  (longer measurement time) is impractical, therefore, to get better results, I linearly interpolated experimental data from the QPD and camera from one trial at 0.1 Hz intervals. This resulted in very modest changes to the viscosity and  $G'_{\text{trap}}$  results.

Finally, I showed that interpolation can also be successfully implemented for a complex fluid by showing the complex shear modulus of a bead in a collagen solution. Again, the difference between the interpolated and non-interpolated data is small, but I recommend using this simple method in future experiments to improve their accuracy.

# Bibliography

- [1] M. J. Buehler, “Nature designs tough collagen: explaining the nanostructure of collagen fibrils.” *Proceedings of the National Academy of Sciences of the United States of America* **103**, 12 285–12 290 (2006).
- [2] P. Fratzl, *Collagen: Structure and Mechanics, an Introduction* (Springer US, Boston, MA, 2008), pp. 1–13.
- [3] F. Grinnell and W. M. Petroll, “Cell motility and mechanics in three-dimensional collagen matrices.” *Annual Review of Cell and Developmental Biology* **26**, 335–361 (2010).
- [4] S. Rhee and F. Grinnell, “Fibroblast mechanics in 3D collagen matrices,” *Advanced Drug Delivery Reviews* **59**, 1299–1305 (2007).
- [5] A. Pathak and S. Kumar, “Biophysical regulation of tumor cell invasion: moving beyond matrix stiffness,” *Integrative Biology* **3**, 267–278 (2011).
- [6] D. W. Friedman, C. D. Boyd, J. W. Mackenzie, P. Norton, R. M. Olson, and S. B. Deak, “Regulation of collagen gene expression in keloids and hypertrophic scars.” *Journal of Surgical Research* **55**, 214–222 (1993).
- [7] N. Huebsch, P. R. Arany, A. S. Mao, D. Shvartsman, O. A. Ali, S. A. Bencherif, J. Rivera-Feliciano, and D. J. Mooney, “Harnessing traction-mediated manipulation of the cell/matrix interface to control stem-cell fate.” *Nature Materials* **9**, 518–26 (2010).
- [8] D. E. Discher, P. Janmey, and Y.-L. Wang, “Tissue cells feel and respond to the stiffness of their substrate.” *Science* **310**, 1139–43 (2005).
- [9] P. A. Janmey and D. A. Weitz, “Dealing with mechanics: Mechanisms of force transduction in cells,” *Trends in Biochemical Sciences* **29**, 364–370 (2004).
- [10] T. Dvir, B. P. Timko, D. S. Kohane, and R. Langer, “Nanotechnological strategies for engineering complex tissues.” *Nature Nanotechnology* **6**, 13–22 (2011).
- [11] A. P. Hollander, I. Pidoux, A. Reiner, C. Rorabeck, R. Bourne, and A. R. Poole, “Damage to type II collagen in aging and osteoarthritis starts at the articular surface, originates around chondrocytes, and extends into the cartilage with progressive degeneration,” *Journal of Clinical Investigation* **96**, 2859–2869 (1995).
- [12] A. Stacey, J. Bateman, T. Choi, T. Mascara, W. Cole, and R. Jaenisch, “Perinatal lethal osteogenesis imperfecta in transgenic mice bearing an engineered mutant pro- $\alpha$  (I) collagen gene,” *Nature* **332**, 131–136 (1988).

- [13] M. Shayegan and N. R. Forde, “Microrheological characterization of collagen systems: from molecular solutions to fibrillar gels,” *PLoS ONE* **8**, 23–28 (2013).
- [14] Y. L. Yang and L. J. Kaufman, “Rheology and confocal reflectance microscopy as probes of mechanical properties and structure during collagen and collagen/hyaluronan self-assembly,” *Biophysical Journal* **96**, 1566–1585 (2009).
- [15] O. Latinovic, L. A. Hough, and H. Daniel Ou-Yang, “Structural and micromechanical characterization of type I collagen gels,” *Journal of Biomechanics* **43**, 500–505 (2010).
- [16] A. van der Horst and N. R. Forde, “Calibration of dynamic holographic optical tweezers for force measurements on biomaterials,” *Optics Express* **16**, 20 987 (2008).
- [17] A. van der Horst and N. R. Forde, “Power spectral analysis for optical trap stiffness calibration from high-speed camera position detection with limited bandwidth.” *Optics Express* **18**, 7670–7677 (2010).
- [18] M. Atakhorrami, J. I. Sulkowska, K. M. Addas, G. H. Koenderink, J. X. Tang, A. J. Levine, F. C. MacKintosh, and C. F. Schmidt, “Correlated fluctuations of microparticles in viscoelastic solutions: Quantitative measurement of material properties by microrheology in the presence of optical traps,” *Physical Review E* **73**, 1–12 (2006).
- [19] J. D. Ferry, *Viscoelastic Properties of Polymers* (John Wiley & Sons, Inc., 1970), 2 edn.
- [20] M. Reiner, “The Deborah Number,” *Physics Today* **17**, 62 (1964).
- [21] M. Clagett, *Ancient Egyptian science: calendars, clocks, and astronomy* (American Philosophical Society, Philadelphia, 1995), 2 edn.
- [22] S. I. Newton and N. W. Chittenden, *Newton’s Principia: The Mathematical Principles of Natural Philosophy: by Sir Isaac Newton; Translated into English by Andrew Motte; to Which Is Added Newton’s System of the World; with a Portrait Taken from the Bust in the Royal Observatory at Greenwich.* (Daniel Adee, New York, 1846).
- [23] J. Chen and J. R. Stokes, “Rheology and tribology: Two distinctive regimes of food texture sensation,” *Trends in Food Science and Technology* **25**, 4–12 (2012).
- [24] G. Tabilo-Munizaga and G. V. Barbosa-Cánovas, “Rheology for the food industry,” *Journal of Food Engineering* **67**, 147–156 (2005).
- [25] J. R. Dorgan, H. Lehermeier, and M. Mang, “Thermal and rheological properties of commercial-grade poly (lactic acid)s,” *Journal of Polymers and the Environment* **8**, 1–9 (2000).
- [26] Y. Lu, D. Elsworth, and L. Wang, “A dual-scale approach to model time-dependent deformation, creep and fracturing of brittle rocks,” *Computers and Geotechnics* **60**, 61–76 (2014).
- [27] D. Or and T. A. Ghezzehei, “Modeling post-tillage soil structural dynamics: A review,” *Soil and Tillage Research* **64**, 41–59 (2002).

- [28] M. Pastor, T. Blanc, B. Haddad, V. Drempevic, M. S. Morles, P. Dutto, M. M. Stickle, P. Mira, and J. A. F. Merodo, “Depth averaged models for fast landslide propagation: mathematical, rheological and numerical aspects,” *Archives of Computational Methods in Engineering* **22**, 67–104 (2015).
- [29] B. D. Hoffman and J. C. Crocker, “Cell mechanics: dissecting the physical responses of cells to force.” *Annual Review of Biomedical Engineering* **11**, 259–288 (2009).
- [30] P. A. Janmey, “The cytoskeleton and cell signaling: component localization and mechanical coupling.” *Physiological Reviews* **78**, 763–81 (1998).
- [31] W. W. Graessley, *Polymeric Liquids and Networks: Dynamics and Rheology* (Taylor & Francis Group, LLC, New York, 2008).
- [32] T. A. Waigh, “Microrheology of complex fluids,” *Reports on Progress in Physics* **68**, 685–742 (2005).
- [33] F. A. Morrison, *Understanding Rheology* (Oxford University Press, Oxford, 2001).
- [34] I. Y. Wong, M. L. Gardel, D. R. Reichman, E. R. Weeks, M. T. Valentine, A. R. Bausch, and D. A. Weitz, “Anomalous diffusion probes microstructure dynamics of entangled F-actin networks,” *Physical Review Letters* **92**, 178 101–1 (2004).
- [35] T. G. Mason, H. Gang, and D. A. Weitz, “Diffusing-wave-spectroscopy measurements of viscoelasticity of complex fluids,” *Journal of the Optical Society of America* **14**, 139 (1997).
- [36] R. E. Mahaffy, C. K. Shih, F. C. MacKintosh, and J. Käs, “Scanning probe-based frequency-dependent microrheology of polymer gels and biological cells,” *Physical Review Letters* **85**, 880–883 (2000).
- [37] A. R. Bausch, W. Möller, and E. Sackmann, “Measurement of local viscoelasticity and forces in living cells by magnetic tweezers.” *Biophysical Journal* **76**, 573–579 (1999).
- [38] T. G. Mason, K. Ganesan, J. van Zanten, D. Wirtz, and S. Kuo, “Particle Tracking Microrheology of Complex Fluids,” *Physical Review Letters* **79**, 3282–3285 (1997).
- [39] R. R. Brau, J. M. Ferrer, H. Lee, C. E. Castro, B. K. Tam, P. B. Tarsa, P. Matsudaira, M. C. Boyce, R. D. Kamm, and M. J. Lang, “Passive and active microrheology with optical tweezers,” *Journal of Optics A: Pure and Applied Optics* **9**, S103–S112 (2007).
- [40] D. Mizuno, D. A. Head, F. C. MacKintosh, and C. F. Schmidt, “Active and Passive Microrheology in Equilibrium and Nonequilibrium Systems,” *Macromolecules* **41**, 7194–7202 (2008).
- [41] K. C. Neuman and S. M. Block, “Optical trapping,” *Review of Scientific Instruments* **75**, 2787–2809 (2004).
- [42] K. Berg-Sørensen and H. Flyvbjerg, “Power spectrum analysis for optical tweezers,” *Review of Scientific Instruments* **75**, 594–612 (2004).
- [43] A. Yao, M. Tassieri, M. Padgett, and J. Cooper, “Microrheology with optical tweezers.” *Lab on a Chip* **9**, 2568–2575 (2009).

- [44] K. M. Addas, C. F. Schmidt, and J. X. Tang, “Microrheology of solutions of semiflexible biopolymer filaments using laser tweezers interferometry,” *Physical Review E* **70**, 1–16 (2004).
- [45] M. Shayegan, *Determining local viscoelastic properties of collagen systems using optical tweezers*, Ph.D. thesis, Simon Fraser University (2014).
- [46] W. W. Graessley, *Polymeric Liquids and Networks: Structure and Properties* (Taylor & Francis Group, LLC, New York, 2003).
- [47] B. R. Dasgupta, S. Y. Tee, J. C. Crocker, B. J. Frisken, and D. A. Weitz, “Microrheology of polyethylene oxide using diffusing wave spectroscopy and single scattering,” *Physical Review E* **65**, 51 505 (2002).
- [48] J. R. Moffitt, Y. R. Chemla, S. B. Smith, and C. Bustamante, “Recent advances in optical tweezers,” *Annual Review of Biochemistry* **77**, 205–228 (2008).
- [49] A. Ashkin, “Acceleration and Trapping of Particles by Radiation Pressure,” *Physical Review Letters* **24**, 156–159 (1970).
- [50] A. Ashkin, J. M. Dziedzic, J. E. Bjorkholm, and S. Chu, “Observation of a single-beam gradient force optical trap for dielectric particles,” *Optics Letters* **11**, 288 (1986).
- [51] S. C. Chapin, V. Germain, and E. R. Dufresne, “Automated trapping, assembly, and sorting with holographic optical tweezers.” *Optics Express* **14**, 13 095–13 100 (2006).
- [52] M. P. MacDonald, G. C. Spalding, and K. Dholakia, “Microfluidic sorting in an optical lattice,” *Nature* **426**, 421–424 (2003).
- [53] P. J. Reece, W. J. Toe, F. Wang, S. Paiman, Q. Gao, H. H. Tan, and C. Jagadish, “Characterization of semiconductor nanowires using optical tweezers,” *Nano Letters* **11**, 2375–2381 (2011).
- [54] T. Yu, F.-C. Cheong, and C.-H. Sow, “The manipulation and assembly of CuO nanorods with line optical tweezers,” *Nanotechnology* **15**, 1732–1736 (2004).
- [55] D. G. Grier, “Optical tweezers in colloid and interface science,” *Current Opinion in Colloid & Interface Science* **2**, 264–270 (1997).
- [56] J. Liphardt, S. Dumont, S. B. Smith, I. T. Jr., and C. Bustamante, “Equilibrium Information from Nonequilibrium Measurements in an Experimental Test of Jarzynski’s Equality,” *Science* **296**, 1832–1835 (2002).
- [57] E. H. Trepagnier, C. Jarzynski, F. Ritort, G. E. Crooks, C. J. Bustamante, and J. Liphardt, “Experimental test of Hatano and Sasa’s nonequilibrium steady-state equality,” *Proceedings of the National Academy of Sciences of the United States of America* **101**, 15 038–15 041 (2004).
- [58] G. M. Wang, E. M. Sevick, E. Mittag, D. Searles, and D. Evans, “Experimental Demonstration of Violations of the Second Law of Thermodynamics for Small Systems and Short Time Scales,” *Physical Review Letters* **89**, 50 601–50 604 (2002).

- [59] R. M. Berry and H. C. Berg, “Absence of a barrier to backwards rotation of the bacterial flagellar motor demonstrated with optical tweezers.” *Proceedings of the National Academy of Sciences of the United States of America* **94**, 14 433–14 437 (1997).
- [60] S. M. Block, D. F. Blair, and H. C. Berg, “Compliance of bacterial flagella measured with optical tweezers,” *Nature* **338**, 514–517 (1989).
- [61] S. M. Block, L. S. Goldstein, and B. J. Schnapp, “Bead movement by single kinesin molecules studied with optical tweezers.” (1990).
- [62] S. C. Kuo and M. P. Sheetz, “Force of single kinesin molecules measured with optical tweezers,” *Science* **260**, 232–234 (1993).
- [63] D. Mehta, M. Rief, J. Spudich, D. Smith, and R. M. Simmons, “Single-molecule biomechanics with optical methods.” *Science* **283**, 1689–1695 (1999).
- [64] U. Bockelmann, P. Thomen, B. Essevaz-Roulet, V. Viasnoff, and F. Heslot, “Unzipping DNA with optical tweezers: high sequence sensitivity and force flips.” *Biophysical Journal* **82**, 1537–1553 (2002).
- [65] T. T. Perkins, S. R. Quake, D. E. Smith, and S. Chu, “Relaxation of a single DNA molecule observed by optical microscopy.” *Science* **264**, 822–826 (1994).
- [66] M. D. Wang, H. Yin, R. Landick, J. Gelles, and S. M. Block, “Stretching DNA with optical tweezers.” *Biophysical Journal* **72**, 1335–46 (1997).
- [67] C. Hawes, A. Osterrieder, I. A. Sparkes, and T. Ketelaar, “Optical tweezers for the micromanipulation of plant cytoplasm and organelles,” *Current Opinion in Plant Biology* **13**, 731–735 (2010).
- [68] H. Maruyama, K. Kotani, T. Masuda, A. Honda, T. Takahata, and F. Arai, “Nanomanipulation of single influenza virus using dielectrophoretic concentration and optical tweezers for single virus infection to a specific cell on a microfluidic chip,” *Microfluidics and Nanofluidics* **10**, 1109–1117 (2011).
- [69] H. Zhang and K.-K. Liu, “Optical tweezers for single cells.” *Journal of the Royal Society* **5**, 671–690 (2008).
- [70] E. R. Dufresne and D. G. Grier, “Optical tweezer arrays and optical substrates created with diffractive optics,” *Review of Scientific Instruments* **69**, 1974 (1998).
- [71] M. Reichert, T. Haist, E. U. Wagemann, and H. J. Tiziani, “Optical particle trapping with computer-generated holograms written on a liquid-crystal display,” *Optics Letters* **24**, 608 (1999).
- [72] D. Bonessi, K. Bonin, and T. Walker, “Optical forces on particles of arbitrary shape and size,” *Journal of Optics A: Pure and Applied Optics* **9**, S228–S234 (2007).
- [73] E. Almaas and I. Brevik, “Radiation forces on a micrometer-sized sphere in an evanescent field.” *Journal of the Optical Society of America B* **12**, 2429 (1995).

- [74] R. Di Leonardo, J. Leach, H. Mushfique, J. M. Cooper, G. Ruocco, and M. J. Padgett, “Multipoint holographic optical velocimetry in microfluidic systems,” *Physical Review Letters* **96**, 7–10 (2006).
- [75] S. F. Nørrelykke and H. Flyvbjerg, “Harmonic oscillator in heat bath: Exact simulation of time-lapse-recorded data and exact analytical benchmark statistics,” *Physical Review E* **83**, 1–10 (2011).
- [76] W. P. Wong and K. Halvorsen, “The effect of integration time on fluctuation measurements: calibrating an optical trap in the presence of motion blur,” *Optics Express* **14**, 12 517–31 (2006).
- [77] G. M. Gibson, J. Leach, S. Keen, A. J. Wright, and M. J. Padgett, “Measuring the accuracy of particle position and force in optical tweezers using high-speed video microscopy.” *Optics Express* **16**, 14 561–14 570 (2008).
- [78] A. J. Makynen, J. T. Kostamovaara, and R. A. Myllyla, “Position Sensitive Detection Techniques for Manufacturing Accuracy,” in *SPIE Proceedings*, D. J. Svetkoff, ed., **1194**, 243–252 (1990).
- [79] J. Happel and H. Brenner, *Low Reynolds Number Hydrodynamics* (Springer Netherlands, 1983), pp. 23–57.
- [80] E. Schäffer, S. F. Nørrelykke, and J. Howard, “Surface forces and drag coefficients of microspheres near a plane surface measured with optical tweezers,” *Langmuir* **23**, 3654–3665 (2007).
- [81] E. J. G. Peterman, F. Gittes, and C. F. Schmidt, “Laser-induced heating in optical traps.” *Biophysical Journal* **84**, 1308–16 (2003).
- [82] J. Kestin, M. Sokolov, and W. A. Wakeham, “Viscosity of liquid water in the range -8 C to 150 C,” *Journal of Physical and Chemical Reference Data* **7**, 941–948 (1978).
- [83] J. Swindells, J. Coe, and T. Godfrey, “Absolute viscosity of water at 20-degrees-C,” *Journal of Research of the National Bureau of Standards* **48**, 1 (1952).
- [84] R. S. Marvin, “The accuracy of measurements of viscosity of liquids,” *Journal of Research at the National Bureau of Standards, Section A: Physics and Chemistry* **75**, 535–540 (1971).
- [85] A. Nagashima, “Viscosity of water substance-New international Formulation and its background,” *Journal of Physical and Chemical Reference Data* **6**, 1133–1166 (1977).
- [86] K. Ohta and H. Ishida, “Comparison among several numerical integration methods for Kramers-Kronig transformation,” *Applied Spectroscopy* **42**, 952–957 (1988).

# Appendix A

## Mathematical model Matlab code

```
for fc = 100:50:100

    df = 1; %frequency interval spacing

    %defining some constants/variable values
    kB = 1.3806*1e-23; %boltzmann constant, standard units
    temp2 = 295-273.15;%temp unit Celsius for calculation of eta
    temp = 295; %temperature, unit K
    R = (1)*1e-6; %radius of bead, unit m
    eta = (0.0010020)*10^(((20-(temp2))/(96+(temp2)))*((1.2364)-(1.37*10^(-3)
        *(20-(temp2)))+(5.7*10^(-6)*(20-(temp2))^2)));
    RQ = R;
    RC = R;

    D = kB*temp/(6*pi*eta*R); %Diffusion constant for theoretical case, units m^2*Hz
    DQ = kB*temp/(6*pi*eta*RQ); %Diffusion constant for QPD
    DC = kB*temp/(6*pi*eta*RC); %Diffusion constant for camera

    fcQ = fc; %and the corner frequency of the PSD, units Hz
    fcC = fc; %same for theoretical, QPD and camera data

    freqQ = linspace(df,50000,1/df*50000); %frequency range for the QPD fnyq=50000
    freqQ2 = linspace(df,100000,1/df*100000); %theoretical frequency range to "inf"
    freqC = linspace(df,1250,1/df*1250); %frequency range for the camera fnyq=1250

    dfQ = freqQ(size(freqQ,2))/(size(freqQ,2)-1); %defining the df of QPD
    dfC = freqC(size(freqC,2))/(size(freqC,2)-1); %defining the df of camera

    fnyqQ = freqQ(size(freqQ,2)); %nyquist frequency is half the sampling frequency
    fnyqC = freqC(size(freqC,2)); %for use in aliasing

    lorentzianQ = (DQ/pi^2)./((fcQ^2)+(freqQ.^2))+(DQ/pi^2)./((fcQ^2)+((2*fnyqQ-freqQ).^2))
        +(DQ/pi^2)./((fcQ^2)+((2*fnyqQ+freqQ).^2))+(DQ/pi^2)./((fcQ^2)+((4*fnyqQ-freqQ).^2))
```

```

+(DQ/pi^2)./((fcQ^2)+((4*fnyqQ+freqQ).^2));

%calculating the PSD for QPD, units m^2/Hz including aliasing

W = 1/(2*size(freqC,2));
%W is the exposure time of the camera. Typically this is not exactly 1/sampling
%frequency but for this purpose, it is ok.

lorentzianC = (DC/pi^2)./(fcC.^2+freqC.^2).*(sin(W.*pi.*freqC)./(W.*pi.*freqC)).^2
+(DC./(fcC.^2+(2*fnyqC-freqC).^2)).*(sin(W.*pi.*(2*fnyqC-freqC))
./(W*2*pi.*(2*fnyqC-freqC))).^2+(DC./(fcC.^2+(2*fnyqC+freqC).^2))
.*(sin(W*2*pi.*(2*fnyqC+freqC))./(W*2*pi.*(2*fnyqC+freqC))).^2
+(DC./(fcC.^2+(4*fnyqC-freqC).^2)).*(sin(W*2*pi.*(4*fnyqC-freqC))
./(W*2*pi.*(4*fnyqC-freqC))).^2+(DC./(fcC.^2+(4*fnyqC+freqC).^2))
.*(sin(W*2*pi.*(4*fnyqC+freqC))./(W*2*pi.*(4*fnyqC+freqC))).^2;

%calculating the PSD for camera. It includes aliasing, and blur
%units m^2/Hz

lorQ2 = (D/pi^2)./((fcQ^2)+(freqQ2.^2));%this is the "theoretical PSD to inf"

%calculating the imaginary response using the fluctuation-dissipation
%theorem

AdpQ1 = (pi.*freqQ)./(2*kB*temp).*lorentzianQ; %finite QPD A double prime
AdpQ2 = (pi.*freqQ2)./(2*kB*temp).*lorQ2; %theoretical
AdpC1 = (pi.*freqC)./(2*kB*temp).*lorentzianC; %finite camera

%the next section come from the MRanalysis_xQPDrotated code, written by
%Marjan and therefore the comments are sparse. The first part is using
%the AdpQ1 and integrating (trapezoid method) to get the 'real' part of
%the frequency response (A prime) for the QPD. It then does the exact
%same thing for the camera.

g = size(freqQ,2);
%Size of the vectors.%
ApQ1 = zeros(size(AdpQ1));
%The output is initialized.

f = zeros(size(AdpQ1));

X1 = freqQ(2:g);
AdpQ1d1 = AdpQ1(2:g);
Y1 = (X1.*AdpQ1d1)./(X1.^2-freqQ(1)^2);
f1 = trapz(X1,Y1);

```

```

f(1) = f1;
ApQ1(1) = 2/pi*f(1);

X1 = freqQ(3:g);
AdpQ1d1 = AdpQ1(3:g);
Y1 = (X1.*AdpQ1d1)./(X1.^2-freqQ(2)^2);
f1 = trapz(X1,Y1);
f(2) = f1;
ApQ1(2) = 2/pi*f(2);

%Two first elements of the output: the integrations are computed by excluding
%the first element of the input

X1 = freqQ(1:g-2);
AdpQ1d1 = AdpQ1(1:g-2);
Y1 = (X1.*AdpQ1d1)./(X1.^2-freqQ(g-1)^2);
f1 = trapz(X1,Y1);
f(g-1) = f1;
ApQ1(g-1) = 2/pi*f(g-1);

X1 = freqQ(1:g-1);
AdpQ1d1 = AdpQ1(1:g-1);
Y1 = (X1.*AdpQ1d1)./(X1.^2-freqQ(g)^2);
f1 = trapz(X1,Y1);
f(g) = f1;
ApQ1(g) = 2/pi*f(g);

%Two last elements of the output: the integrations are computed by excluding
%the last element of the input

for j = 3:g-2;
    X1 = freqQ(1:j-1);
    X2 = freqQ(j+1:g);
    AdpQ1d1 = AdpQ1(1:j-1);
    AdpQ12 = AdpQ1(j+1:g);
    Y1 = (X1.*AdpQ1d1)./(X1.^2-freqQ(j)^2);
    Y2 = (X2.*AdpQ12)./(X2.^2-freqQ(j)^2);
    f1 = trapz(X1,Y1);
    f2 = trapz(X2,Y2);

    f(j) = f1+f2;

    ApQ1(j) = (2/pi*f(j));
end

```

```

%all other elements are calculated, each by avoiding the pole at 'j'.

%the next part is the same but for the Ap for the camera

g = size(freqC,2);
%Size of the vectors.%
ApC1 = zeros(size(AdpC1));
%The output is initialized.

f = zeros(size(AdpC1));
AdpC1n = AdpC1(g);

X1 = freqC(2:g);
AdpC1d1 = AdpC1(2:g);
Y1 = (X1.*AdpC1d1)./(X1.^2-freqC(1)^2);
f1 = trapz(X1,Y1);
f(1) = f1;
ApC1(1) = 2/pi*f(1);

X1 = freqC(3:g);
AdpC1d1 = AdpC1(3:g);
Y1 = (X1.*AdpC1d1)./(X1.^2-freqC(2)^2);
f1 = trapz(X1,Y1);
f(2) = f1;
ApC1(2) = 2/pi*f(2);

%Two first elements of the output: the integrations are computed by excluding
%the first element of the input

X1 = freqC(1:g-2);
AdpC1d1 = AdpC1(1:g-2);
Y1 = (X1.*AdpC1d1)./(X1.^2-freqC(g-1)^2);
f1 = trapz(X1,Y1);
f(g-1) = f1;
ApC1(g-1) = 2/pi*f(g-1);

X1 = freqC(1:g-1);
AdpC1d1 = AdpC1(1:g-1);
Y1 = (X1.*AdpC1d1)./(X1.^2-freqC(g)^2);
f1 = trapz(X1,Y1);
f(g) = f1;
ApC1(g) = 2/pi*f(g);

%Two last elements of the output: the integrations are computed by excluding
%the last element of the input

```

```

for j = 3:g-2;
    X1 = freqC(1:j-1);
    X2 = freqC(j+1:g);
    AdpC1d1 = AdpC1(1:j-1);
    AdpC12 = AdpC1(j+1:g);
    Y1 = (X1.*AdpC1d1)./(X1.^2-freqC(j)^2);
    Y2 = (X2.*AdpC12)./(X2.^2-freqC(j)^2);
    f1 = trapz(X1,Y1);
    f2 = trapz(X2,Y2);

    f(j) = f1+f2;

    ApC1(j) = (2/pi*f(j));
end

ApQ2 = ((D/pi^2)*pi.*fcQ)./(2*kB*temp).*(1./(freqQ2.^2+fcQ^2));
%integral from 0 to inf outcome i.e. infinite A prime

%calculating the G prime and G double prime using the real and imaginary
%parts of the response function for the finite QPD (Q1), infinite (Q2) and
%camera (C1)

GpQ1 = (1/(6*pi*RQ)).*(ApQ1./(ApQ1.^2+AdpQ1.^2));
GpQ2 = (1/(6*pi*R)).*(ApQ2./(ApQ2.^2+AdpQ2.^2));
GpC1 = (1/(6*pi*RC)).*(ApC1./(ApC1.^2+AdpC1.^2));

GdpQ1 = (1/(6*pi*RQ)).*(AdpQ1./(ApQ1.^2+AdpQ1.^2));
GdpQ2 = (1/(6*pi*R)).*(AdpQ2./(ApQ2.^2+AdpQ2.^2));
GdpC1 = (1/(6*pi*RC)).*(AdpC1./(ApC1.^2+AdpC1.^2));

%now I calculate how much of the finite data we can trust (it drops off of
%the theoretical 'to inf' line). For water, Gp should be a flat line,
%therefore I compare (in logarithm) a certain point (i) to the maximum and
%see where that deviates from that by a given amount.
%The frequency at which this occurs is called the cutoff frequency (fcutoff).

for i = 1:size(GpQ1,2)
    dB = GpQ1(i)/max(GpQ1);
    if dB <= 0.90
        fcutoff = freqQ(i-1); %cutoff frequency for Gp for QPD
        break
    end
end
end

for j = 1:size(GpC1,2)

```

```

    dBc = GpC1(j)/max(GpC1);
    if dBc <= 0.90
        fcutoffC = freqC(j-1);%cutoff frequency for Gp for the cam
        break
    end
end
end

%For Gdp, we should get a straight line of slope 1 (on log scale), in order to see
%where this falls off I calculate the slope (in log10) at each point (k for QPD,
%l for camera), and where that deviates from 1 by 10% is the cutoff
%frequency (fcutoff2, fcutoffC2).

for k = 3:size(GdpQ1,2)-2
    dB2 = (log10(GdpQ1(k+1))-log10(GdpQ1(k-1)))/(log10(freqQ(k+1))-log10(freqQ(k-1)));
    if dB2 <= 0.98 || dB2 >= 1.02
        fcutoff2 = freqQ(k-1);
        break
    end
end
end

for l = 3:size(GdpC1,2)-2
    dBc2 = (log10(GdpC1(l+1))-log10(GdpC1(l-1)))/(log10(freqC(l+1))-log10(freqC(l-1)));
    if dBc2 <= 0.90 || dBc2 >= 1.1
        fcutoffC2 = freqC(l-1);
        break
    end
end
end

%Now calculating the output parameters

%For Gp we expect a flat line, slope 0
xQ = freqQ(1:i-1);
yQ = GpQ1(1:i-1);
myfittype = fittype('0*xQ+b','dependent',{'yQ'},'independent',{'xQ'}, 'coefficients',
    {'b'});
fitQ = fit(xQ',yQ',myfittype);
coeffsQ = coeffvalues(fitQ);
plateauQ = coeffsQ(1); %plateau of Gp for QPD

xC = freqC(1:j-1);
yC = GpC1(1:j-1);
myfittype = fittype('0*xC+b','dependent',{'yC'},'independent',{'xC'}, 'coefficients',
    {'b'});
fitC = fit(xC',yC',myfittype);
coeffsC = coeffvalues(fitC);
plateauC = coeffsC(1); %plateau of Gp for camera

```

```

xQ2 = freqQ2(1:size(freqQ2,2));%theoretical uses all of the available data
yQ2 = GpQ2(1:size(freqQ2,2));
myfitttype = fitttype('0*xQ2+b','dependent',{'yQ2'},'independent',{'xQ2'}, 'coefficients',
    {'b'});
fitQ2 = fit(xQ2',yQ2',myfitttype);
coeffsQ2 = coeffvalues(fitQ2);
plateauQ2 = coeffsQ2(1); %plateau of Gp for theoretical

%for viscosity, the intercept of a linear line in the logscale is necessary

%I create a custom equation for a logline of slope 1
xQ = freqQ(1:k-1);
yQ = GdpQ1(1:k-1);
myfitttype = fitttype('(xQ)*(10^b)', 'dependent',{'yQ'}, 'independent',{'xQ'}, 'coefficients',

fitQ = fit(xQ',yQ',myfitttype);

coeffsQ = coeffvalues(fitQ);
interceptQ = coeffsQ(1);
%calculating the viscosity using the intercept
etaQ = 1/(2*pi)*10^(interceptQ);

%repeating for the camera

xC = freqC(1:l-1);
yC = GdpC1(1:l-1);
myfitttype = fitttype('(xC)*(10^b)', 'dependent',{'yC'}, 'independent',{'xC'},
    'coefficients', {'b'});
fitC = fit(xC',yC',myfitttype);
coeffsC = coeffvalues(fitC);
interceptC = coeffsC(1);
%camera viscosity
etaC = 1/(2*pi)*10^(interceptC);

%and finally for the theoretical case
xQ2 = freqQ2(1:size(freqQ2,2));
yQ2 = GdpQ2(1:size(GdpQ2,2));
myfitttype = fitttype('(xQ2)*(10^b)', 'dependent',{'yQ2'}, 'independent',{'xQ2'},
    'coefficients', {'b'});
fitQ2 = fit(xQ2',yQ2',myfitttype);
coeffsQ2 = coeffvalues(fitQ2);
interceptQ2 = coeffsQ2(1);
%theoretical case viscosity
etaQ3 = 1/(2*pi)*10^(interceptQ2);

end

```

## Appendix B

### Calculation of Equation 5.3

Here, the principal value integral from the Kramers-Kronig relation, Equation 5.2, is calculated using partial fractions.

Starting from the fluctuation-dissipation theorem, which relates the magnitude of the fluctuating force to the energy dissipation, we get the imaginary response function,

$$A''(\xi) = \frac{\pi\xi}{2k_B T} \times PSD(\xi) = \frac{D}{2\pi k_B T} \times \frac{\xi}{(\xi^2 + f_c^2)}, \quad (\text{B.1})$$

for a bead trapped in water, whose power spectrum is defined by a Lorentzian function (Equation 2.15). Next, the Kramers-Kronig relation is the principal value integral:

$$A'(f) = \frac{2}{\pi} P \int_0^\infty \frac{\xi A''(\xi)}{(\xi^2 - f^2)} d\xi = \frac{D}{\pi^2 k_B T} P \int_0^\infty \frac{\xi^2}{(\xi^2 - f^2)(\xi^2 + f_c^2)} d\xi. \quad (\text{B.2})$$

Using partial fractions, we can decompose the integral into 3 separate integrals. Only one of these integrals now has the pole at  $\xi = f$ .

$$\frac{\xi^2}{(\xi^2 - f^2)(\xi^2 + f_c^2)} = \frac{f_c^2}{(\xi^2 + f_c^2)(f^2 + f_c^2)} + \frac{f}{2(\xi - f)(f^2 + f_c^2)} - \frac{f}{2(\xi + f)(f^2 + f_c^2)}. \quad (\text{B.3})$$

Therefore,

$$A'(f) = \frac{D}{\pi^2 k_B T} \left[ \left( \frac{f_c^2}{(f^2 + f_c^2)} \int_0^\infty \frac{1}{(\xi^2 + f_c^2)} d\xi \right) + \frac{f}{2(f^2 + f_c^2)} \left( P \int_0^\infty \frac{1}{(\xi - f)} d\xi - \int_0^\infty \frac{1}{(\xi + f)} d\xi \right) \right]. \quad (\text{B.4})$$

The first integral is a known integral:

$$\int_0^\infty \frac{1}{(\xi^2 + f_c^2)} d\xi = \frac{\pi}{2f_c}. \quad (\text{B.5})$$

The second is a principal value integral, which, itself, is split into two separate integrals:

$$P \int_0^\infty \frac{1}{\xi - f} d\xi = \lim_{df \rightarrow 0} \left( \int_0^{f-df} \frac{1}{\xi - f} d\xi + \int_{f+df}^\infty \frac{1}{\xi - f} d\xi \right) \quad (\text{B.6})$$

$$= \lim_{df \rightarrow 0} \lim_{x \rightarrow \infty} \left[ \left[ \ln |\xi - f| \right]_0^{f-df} + \left[ \ln |\xi - f| \right]_{f+df}^x \right] \quad (\text{B.7})$$

$$= \lim_{df \rightarrow 0} \lim_{x \rightarrow \infty} \left[ \ln |(f - df) - f| - \ln |-f| + \ln |x - f| - \ln |(f + df) - f| \right] \quad (\text{B.8})$$

$$= \lim_{x \rightarrow \infty} \left[ \ln |df| - \ln |-f| + \ln |x - f| - \ln |df| \right] \quad (\text{B.9})$$

The  $\ln |df|$ s cancel and we're left with

$$P \int_0^\infty \frac{1}{\xi - f} d\xi = \lim_{x \rightarrow \infty} \left[ -\ln |-f| + \ln |x - f| \right] \quad (\text{B.10})$$

The third integral is

$$P \int_0^\infty \frac{1}{\xi + f} d\xi = \lim_{x \rightarrow \infty} \left[ \ln |\xi + f| \Big|_0^x \right] \quad (\text{B.11})$$

$$= \lim_{x \rightarrow \infty} \left[ \ln |x + f| - \ln |f| \right] \quad (\text{B.12})$$

As  $x$  approaches infinity, both  $\ln |x + f|$  and  $\ln |x - f|$  will approach infinity. In Equation B.4, these are subtracted. Similarly,  $\ln |-f| = \ln |f|$  and so those terms vanish as well, leaving us with

$$A'(f) = \frac{D}{\pi^2 k_B T} \left[ \left( \frac{f_c^2}{(f^2 + f_c^2)} \left( \frac{\pi}{2f_c} \right) \right) \right]. \quad (\text{B.13})$$

Therefore, the solution is

$$A'(f) = \frac{D f_c}{2\pi k_B T (f^2 + f_c^2)}. \quad (\text{B.14})$$